Electrical and Computer Engineering ETDs

Engineering ETDs

9-26-2008

Minimally invasive capacitive micromachined ultrasonic transducers array For biomedical applications

Xiaoyang Cheng

Follow this and additional works at: https://digitalrepository.unm.edu/ece_etds

**MINIMALLY INVASIVE CAPACITIVE MICROMACHINED
ULTRASONIC TRANSDUCERS ARRAY FOR BIOMEDICAL
APPLICATIONS**

BY

XIAOYANG CHENG

B.S., ME, Huazhong University of Science & Technology 1994
M.S., ME, South China University of Tech, 2001

DISSERTATION

Submitted in Partial Fulfillment of the
Requirements for the Degree of

Doctor of Philosophy

ENGINEERING

The University of New Mexico
Albuquerque, New Mexico

AUGUST, 2008

To my parents

ACKNOWLEDGMENTS

imaging and signal processing greatly benefited me and inspired me and made this research project to be a very complete story. I would like to send my thanks to them.

I want to thank my lab colleague at UNM, Mengli Wang, who provided me the valuable help in the measurements of some devices. It was great to work together with a lovely girl like her.

A very special thanks goes to David Lemmerhirt -- Thank you for sincere friendship, guidance and help for editing/commenting on my dissertation. I am deeply honored to have chance to work with such talented people like you during my early career.

The companion of all of my friends has been an important part of my life. With mutual help and encouragement, we lived through many physical and spiritual challenges. They are Jian Ouyang, Dawen Li, Jingyu Liu, Jingyang Liu, Huiping Sheng, Huimin Li, Min Zhu, Ke Ye, Yongjie Zhu, Weimin Wang, Yuan Xie, Xiaochuan Bi, Yuefeng Zhu, Sheng Yang, Ying Yao, Trushal Chokshi, Jianbai Wang, Zhimei Zhu, Jinzheng Peng, Weibin Zhu, Yanhua Wu, Asli Burcu Ucok, Onnop Srivannavit, Zhi Yang, Yuhai Mei, Guohong He, George Meng, Chi-Ting Lin, and George Binder.

Finally, this thesis is dedicated to my parent. I cannot imagine how I can finish my PhD study without their endless love. I am grateful to them for instilling their philosophy on hardworking and persistence on me from a very young age. I want to thank my sister Hongxia Cheng and my brother Kevin Cheng for their great love, care, support and encouragement, for helping me going through failures and difficulties and becoming a better person.

MINIMALLY INVASIVE CAPACITIVE MICROMACHINED ULTRASONIC TRANSDUCERS ARRAY FOR BIOMEDICAL APPLICATIONS

BY

XIAOYANG CHENG

ABSTRACT OF DISSERTATION

Submitted in Partial Fulfillment of the
Requirements for the Degree of

Doctor of Philosophy

ENGINEERING

The University of New Mexico
Albuquerque, New Mexico

AUGUST, 2008

MINIMALLY INVASIVE CAPACITIVE MICROMACHINED ULTRASONIC TRANSDUCERS ARRAY FOR BIOMEDICAL APPLICATIONS

BY

XIAOYANG CHENG

B.S., ME, Huazhong University of Science & Technology 1994
M.S., ME, South China University of Technology, 2001
PhD., Engineering, University of New Mexico, 2008

ABSTRACT

Ultrasound covers a broad range of applications from underwater exploration and nondestructive evaluation of materials to medical diagnosis and treatment. The ultrasonic transducer plays an important role in determining the resolution, sensitivity, as well as other critical diagnostic capabilities of an ultrasonic detection or imaging system. Currently piezoelectric ultrasonic transducers dominate the market. The device performance of the piezoelectric ultrasonic transducer in medical applications is limited by the material properties and related electrical and acoustic impedance match issues. The fabrication of piezoelectric transducer array requires meticulous handcrafting. It is difficult and expensive to fabricate densely populated piezoelectric array. The Capacitive Micromachined Ultrasonic Technology (CMUT) has emerged as a promising alternative. Compared to piezoelectric technology, the MEMS based CMUT has advantages such as ease of fabrication and the potential to integrate with front-end electronic circuits. CMUT could also provide broader acoustic bandwidth and higher sensitivity over its piezoelectric counterpart, which would improve the image resolution.

The main goal of this dissertation work is to develop miniature CMUT devices for minimally invasive biomedical diagnosis and treatment. A two-layer poly-silicon surface

micromachining process mixed with bulk micromachining process was developed. Based on this process, three prototypes of application were developed in this research:1) a multi-looking imager, 2) a miniaturized invasive ultrasonic probe, and 3) an image-Guided Therapy (IGT) system. Primary testing results including the acoustic/electrical characterization, ultrasonic imaging and flowmetering have been obtained and are discussed. These results indicate that CMUT technology has great potential to become the next-generation transducer technology for the Intravascular Ultrasonic system, invasive blood-flow metering, and therapeutic treatment.

TABLE OF CONTENTS

LIST OF FIGURES

LIST OF TABLES

CHAPTER I

INTRODUCTION

Ultrasound refers to sound waves having a frequency above the human ear's audibility limit of about 20 KHz. Uses for ultrasound are wide-ranging, with applications in industrial testing, therapeutic healthcare, and medical imaging. The advantages of ultrasound as imaging modality are numerous. Ultrasound imaging is extremely safe and is believed to have no adverse health effects. It does not use ionizing radiation. It delivers excellent quality results at relatively low cost, and it is highly portable.

The earliest investigation of this inaudible acoustic phenomenon can be dated back to the 19th century, when the first high frequency ultrasound whistle was introduced to study the audibility limit. In 1928, Soviet scientist Sergei Y. Sokolov first proposed a through-transmission technique for flaw detection in metals, which is the first use of ultrasound in industry [1]. The first use of ultrasound as a medical diagnostic tool was for transmission imaging of brain tumors by Karl Theodore Dussik of Austria in the early 1940s [2]. In 1965, Siemens Medical Systems of Germany developed the first real-time scanner. Since then, the application of ultrasound has gradually gained popularity for medical diagnosis. In past decades, intensive research in this area has generated significant outcomes such as phase-array scanning mechanisms [3] and beamforming technologies [4]. Software-controlled system such as Computed Sonography System appeared in 1983 and earned a good reputation for high resolution and clarity at a low price. Currently, real-time 3D imaging, photoacoustic imaging, intravascular applications, high-frequency arrays, and

ultrasonic therapeutic treatment are among the research topics of greatest interest within this field.

A commercial state-of-the-art ultrasonic imaging system is shown in Fig 1.1 a), with its block diagram shown in Fig 1.1 b). The system has three modules: the transducer arrays, the processing unit, and the image reconstruction unit. The transducer array is connected to the processing unit, which contains a transmitter pulser, a low-noise preamplifier (LNA), a time-gain controlled amplifier (TGC), a low-pass filter, and an analog-to-digital converter (ADC) for each channel. Transmit and receive beamforming unit are located in the processing unit. The image reconstruction unit is composed of image processing electronics and the display.

During conventional pulse-echo operation, the transducer arrays both transmit and receive the ultrasonic signals. In transmit mode, an electrical signal is transformed to an acoustic signal and transferred to the surrounding medium. This acoustic signal is reflected when encountering discontinuous (mismatched impedance) interfacial layers at different locations along the propagation path. The reflected signal is detected by the receivers and converted into electrical signal. This signal is then processed and the image is reconstructed.
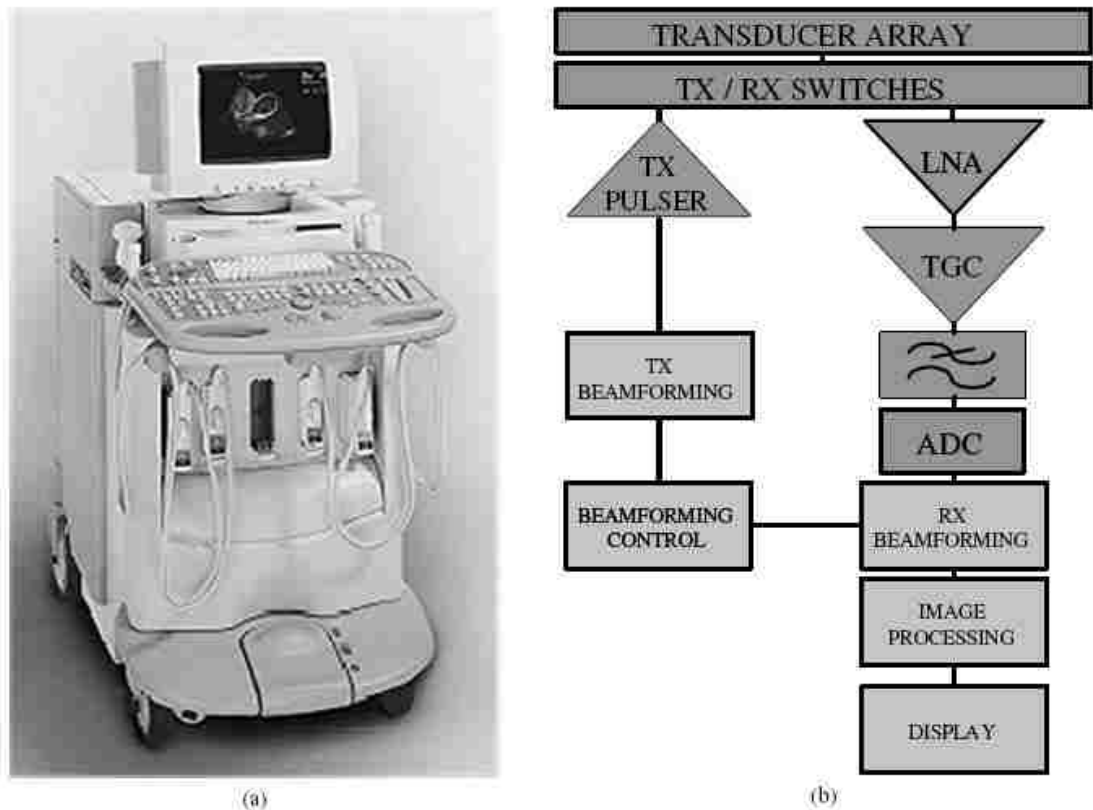
Figure 1.1 a) A commercial state-of-the-art ultrasonic imaging system, b) The block diagram of the imaging system [5].

Advances in digital signal processing technology and system integration have enhanced the abilities of the backend processing and reconstruction modules. These achievements improve the quality of the imaging. Nevertheless, their performance largely depends on the quality of the original echoed signals from the transducer array, making the transducer one of the most critical components in the ultrasonic imaging system.

1.1 Transduction Mechanisms

Physical mechanisms of ultrasonic transducers include magnetostriction, piezoelectricity, and electrostatics. J.Joule first described magnetostriction in 1842, when he noticed that iron changed length in response to changes in magnetism [6]. Other

magnetostrictive materials are cobalt, nickel, ferrite, and terbium alloys. However, the losses due to eddy currents in metallic transducers limit their use at higher frequencies.

Piezoelectricity is a coupling between mechanical and electrical behaviors of a material. Bound electric charge collects on the material's surface by the imposition of mechanical stress. Conversely, the material deforms when it is subjected to a voltage drop. The Curie brothers first discovered the piezoelectric effect in 1880. A detailed review of piezoelectricity and piezoelectric polymers and piezoelectric ceramics can be found in [7, 8]. Historically these two types of materials and their composite dominated the early ultrasound application field and were used to generate and detect ultrasound. In contrast to its popularity, the piezoelectric polymer transducers suffer from low coupling efficiencies, limiting their use in diagnostic imaging. Piezoelectric ceramics, and especially the PZT (lead–zirconate–titanate) family, are popular because they offer relatively high coupling efficiency, a wide range of dielectric constants, and low dielectric loss. Piezoelectric ceramics are the best choice for ultrasonic imaging directly on solids because the acoustic impedance of the piezoelectric ceramics is of the same order of magnitude as that of the solids. However, when the objective is to excite and detect ultrasound in fluidic environment such as the body fluids, then piezoelectric transducers (30 Mrayl(kg/m^{2}s)) have impedance mismatch problems between the piezoelectric and the fluid of interest (1 Mrayl). The situation becomes acute for air-coupled applications because the air acoustic impedance is about 400 Rayl. The large impedance mismatch implies that piezoelectric transducers are inefficient in those applications. Matching layers are usually adopted to improve the energy coupling efficiency. However, the use of matching layers introduces other problems. First, it is

very difficult to find matching layer materials to accommodate the large impedance mismatch. Secondly, the energy coupling comes at the expense of bandwidth, which is critical for the application. In addition, the matching layer required for high frequency transducers is impractically thin. Finally, the complexity of fabricating the devices reduces reliability and increases cost.

Capacitive Micro-machined Ultrasonic Transducers (CMUT) are widely considered as a promising alternative to the piezoelectric transducers. Extensive research on the fabrication and modeling of CMUT began in the early 1990s [9-13]. The working mechanism of CMUT is called electrostatic transduction [10]. It can best be described by means of a parallel-plate capacitor where one plate is kept stationary, and the other (membrane) is forced in flexural vibration by a time varying voltage or by the reflection of the wave at its surface (reception). The capacitance modulation due to membrane displacement is used to detect the signal. This basic principle of actuation and detection is not a new invention. However, it has not gained popularity simply because electric field strengths caused by the applied voltage are required to be on the order of million volts per centimeter ($10^6 V/cm$), in order to achieve electrostatic forces as large as a kilogram per square centimeter (kg/cm^2)[14]. This is virtually impossible in most macro-scale applications. Thanks to micromachining technologies, the downscaled capacitive ultrasound transducer fabrication has turned this into reality.

One advantage of CMUT over its piezoelectric counterpart is the impedance mismatch when performing in a fluid medium. It is normally three orders of magnitude lower than that of piezoelectric transducers. Therefore, CMUT can increase energy coupling efficiency, and improve bandwidth with comparable sensitivity to piezoelectric

transducers. Another important difference between the CMUT and the piezoelectric transducers is that the CMUT coupling efficiency is a function of the electric field intensity and the capacitance, and for piezoelectric transducers, it mainly depends on the material properties. Therefore, CMUT performance can be easily tailored by changing the device dimensions and bias conditions but not the materials properties.

The biggest advantage of CMUT over piezoelectric transducers is the ease of fabrication. It becomes very difficult to fabricate densely populated piezoelectric transducer array due to limitations in existing transducer array and interconnect technologies. The assembly of a typical piezoelectric array requires meticulous handcrafting. CMUT are fabricated using process steps from standard silicon integrated circuit fabrication technology. This makes it possible to fabricate large multi-element arrays that can supply a large amount data for the signal processing. Furthermore, CMUT can easily be integrated with electronic circuits using common fabrication technologies. The integration will greatly miniaturize device dimensions, and reduce the parasitic capacitance due to the cross coupling of interconnects within the arrays.

CMUT technology has made significant progress both on device and system levels since its first introduction [9]. However, present ultrasonic transducer technology is still predominantly based on piezoelectric materials. There is a long way to go before CMUT can successfully replace piezoelectric counterpart in the application of underwater exploration, nondestructive evaluation of materials, and medical diagnosis and treatment. The performance metrics that directly relate to the resulting imaging quality, such as bandwidth, sensitivity, output pressure, transformation efficiency, and angular response must be further improved. Although CMUT technology provides a promising approach to

manufacturing densely populated array, downscaling the transducer dimensions, providing individual electrical connections to array elements, and integration with electronic circuits makes fabrication of 2D arrays with high element densities and realization of high-frequency probes challenging. The challenge to improve the capability of fabricating high element count arrays with high yield is haunting designers and process engineers. Other challenges include increasing reliability, cross talk between independent elements, and packaging.

1.2 Motivation

1.2.1 Intravascular Ultrasonic System

The development of CMUT has been driven by its potential in bio-medical diagnostics and therapy, especially biomedical imaging. The commercial piezoelectric ultrasonic imaging system has benefited many fields of medicine, and the principle of ultrasonic imaging has been well recognized. High frequency, real time imaging systems has been an important research area in the past decade [15-16]. A higher ultrasound frequency increases the resolution of the image. The trade off to achieve high resolution is that at high frequencies, ultrasound becomes more attenuated in the medium. This prevents high frequency ultrasound from imaging deep into the body. In order to obtain the anatomical details of the organs/tissue inside the human bodies, one approach is to invasively implant the ultrasonic transducer inside the body and close to the organ/tissue. One of these invasive ultrasonic systems is intravascular ultrasound imaging system (IVUS) [17]. The schematic description of IVUS is shown in Figure 1.2a). The

photograph (Fig 1.2b) gives a closer view of a forward-looking ultrasonic probe using piezoelectric transducer elements.
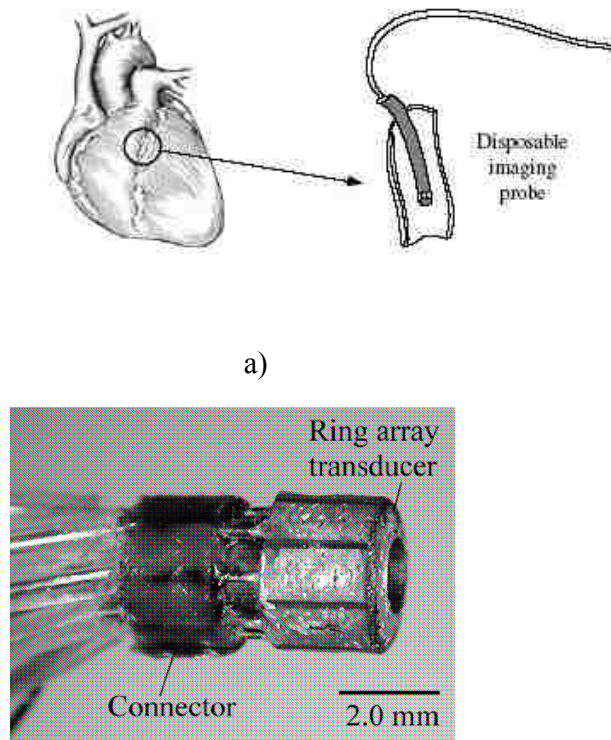
a)

b)

Figure 1.2 a) Schematic of IVUS imaging probes [5]. b) Photograph of a forward-looking ultrasonic probe using piezoelectric transducer elements [18].

The IVUS system commonly uses a long, flexible tube called a catheter, typically 0.5-3 millimeters in diameter, to support a disposable imaging probe at its tip from which the ultrasound signals are transmitted and received. It was developed not only to resolve anatomical detail, but also to subsequently guide the interventional treatment by the catheter. The most available IVUS fixes one image plane perpendicular to the catheter axis. By mechanical retraction of the catheter it is possible to build a 3-D image of the region of interest. A disadvantage of this system is the limitation on the data acquisition

rate since the volume is scanned by physical motion. This system is too slow to allow real-time imaging of dynamic structures. Another disadvantage is the poor resolution. It results in blurry 3D images, degrades the spatial resolution, and limits the accuracy of volume measurement [13].

IVUS with a 1D array of piezoelectric transducers mounted around a catheter was reported [17] and has been commercialized. This kind of IVUS heads can be scanned electronically and acquire 2D images around the catheter. Mounted on a catheter using meticulous handcrafting, it is difficult to manufacture these IVUS arrays with consistent pitch and kerf with the dimensions necessary for intravascular operations [5]. Furthermore, these arrays provide only the side viewing capability and cannot look at the direction the catheter is pointing at. Driven by the clinical need, recent IVUS R&D efforts have been focused on the development of a front-looking IVUS (see Figure 1.2b) in order to provide the guidance of the intervention and Doppler-based flow measurement. This front looking IVUS was implemented using annular arrays mounted on the front-end of a catheter [19-20]. However, these IVUS are restricted to only the front view and are not equipped with side-looking imagers. Meanwhile, a multi-looking design was proposed in the literature [21-22], which divides a 1D array of piezoelectric transducers into two sections. The shorter section is bent and mounted on the front end of the catheter to form an annular array for front looking, while the longer section is mounted on the sidewall of the catheter for side looking. This device can potentially provide views from both the front and the side. However, due to numerous elements missing in the front looking imager, the prototype was not able to provide clinical imaging.

If multiple pieces of transducers can be mounted on the front and the side of a catheter platform, the real-time 3D image could be obtained from the simultaneous multi direction imaging as shown in Figure 1.3. This will enormously expand the capability of ultrasonic medical diagnosis. CMUT has manifested itself as a promising candidate to realize MEMS based IVUS that will possess the capability of multi-direction imaging.
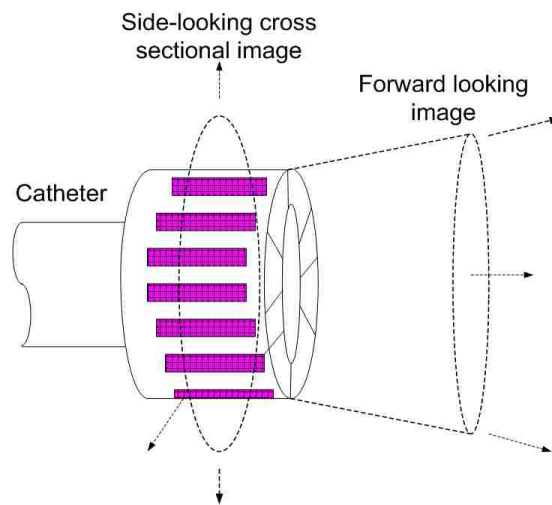
Figure 1.3 Schematic of a side-looking and forward-looking imager

1.2.2 Blood Flow metering

Another prominent area of ultrasonic application in medicine is blood flow metering. Blood flow measurement can identify clogging and other abnormities of the blood vessel and is useful for diagnosing cerebra-vascular and cardiovascular diseases. In the past century, a variety of methods for measurement of volumetric blood flow were developed. Flow measurement using an electromagnetic wave is commonly used for the measurement of blood flow in physiological studies [23]. However, this electromagnetic flow meter is relatively large and cannot produce accurate results in low flow measurement. Laser blood flow meters were first used in 1975 to measure the blood flow

in living tissues [24]. While it can produce high-resolution measurement results, laser Doppler flow meters cannot measure blood vessels deep inside the tissue due to limited penetration depth of high-frequency laser light. Additionally, the sensitivity of lasers to red blood cell motion is too high and unable to distinguish between directed (or net) flow and random red motion [25]. This distinction is critical for low flow velocity measurements needed for many clinical applications.

Ultrasound Doppler uses the frequency/wavelength shift of ultrasound for detection of blood flow. The ultrasonic Doppler flow meter was first applied to blood detection in 1959. Compared to its laser counterpart, ultrasound has a lower frequency and can penetrate into the biological object to measure blood flow deep inside the tissue. A negative effect of the ultrasound is that the resolution of the measurement is poorer. Currently there are several types of Echo and Doppler cardiograms systems commercially available for measuring blood flow [26, 27]. These systems were large and were developed mainly for transcutaneous, noninvasive measurement of blood flow. These systems are similar to conventional ultrasonic imaging, but due to the wavelength related penetration depth limit, these traditional Doppler ultrasonic systems must compromise flow resolution and penetration depth. In order to overcome the dilemma between the detection depth and the measurement resolution, one solution would introduce high-frequency waves to the target vessel using a minimally invasive tool. Therefore, an implantable CMUT array would be a very good candidate for blood flow measurement. Due to its miniature size, this tool can be implanted close to target vessels deep inside the tissue without introducing significant disruption to the tissue. Figure 1.4 illustrated the concept of using this implantable CMUT array to measure the cerebral blood flow rate.
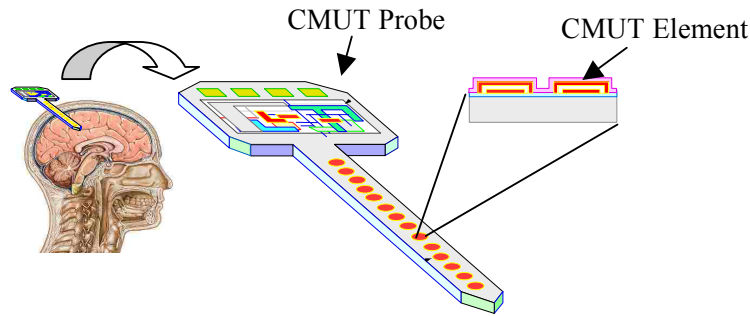
Figure 1.4 Ultrasound applications in blood flow metering.

1.2.3 Image-Guided Therapy

Ultrasound can do more than produce diagnostic images. In recent years, ultrasound enhanced approaches have also become increasingly popular for therapeutic treatment and surgical applications such as the thrombolysis in arterial obstruction [28], and removal of necroses pathological tissues [29]. The benefits of the use of thrombolytic therapy in arterial obstruction include a reduction in both mortality and morbidity of acute myocardial infarction and improved outcomes in patients with peripheral vascular disease. Recent studies [28] have also shown that the arterial obstruction (clots) can be mechanically disrupted into small fragments using ultrasound at high intensity.

Although most studies of ultrasound-enhanced thrombolysis have concentrated on the potential for external application, the endovascular route is also attractive, offering the potential to deliver local ultrasound directly at the site of thrombosis while limiting exposure of normal tissue. Some results [28] also demonstrate that exposure to ultrasound increased the total amount of tissue plasminogen activator (tPA) and depth of penetration in the absence of liquid permeation, and both effects would accelerate clot dissolution. To fulfill this target, High Intensity Focused Ultrasound (HIFU) is required. While piezoelectric arrays have traditionally been used for HIFU, again the fabrication

flexibility and improved performance of CMUT technology has made it competitive for HIFU applications.

An all-ultrasound system integrating diagnosis (imaging) and treatment (HIFU treatment) together using CMUT technology could be developed. This system can be described as Image-Guided Therapy (IGT) [30-31]. By using ultrasound for both imaging and HIFU treatment, it is easier to register (align) imaging and therapy using one modality (see Figure 1.5).

1.2.4 Photoacoustic Imaging

In addition, photoacoustic imaging has emerged actively in ultrasound research. Photoacoustic imaging (PAI) [32-35] constructs images using ultrasounds generated by a target object, which is illuminated with pulsed infrared illumination. The target object is flashed with a laser pulse, leading to optical absorption and thermo-elastic expansion. This expansion generates ultrasound, which can be detected by an ultrasound transducer. Whereas traditional pulse-echo ultrasound imaging has low contrast in soft tissue due to similar acoustic impedances, PAI benefits from high optical contrast combined with excellent spatial resolution determined primarily by the ultrasound wavelength, approaching cellular resolution [35]. Contrast in PAI depends primarily on the optical wavelength and absorption spectrum of the tissue. Thus, PAI provides an appreciably higher contrast than pulse-echo ultrasonic imaging. Moreover, when the light source is tuned to the near infrared, PAI can be used to form an image well over a centimeter into tissue. For photoacoustic imaging of live human or animal tissue with red blood cells, hemoglobin provides significant help in boosting the contrast ratio. Hemoglobin has a very high optical contrast in the visible and infrared spectra. As a result, high-contrast

imaging of blood containing structures in tissue such as tumors or blood vessels is one of the unique advantages of PAI. Compared to other techniques, PAI is a safe process that uses nonionizing radiation and fluences within standards set by ANSI. It has potential to provide 3D images with high resolution and contrast. In addition to viewing anatomical structure, photoacoustic imaging is capable of detecting composition of tissue and functional activities [34] of an organ based on blood-related infrared absorption rate difference and sensitivity of the optical spectrum of hemoglobin to oxygen saturation [35].
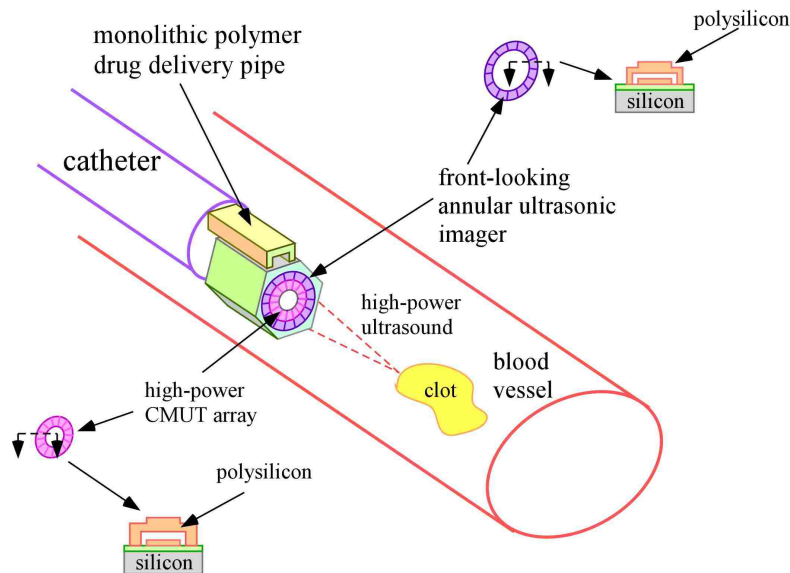
Figure 1.5 Schematic of Image-Guided Therapy.

The vast majority of photoacoustic imaging experiments reported to date have relied on individual or arrayed-piezoelectric transducers for the ultrasound detection. CMUT device could provide an attractive replacement for piezoelectric devices for PAI because they provide broader acoustic bandwidth. A miniature CMUT array can be used in an invasive PAI system and would provide information not available from a non-invasive

system. Figure 1.5 illustrates the schematic of a PAI process using a miniature CMUT array.
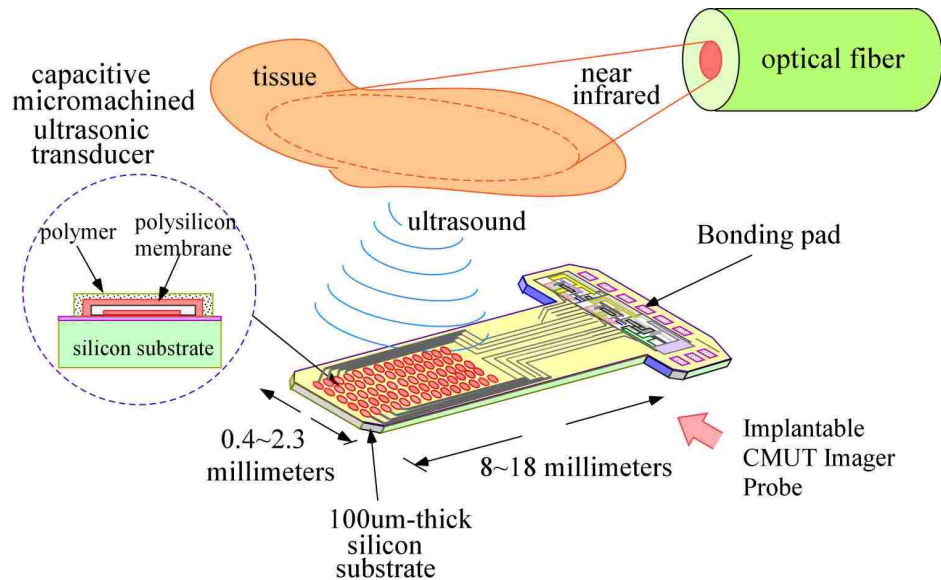
Figure 1.6 Schematic of the CMUT imager probe and its application in a photoacoustic imaging process

1.3 Summary

This project addresses the need for a miniaturized invasive ultrasonic imaging system and implantable ultrasonic array for blood flow metering as well as the demand for an Image-Guided Therapy system. The development of such systems requires expertise in multi-disciplinary areas such as acoustic modeling, fabrication, signal processing, and front-end/mixed signal circuit design.

This project proposes to contribute to the development of prototypes for those three major biomedical applications in terms of device modeling, fabrication, and characterization. The fabrication of an implantable probe-shaped transducer array will be introduced as a prototype for blood flow meter. Due to its miniature size, it can be implanted close to target vessels deep inside the tissue without significant tissue

15

disruption. With no extra fabrication process, we could also add metallic electrodes that can be used for the tissue electric stimulation and recording. This approach is currently being used for the study of neuron activity. A MEMS prototype for an IVUS system (multi-direction imager) will be fabricated by monolithically integrating multiple ultrasonic transducer arrays on a flexible silicon substrate. By slightly modifying the fabrication process of the imager, we could also integrate HIFU capabilities and thus develop devices for image-guided therapy.

This dissertation is organized as follows:

Chapter II starts with the analysis of the fundamentals of CMUT cells (elements). This includes the CMUT structure, principles of operation, essential parameters impacting the CMUT performance and electrical equivalent circuit simulations. Frequency performance based on the equivalent circuit simulation will be discussed. The physics behind charge injection will be analyzed, and to reduce charge-trapping problems, a new CMUT cell design will be introduced.

In chapter III, the fabrication of the new CMUT design will be discussed and its difference from conventional structure will be addressed. The fabricated CMUT cell laid the foundation for the further development of the transducer arrays and prototypes discussed earlier.

In chapter IV, the fabrication and assembly process for the prototype will be detailed; Design guideline for transducer array will also be presented.

In chapter V, experiments to characterize CMUT performance in transmitting and receiving mode will be discussed in detail. The results will be used to verify the theoretical predictions and validate the equivalent circuit model.

Image characterization, for photoacoustic imaging and pulse-echo imaging will also be fully addressed in Chapter VI.

In chapter VII, some primary results for blood flow metering and Image-Guide therapy will be discussed. Efforts will also be made to explore the integration of CMUT with CMOS electronics in this chapter.

The conclusions and recommendations for future work will be drawn in the final chapter.

CHAPTER II

THE DESIGN OF CMUT

The cross sectional view of the conventional CMUT cell is shown in Figure 2.1 a). The whole structure is built on the silicon substrate. A thin membrane is supported by a peripheral supporting structure. A rough vacuum gap (if sealed) is underneath the membrane. The major parameters for this structure include the gap distance t_g, the membrane thickness t_m, and the membrane radius a. The cell lays the foundation for the CMUT element, which is typically composed of more than one cell. Figure 2.1 b) shows the cross-sectional schematic of CMUT elements. Different arrangement of elements are shown in Figure 2.1 c) and d).

a)

b)

c)

d)
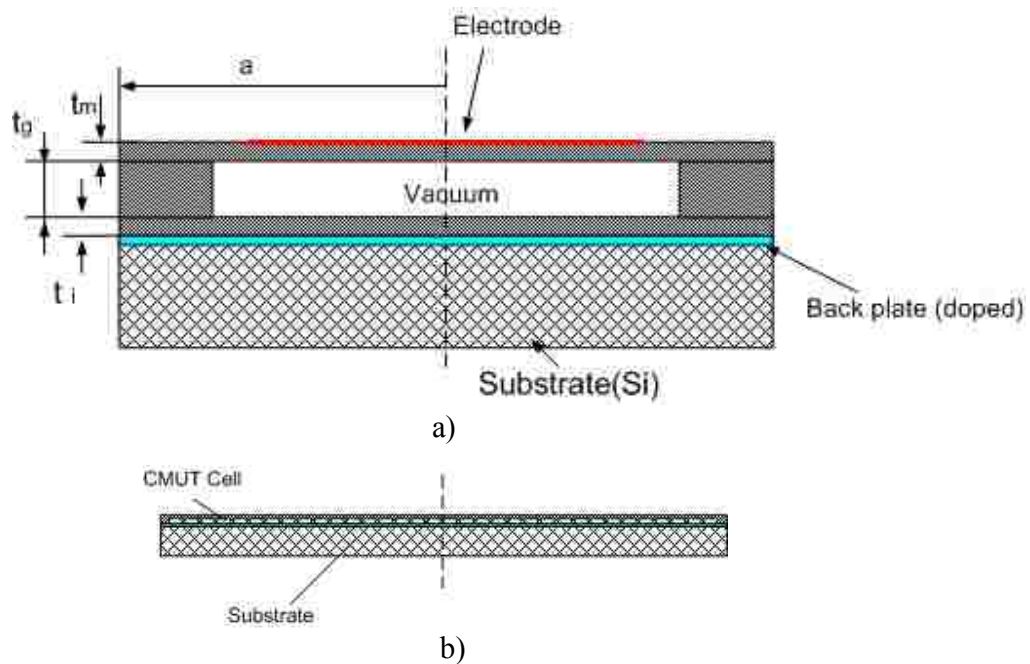
Figure 2.1 a) the cross-sectional schematic of the single CMUT Cell, b) The cross section of CMUT array; c) The 2-D array elements   d) The 1-D array elements

Three main parts are essential in the CMUT transducer, i.e. the membrane, the gap between electrodes, and the substrate.

1) Materials available for the membrane include silicon nitride, polysilicon and metal. Material properties such as stiffness and mass density of the membrane have to be selected carefully to achieve good impedance matching between the membrane and the coupling medium, which is of very low acoustic impedance. In particular for a broadband transducer, the membrane stiffness (rigidity) should be low and essentially constant. Aside from the material properties, geometrical parameters such as membrane thickness and membrane diameter are essential in determining dynamic characteristics such as resonant frequency.

2) The gap distance between the upper and lower electrodes plays a major role in device performance in terms of sensitivity, dynamic range and coupling efficiency. Smaller gap distance results in higher sensitivity and coupling efficiency at the cost of dynamic range. Usually, insulating materials with sufficiently high electrical resistance are required to avoid destruction of the layers by electric short-circuiting

19

(breakdown). But it is known the insulation layers subject to high electric fields often suffer from a charge-trapping problem and that causes reliability issues.

3) Silicon is used for the substrate since it can be machined with high accuracy and reproducibility and offers the possibility of producing a silicon oxide insulation layer by thermal oxidation. It has been commonly used for CMUT substrates. Generally, the thickness of the substrate is expected to be less than the standard silicon wafer (500μm) in order to reduce the acoustic loss.

Fabrication and the characterization of CMUT are time and cost intensive. A reliable modeling and simulation analysis are therefore important for a successful CMUT design. Usually, simulation is done based on finite-element methods (FEM) and analytical methods based on equivalent circuit models such as Mason's model. Many efforts have been made by researchers to derive simpler models based on piston radiator and plate capacitance theory [36-38]. These models accounts for membrane impedance and are well-suited to analyze CMUT when operating in air or vacuum (small load). For CMUT operating in a fluid medium, the membrane impedance is typically ignored based on the assumption that the medium load over-dominates the performance of the system.

In this chapter, the principle of CMUT operation will be introduced. Analysis such as mechanical analytical calculation will be conducted. Equivalent circuit analysis will be used to find the frequency performance and will pave the way for the new CMUT structure design. Effort will also be made to address the dielectric charge-trapping problem.

2.1 Principle of operation

In principle, the CMUT can be thought of as many small condenser microphones [39] (cells/elements) grouped together in one substrate and operating in parallel. The CMUT transducer converts electrical energy into mechanical energy (acoustic) and vice versa. It is based on the effect that the spacing between the plates of a cell may be changed by mechanical (receiving operation) or electrostatic (transmitting operation) force. In transmitter mode the top moveable plate is vibrated due to an applied AC voltage, causing it to emit ultrasonic waves. In the receiver mode the incoming ultrasonic waves cause the moveable plate to vibrate, which modulates the capacitance value between the two plates. If the two plates are electrostatically charged by a DC voltage source, an electric signal is generated.

The externally applied force such as the incoming pressure wave, usually acts perpendicularly to membrane surface in receiving operation. While in transmitting operation, this membrane is under the electrostatic force applied by the electrical field E between the membrane and the bottom electrode. This electrical field has very little effect on the displacement along the radical direction. Therefore, the CMUT model can be simplified to a one dimensional (1-D) model, where the membrane displacement of the CMUT cell is reduced to a single degree of freedom along the normal direction. A parallel plate approximation is considered to illustrate the major aspects of the CMUT devices as shown in Figure 2.2.
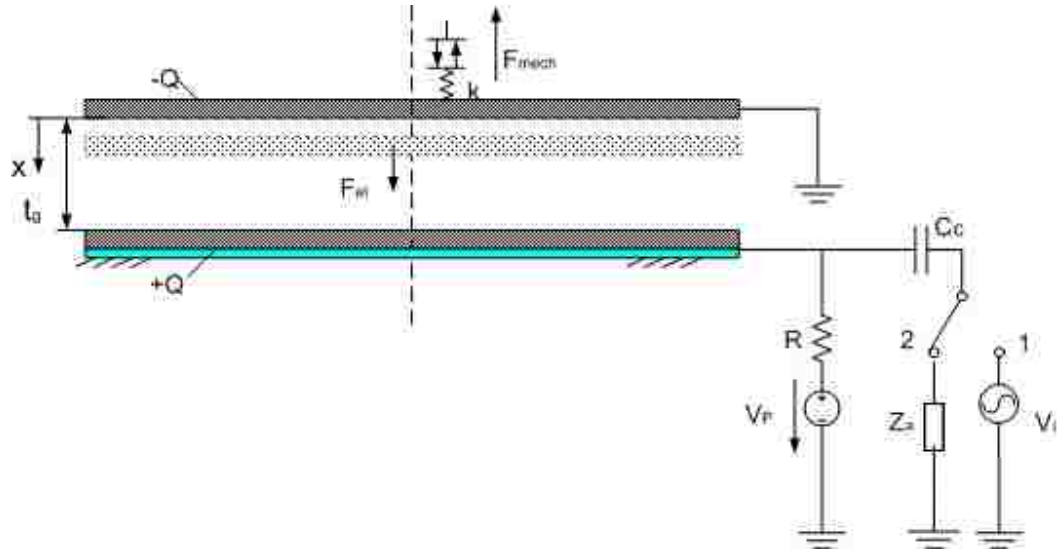
Figure 2.2 the simplified lumped CMUT model

2.1.1 Electrostatic Force

The fixed plate is charged $(+Q_0)$ using a DC voltage source V_p connected through resistor R. In order to avoid AC current flow into the voltage source, the condition

$$R \gg \frac{1}{\omega C_c} \qquad (2\text{-}1)$$

should be fulfilled. The electrostatic force F_{el} generated by the applied DC voltage is always an attraction force, regardless of the polarity of the voltage. The capacitance between these two plates is

$$C_0 = \frac{\varepsilon_0 A}{t_g} \qquad (2\text{-}2)$$

where A is the overlapped area of the capacitor plates, ε_0 is the permittivity of free space, The energy equation for a capacitor is

$$W = \frac{1}{2}C_0 V^2 \qquad\qquad (2\text{-}3)$$

where V is the voltage across the two plates. If an AC voltage V_i is applied to the plate (transmitting mode), the moveable plate oscillates up and down centering at the static position and the electrostatic force causing the oscillation is given by

$$F_{el} = \frac{\partial W}{\partial x} = \frac{\partial(\frac{1}{2}C'(V_p - V_i)^2)}{\partial x} = \frac{1}{2}(V_p - v_i)^2 \frac{\partial C'}{\partial x} \qquad (2\text{-}4)$$

where x is the displacement of the moveable plate, and C' is the capacitor in the dynamic situation given by

$$C' = \frac{\varepsilon_0 A}{t_g - x} \qquad\qquad (2\text{-}5)$$

Differentiating (2-5), the capacitance change per unit displacement along x-axis is expressed as

$$\frac{\partial C'}{\partial x} = \frac{\varepsilon_0 A}{(t_g - x)^2} \qquad\qquad (2\text{-}6)$$

followed by a Taylor series expansion, giving

$$\frac{\partial C'}{\partial x} = \frac{C_0}{t_g}(1 - \frac{2}{t_g}x + \frac{3}{t_g^2}x^2 - \frac{4}{t_g^3}x^3 + \ldots) \cong \frac{C'}{t_g} \qquad (2\text{-}7)$$

If a continuous wave (narrow band) signal applied, by plugging $v_i = V_i \cos(\omega_0 t)$, the total electrostatic force is

$$F_{el} == \frac{1}{2}(V_p^2 + \frac{V_i^2}{2} - 2V_p V_i \cos(\omega_0 t) + \frac{V_i^2}{2}\cos(2\omega_0 t))\frac{\partial C'}{\partial x} \qquad (2\text{-}8)$$

which demonstrates that the resulting electrical force consists of a constant part superimposed by an alternating part. The constant part (DC voltage) was generated from

both the dc bias and the ac signal. The alternating part has two harmonics. If the applied DC voltage V_p is much larger than the time varying voltage V_i, (i.e. $V_p >> V_i$) an operation of the transducer at the first harmonic is obtained. The transducer will operate at the second harmonics if the DC voltage is very small. The dominant time varying force becomes

$$F_{el} = V_p V_i \cos(\omega t) \frac{\partial C'}{\partial x} \approx V_p V_i \cos(\omega t) \frac{C'}{t_g} \qquad (2\text{-}9)$$

Induced by the time-varying charge stored between the two plates, the vibration of the moveable plate creates an ac output current i_0 (receiving mode), given by

$$i_0 = V_p \frac{\partial C'}{\partial t} = V_p \frac{\partial C'}{\partial x} \frac{\partial x}{\partial t} \qquad (2\text{-}10)$$

whose magnitude in phase form can be written as

$$I_0 = V_p \frac{\partial C'}{\partial x} \omega_0 X \approx \frac{V_p \omega_o X C'}{t_g} \qquad (2\text{-}11)$$

where X is the magnitude of the displacement x of the moveable plate which is related to the mechanical properties of the device.

When a pulse or a burst broadband signal, for example a square wave pulse $v_i = V_i \prod(t - \tau)$ is applied, which can be expressed in Fourier series:

$$
\begin{aligned}
v_i &= \frac{4V_i}{\pi}(\sin(\frac{\pi t}{\tau}) + \frac{1}{3}\sin(\frac{3\pi t}{\tau}) + \cdots + \frac{1}{n}\sin(\frac{n\pi t}{\tau}) + \cdots) = \\
&\quad \frac{4V_i}{\pi}(\sin(\omega t) + \frac{1}{3}\sin(3\omega t) + \cdots + \frac{1}{n}\sin(n\omega t) + \cdots)
\end{aligned}
\qquad (2\text{-}12)
$$

An electrostatic force similar to equation (2-8) can be obtained with harmonic terms. The higher harmonic term can be trimmed off at the small displacement operation.

2.1.2 DC Bias Voltage

Equation (2-10) shows an important aspect for designing a CMUT transducer, i.e. the output current signal can be improved by increasing the applied DC voltage V_p and the device capacitance C'. However, the applied DC voltage is limited due to the fact that increasing beyond the so-called collapse voltage $V_{collapse}$ the electrostatic force F_{el} cannot be balanced by the mechanical restoring force F_{mech} anymore and the moveable plate (membrane) collapses to the substrate. This instable behavior is well known as "Pull-In" effect [40-42]. It is well known that for ideal parallel plate operation, the "Pull-In" effect occurs when the plate is pulled by a dc bias that is larger than one-third of the gap ($x = {t_g}/{3}$). [43] The collapse voltage of an ideal parallel-plate capacitor can be calculated using the following equation

$$V_{collapse} = \sqrt{\frac{8kt_g^3}{27\varepsilon_0 \pi a^2}} \qquad (2\text{-}13)$$

where k is the spring constant of the variable capacitor system, ε_0 is the permittivity of the air in the gap. For the device with dielectric layers between two electrodes with thickness t_i and dielectric constant ε_i, the collapse voltage is expressed as

$$V_{collapse} = \sqrt{\frac{8k(t_g + t_i/\varepsilon_i)^3}{27\varepsilon_0 \pi a^2}} \qquad (2\text{-}14)$$

At this marginal voltage, the membrane deflection is about $x = \dfrac{t_g + t_i/\varepsilon_i}{3}$, which means that the membrane displacement x can be greater than one-third of the gap at the "Pull-In" point. The membrane will be collapsed if the dc voltage is increased beyond the

"pull-in" point. In the case that an insulator layer is present between the membrane and the bottom electrode, the membrane will snap back if the dc voltage is reduced to [43]:

$$V_{snap-back} = \sqrt{\frac{2kt_i^2(t_g - t_i)}{\varepsilon_i \pi a^2}} \qquad (2\text{-}15)$$

It is preferable that the dc bias voltage be small enough to avoid electric current leakage inside the CMUT elements (arrays). For minimally invasive application such as the implantable biomedical devices, low dc bias is desirable and necessary to meet the safety regulations. Furthermore, applying a high dc bias voltage presents challenges for integrating CMUT with CMOS circuits.

2.1.3 Frequency Analysis

When a time varying electrostatic force is applied to the plates, a CMUT will resonate/vibrate at the same frequency as one of the inherent mechanical frequencies of the structure. A CMUT transducer is normally a resonant device. The quality factor (Q) of this resonant structure is determined by the load Z that represents the acoustic impedance of the medium (air or liquid). Q is high in air because of its low-acoustic impedance. For liquid immersion the high acoustic impedance of water overdamps the CMUT resonant behavior and Q will be much lower. Basically, the electrostatic force generated on the mechanical port is divided between the mechanical impedance of the membrane and the acoustic load, just like a voltage division. For frequencies where the mechanical impedance of the transducer is small compared to the acoustic load, all of the electrostatic force generated on the mechanical port appears across the load. This usually results in a wide bandwidth characteristic.

It is known that the vibration modes of a structure are governed by material properties and geometric device dimensions including the membrane thickness, diameter and the anchoring configuration. For a circular polysilicon membrane anchored along its whole circumference, the resonant frequency can be determined by the following analytical Equation [44]

$$f_r = \frac{1}{2\pi}\sqrt{\frac{k}{m}} = \frac{t_m K}{2\pi a^2}\sqrt{\frac{E}{12\rho(1-\upsilon^2)}}$$ (2-16)

where t_m is the thickness of the membrane, E is the Young's modulus, ρ is the density, and υ is the Poisson ratio of the membrane material. The coefficient K depends on the anchoring conditions at the edges. A simply supported membrane will have lower value than that of a rigidly supported membrane [45].

Obviously, the thicker and/or the smaller a membrane is, the higher resonant frequency will be. The influence of the residual film stress can also be evaluated by comparing to the in-plane critical (buckling) stress for a simply supported circular membrane. The critical stress is denoted σ_{cr} and is calculated from [46] as

$$\sigma_{cr} = \frac{4.2Et_m^2}{12(1-\upsilon^2)a^2}$$ (2-17)

Polysilicon is chosen as the CMUT membrane material. (Note: *Parylene C was coated on the CMUT for encapsulation. Due to a relatively small (about 2.3% that of the polysilicon) Young's modulus of parylene C and for simplifying the problem, the impact of parylene C on the mechanical characteristics of this membrane was neglected*). For a circular membrane with the parameters summarized as in Table 2.1, σ_{cr} is found to be 122MPa.

PROPERTIES	POLYSILICON	Parylene C
Young's modulus E (Gpa)	169	4
Poisson ratio υ	0.3	0.4
Density ρ (kg/m^3)	2329	1289

Table 2.1 Properties of the building materials used in this bi-layered CMUT.

The residual film stress (around -10MPa to 20Mpa) is small in comparison to σ_{cr}. Therefore, the presence of the residual film stress has minimal influence on the membrane stiffness and resonant frequency.

Another factor that affects the resonant frequency is the spring softening effect caused by the dc bias voltage. The explanation for spring softening [47] lies in the fact that, as the capacitor plate deflects in the +x direction, a spring force is generated in the −x direction. However, displacement in +x direction under constant dc voltage also causes an increase in the electrostatic force in the +x direction. When the dc voltage is increased, the electrostatic spring drops, and the resonance frequency will drop as well. The spring softening effect can be expressed as in equation (2-18).

$$k_{soft} = \frac{\varepsilon_0 \pi a^2 V_{DC}^2}{t_g^3} \qquad (2\text{-}18)$$

Real CMUT devices (cells) are always clamped fully at the edge. Therefore, the nonlinear and non-uniform electrostatic forces are generated due to the presence of residual stress and the developed strain energy in the middle of the membrane. For large diameter, large gap membrane with large deflection, nonlinear behavior known as the spring hardening effect [52] is introduced. But for CMUT application where the

deflection is usually much smaller in comparison to the membrane thickness, the large

deflection model of analysis can be ignored.

2.1.4 Important Parameters

a) Transformation ratio

One of the most important parameters of interest in CMUT design is the

transformation ratio n. The transformation ratio represents the ratio between the

conversions from the electrical domain quantity (*current*) to its analogue in mechanical

domain (*average velocity*). The transformation ratio is expressed as [43]

$$n = \frac{V_{DC}\varepsilon_0 \pi a^2}{(t_g - x)^2} \qquad (2\text{-}19)$$

The transformation ratio affects the acoustic bandwidth and the sensitivity of the

transducer. In order to increase the transformation ratio, a dc bias voltage as high as

allowed with the device structure should be applied. From equation (2-19), the

transformation ratio is proportional to the square of the membrane radius a, and inversely

proportional to the square of the gap distance t_g. Decreasing t_g increases the

transformation ratio.

b) Capacitance

The capacitor C_0 in equation (2-2) is considered as the 'fixed' capacitance with zero

dc bias. For non-uniform deformation of the membrane under dc bias voltage V, the value

of capacitance C can be derived as:

$$C \approx 2\pi\varepsilon_0 \int_0^a \frac{r}{t_g - x(r)} dr \approx \frac{2\pi\varepsilon_0}{t_g} \int_0^a r(1 + \frac{x(r)}{t_g}) dr \qquad (2\text{-}20)$$

$x(r)$ is the deflection profile of the membrane, approximately expressed as

$x(r) = \dfrac{x_0}{a}(a-r)$, where x_0 is the center deflection of the membrane with a dc bias

voltage applied.

Thus:

$$C(x_0) = C_0(1 + \frac{1}{3t_g}x_0) \qquad\qquad (2\text{-}21)$$

Taking into account the deflection is approximately proportional to the square of the

dc bias voltage [42], which is

$$x_0 \approx \frac{\varepsilon_0 \pi a^2 V^2}{2kt_g^2} \qquad\qquad (2\text{-}22)$$

Equation (2-21) can be rewritten as:

$$C(V) = C_0 + \frac{\varepsilon_0 \pi a^2 C_0}{6kt_g^3}V^2 \qquad\qquad (2\text{-}23)$$

Besides the device capacitance C, there is another capacitance which can have a

significant negative effect on the device performance. It is called parasitic capacitance,

and, in some cases, it can dominate the active capacitance of the device. Parasitic

capacitance exists in the areas between the bottom electrode and the peripheral edges.

Parasitic capacitance also comes from the electrical interconnects to the substrates. This

parasitic capacitance could easily overwhelm the device capacitance for high element

count transducer arrays. It does not contribute to the output signal and is detrimental in

achieving acceptable SNR from array elements.

A structural buffer layer should be used to isolate the electrode from the substrate and minimize the parasitic capacitance. The width of metal electrical interconnects also needs to be reduced to the minimum achievable with the fabrication process. But there is a tradeoff since narrower interconnects means higher resistance between cell elements. This has implications for transducer performance: higher loss due to the higher serial resistance; higher noise level due to the increased built-in resistance component in the transducer impedance; and low efficiency due to the phase shift among the individual cell elements.

Other feasible solutions to the parasitic capacitance problem include using through-wafer-interconnect technology in conjunction with CMUT and the hybrid or monolithic integration of electronics, typically implemented using CMOS technology. These approaches help reduce the parasitic capacitance by largely reducing the length of interconnects between CMUTs and the first stages of readout circuits.

c) Impedance

One important consideration is the impedance of the transducers mismatching with their surrounding medium. The impedance of CMUT can be represented as $Z_m S$, which is the lumped mechanical impedance of the membrane, given by the ratio of the uniform applied pressure to the resulting average velocity ($Z_m = P / \bar{v}$). Higher impedance indicates a stiffer membrane. The better approach to determine the impedance value is to apply a static pressure and integrate the resulting displacement over the surface of the membrane of a model built using FEM software such as ANSYS. When loaded by air, the lumped membrane impedance $Z_m S$ dominates the bandwidth of the transducer. If immersed in liquid, the impedance of the surrounding medium $Z_a S$ determines the

CMUT bandwidth. This impedance is related to the acoustic wave number and the medium load area defined as:

$$k_0 = \frac{2\pi f}{c} \qquad (2\text{-}24)$$

where f is the drive frequency and c is the acoustic wave speed in the medium. For $k_0 a \gg 1$, $Z_a S$ is simply treated as the real lumped impedance and is given by the product of the specific acoustic impedance, defined as the product of density of the medium with the speed of sound in the medium $Z_a = \rho c$, and transducer area S. The real impedance increases the power dissipated by the source. For $k_0 a \ll 1$ (lower frequency, when the radius a is a fixed value), the impedance becomes a complex value, the imaginary part manifests itself as a mass loading which decrease the resonant frequency of the oscillation. An approximate model was considered [48]

$$Z_a = Z_r e^{j\theta} = R_r + jX_r = \rho_e c S \frac{(k_0 a)^2}{1+(k_0 a)^2} + j\rho_e c S \frac{k_0 a}{1+(k_0 a)^2} \qquad (2\text{-}25)$$

where ρ_e is the density of the medium. In addition, the gap (cavity) also presents the impedance Z_{gap} since residual air always remains in the nominally vacuum-filled gap. It is defined as

$$Z_{gap} = V_{gap} / (\rho_g c^2) \qquad (2\text{-}26)$$

where V_{gap} represents the volume of the gap cavity, and ρ_{gap} is the density of the air in the gap.

2.2 Equivalent Circuit Model

Different types of CMUT equivalent circuit based on Mason's model can be found in literature [14, 40]. Figure 2.3 shows the equivalent circuit for both transmitting and

32

receiving modes. In Figure 2.3 a), the CMUT operates as a transmitter excited by a voltage source to drive the impedance of the medium $Z_a S$, while the CMUT is working as receiver excited by acoustic pressure P_{in} to drive the electrical load $Z_L S$ (Figure 2.3b). The negative term $-C_c$ is used to represent the spring softening effect as mentioned earlier.
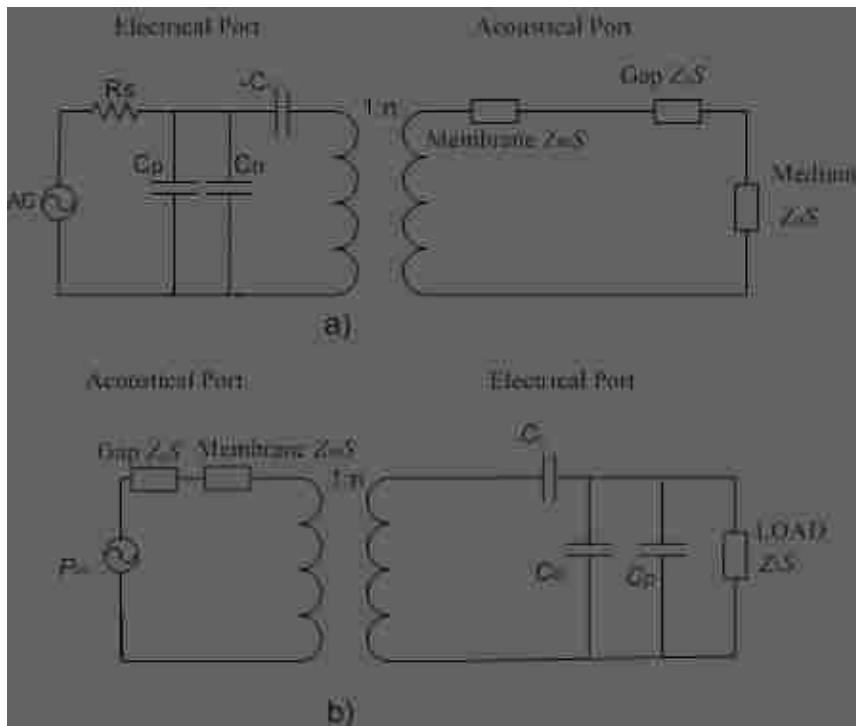
Figure 2.3 Electrical equivalent circuits

2.2.1 Electromechanical Analogy

Solutions using the above models involve both electrical and mechanical (acoustic) domains. It is worth noting that there exists similarities between electrical and mechanical applications. These similarities are called electromechanical analogies [49], which govern the model transformation from the mechanical domain to the electrical one, and vice versa.

Figure 2.4 illustrates the transformation of a signal between the mechanical and electrical domains. The elastic model in the mechanical domain can be transformed into an equivalent LCR model. The element values C_m, L_m and R_m in the equivalent LCR model are determined by the dynamic mass m, spring stiffness k and viscous damping c of the elastic model, and by the magnitude of the electromechanical transformation ratio n, as defined in Equation (2-19).

The relations between the elements in the mechanical domain with the equivalent LCR model can be expressed as follows: [44, 49]

$$C_m = \frac{n^2}{k} \quad L_m = \frac{m}{n^2} \quad R_m = \frac{c}{n^2} \tag{2-27}$$
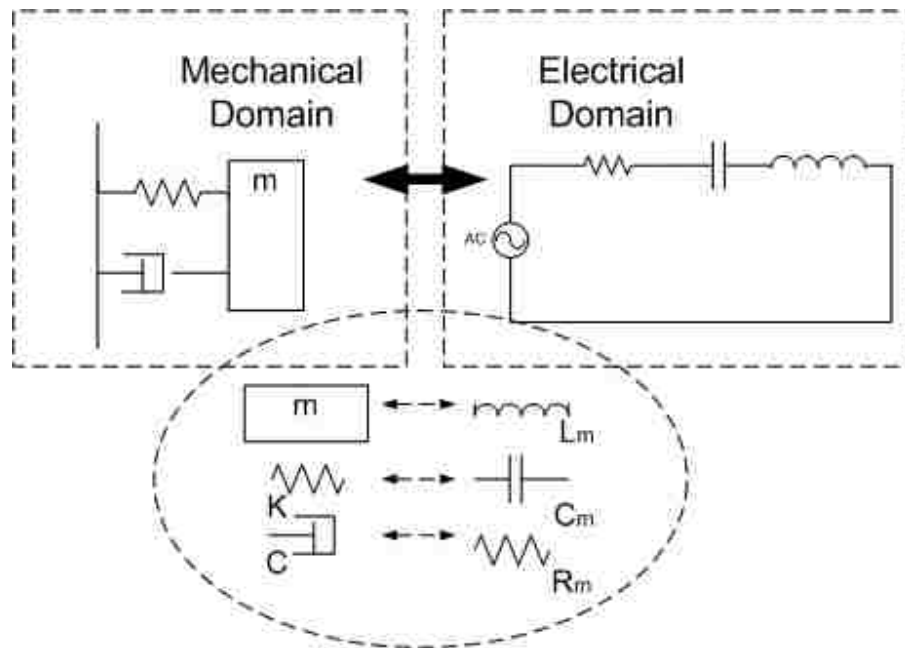
Figure 2.4 Electromechanical Analogies. A comparison of the mechanical domain to the electrical domain

2.2.2 Reduced Equivalent Circuit

By applying the electromechanical analogy, reduced equivalent circuit models in electrical domain are obtained from the circuit of Figure 2.3. The membrane impedance Z_m is replaced by its equivalent parameters C_m, L_m and R_m. The impedance of medium Z_a is converted to Z_a / n^2 as well. The gap impedance Z_{gap} is neglected.

In the transmit mode, there is no electrical limitation on the applied voltage other than the collapse voltage of the membrane or the electrical breakdown of the insulation material. The electrical mismatch between the electrical source and the transducer is not a concern. Therefore, efforts should be made to maximize the pressure at the mechanical side with the maximum allowed voltage applied. The reduced equivalent circuit model is shown in Figure 2.5a), where the pressure has its analogue parameter, voltage v in electric domain. To have a fast response to the applied voltage, the time constant of the network needs to be reduced.
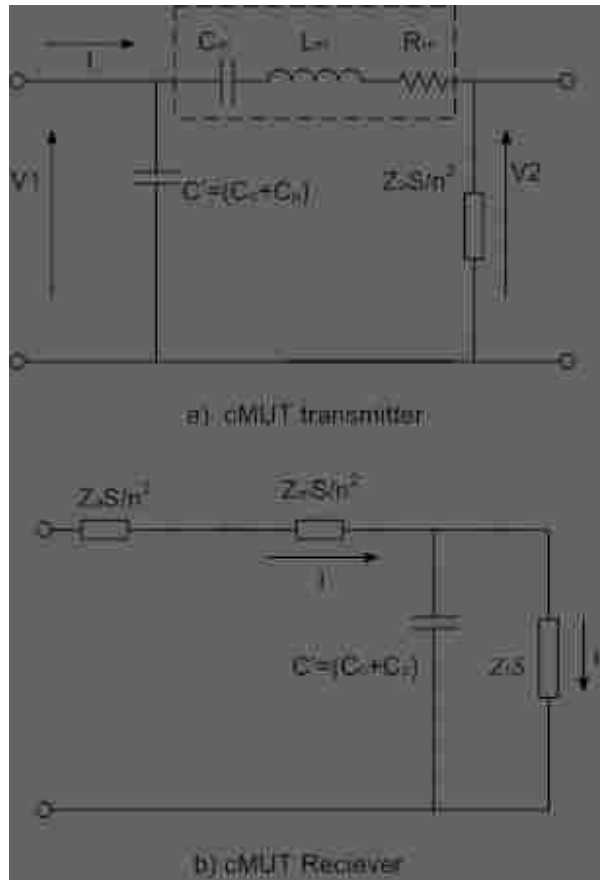
Figure 2.5 Reduced Equivalent Circuit of CMUT

When the membrane is immersed in the fluid, and its impedance Z_m is ignored, the model in Figure 2.5 reduces to just a first order model (resistance-capacitance (RC) circuit), in which the time constant is simply expressed as

$$\tau = \frac{C'Z_a}{n^2} \qquad (2\text{-}28)$$

To reduce the time constant τ so that the bandwidth can be increased, the parasitic capacitance C_p should be reduced to a minimum. From Figure 2.5a), the input impedance is expressed as:

$$Z_{in}(s) = \frac{V(s)}{i(s)} = \frac{L_m C_m s^2 + (\frac{Z_a}{n^2} + R_m)C_m s + 1}{s(C' L_m C_m s^2 + (\frac{Z_a}{n^2} + R_m)C_m C' s + (C_m + C'))} \qquad (2\text{-}29)$$

Figure 2.6 has shown the simulated result for the electrical input impedance in different medium. Because of the low acoustic impedance in air, the Q factor of the input impedance is high, whereas in water, the resonance was dominated by the high impedance of the water. The frequency range primarily determines the frequency bandwidth of the transducer.
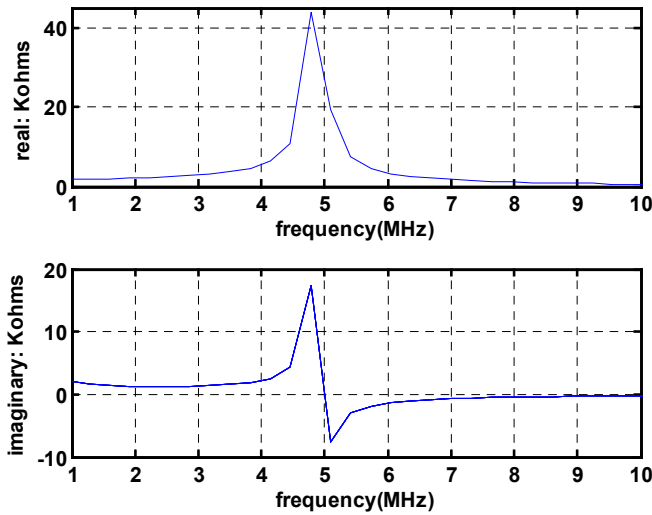
a)
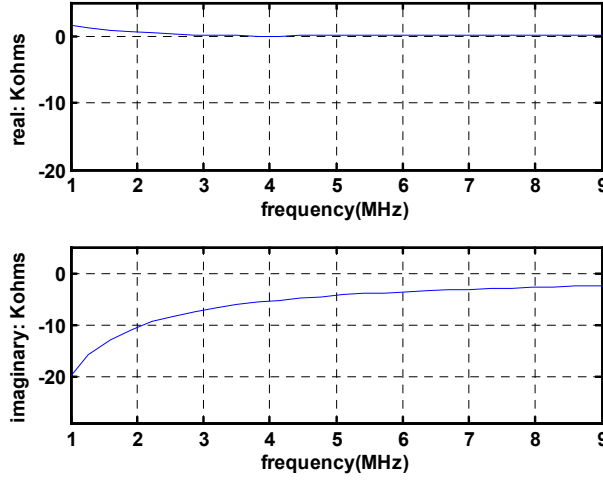
b)

Figure 2.6 Simulation results of Electrical Input Impedance operating a) in air; b) in water. The dimension of CMUT membrane is 46um in diameter, 1.5um in thickness.

For the case of receiver mode, the reduced equivalent circuit is given as in Figure 2.5b). The electrical load impedance Z_L can be expressed as real impedance R_L and imaginary impedance X_L or $C_L S$. The transfer function is expressed as:

$$\frac{i_1(s)}{i(s)} = \frac{1}{R_L (C' + C_L)s + 1}$$

(2-30)

Similarly, the parasitic capacitance C_p and load C_L need to be reduced in order to have a better frequency response. In reality, the off-chip capacitance is always much larger than the CMUT capacitance itself. Buffering circuit are expected to be inserted between the readout circuit and the CMUT.

In immersion transducers, the maximum pressure occurs at resonance frequency f_r and the higher end of the bandwidth is determined by anti-resonance frequency f_a. Qualitatively, both values will determine the frequency bandwidth [48]. Figure 2.7

38

illustrated the shape of the membrane at both frequency modes. f_r and f_a can be determined by setting the $Z_{in} = 0$, $Z_{in} = \infty$ respectively in the equivalent circuit. Therefore,

$$f_r = \frac{1}{2\pi\sqrt{L_m C_m}} \tag{2-31}$$

$$f_a = \frac{1}{2\pi}\sqrt{\frac{C'+C_m}{C'L_m C_m}} = \frac{1}{2\pi}\sqrt{\frac{C'/C_m + 1}{L_m C'}} \tag{2-32}$$

Note that the frequency f_r coincides with the frequency in Equation (2-16) in the mechanical domain by substituting the Equation (2-27) into (2-31).

a) f_r

b) f_a
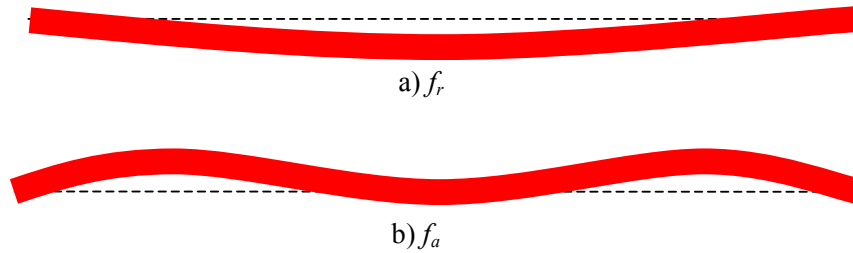
Figure 2.7 the frequency mode

From Equations (2-31) and (2-32), the membrane impedance (C_m, L_m and R_m) plays an important role in the values of f_r and f_a. Increased L_m will have a smaller f_r, but f_a will become smaller as well. Note that L_m is proportional to the effective mass while C_m is inversely proportional to the stiffness k of the membrane according to the Equation (2-27). The initial decreased mass m increases f_r and f_a together. But it is important to increase f_a without increasing f_r so that higher bandwidth can be obtained. One solution would be to force the central region to bend in the same direction with the remaining portion at the actual f_a. This can be achieved by putting a mass to the center of the membrane (the boss), forming a nonuniform membrane.

Another important performance metric is the electromechanical coupling coefficient K_T^2 [45]. K_T^2 is defined as the ratio of the stored mechanical energy to the total stored energy in the transducer. This parameter indicates how efficiently the electrical energy applied to the device is converted into mechanical energy of the membrane. The commonly used method is to use the resonance and the anti-resonance frequencies to calculate K_T^2. This method requires knowing the relation between the impedance and the frequency of the transducer. It has the following equation: [50-51]

$$K_T^2 = \frac{f_a^2 - f_r^2}{f_a^2} \qquad (2\text{-}33)$$

By substituting Equations (2-31) and (2-32), the Equation (2-33) can be rewritten as:

$$K_T^2 = 1 - \frac{C'}{C' + C_m} = \frac{1}{C'/C_m + 1} = \frac{1}{(C_0 + C_p)/C_m + 1} \qquad (2\text{-}34)$$

It can be seen that the parasitic capacitance will decrease the coupling coefficient, while increasing C_m (deceasing stiffness k) will increase the coupling coefficient. As we have already known, the dc bias voltage will cause the spring softening effect, and reduce the stiffness k as expressed in Equation (2-18). Therefore, higher dc bias voltage will cause a higher coupling coefficient as well.

2.3 Non-uniform membrane (Bossed Membrane)

A non-uniform membrane has a central region that is thicker than the peripheral region. The schematic is shown in Figure 2.8. By changing the size of the boss (dimension, thickness), the whole structure impedance can be modified.
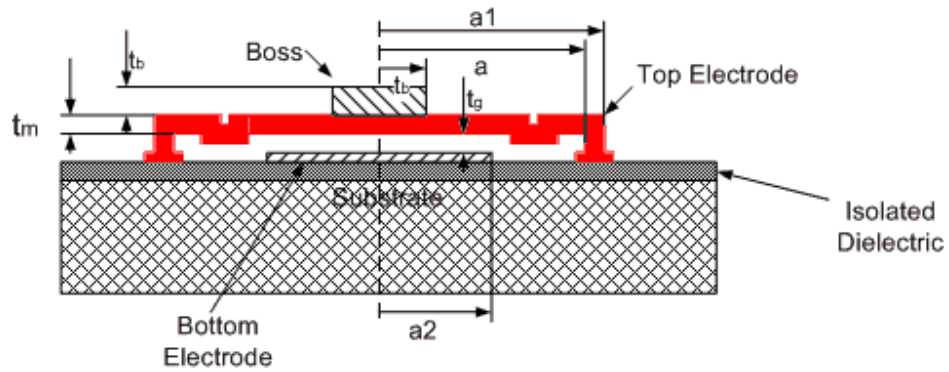
Figure 2.8 Bossed Membrane structure cross-sections view

Some researchers have analyzed the characteristics of similar bossed-membrane devices for the pressure sensors [52]. Simulation results using non-uniform membrane for CMUT were also reported in [46]. However, to our knowledge, no prototype of such a bossed membrane CMUT has ever been reported. Notice that the additional mass at the center also affects the stiffness, which has negative impact on the bandwidth. Therefore, the geometrical dimensions of this additional mass have to be chosen cautiously. To some extent, adding a boss at the center allows relatively separate control of the mass and spring constant of the membrane. This mass part may also serve to increase the output pressure and allows a more piston-like transducer behavior, which increases the average displacement of the membrane.

Finite Element Analysis (FEA) is the best method to find the frequency response of this non-uniform membrane. The force induced by the electric fields is applied as boundary conditions for mechanical analysis. Taking into account the actual CMUT structure after fabrication, we adopted the Parylene-TEOS-polysilicon composite system shown in Figure 2.9 a). The natural frequencies can be found using modal analysis.
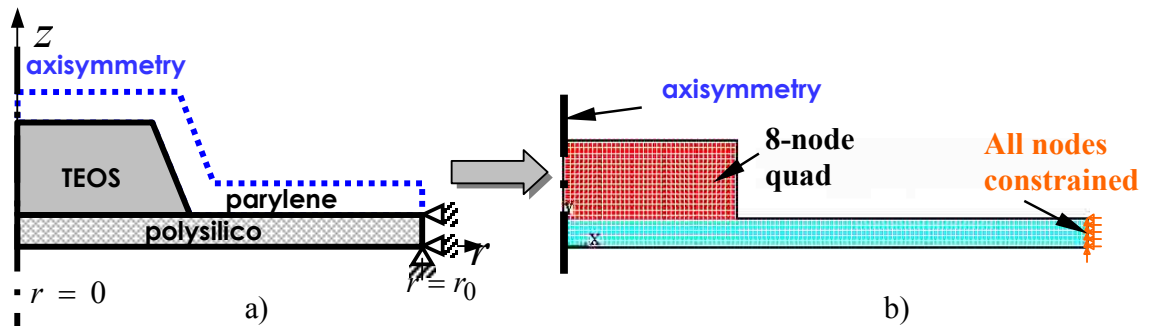
Figure 2.9 finite element model of axisymmetric membrane constrained at its periphery.

The 46μm membrane is taken as an example. An axisymmetric geometry shown in Fig. 2.9 b) was created and discretized by 8-node elements (PLANE42) with constraint at the periphery of membrane. The first three natural frequencies are listed in Table 2.2 where the frequency difference between the 1st and 2nd is found to be increased by almost 1/3 due to the addition of boss. The mode shapes for the first three frequencies are also shown in the table for reference.
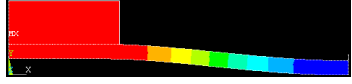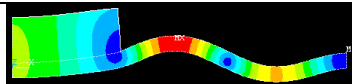
MODE	MODE SHAPE	NATURAL FREQUENCY 46B(MHZ)	NATURAL FREQUENCY 46P (MHZ)	DIFFERENCE BETWEEN MODES (MHZ)	
				46B	46P
1		6.3690	7.5289		
				28.435	21.461
2		34.804	28.990		
				50.239	34.904
3		85.043	63.894		

Table 2.2 Natural frequencies of the CMUT devices 46B and 46P by FEA (46B represents the bossed membrane CMUT element with 46um in diameter, while 46P is the uniform membrane CMUT with 46um in diameter).

2.4 Dielectric Charging

As mentioned earlier, a dielectric layer is usually present between the two electrodes to avoid the short-circuiting when the membrane is pulled down. A major concern for CMUT with dielectric layers is charging of the dielectrics [53-55]. The frequently used insulation materials are silicon oxide and nitride, both of which have high insulation resistance and field strength. The bulk or surface of such dielectrics can be charged up locally under high electric field. This accumulated parasitic charge may alter actuation voltages and change the mechanical behaviors.

Several kinds of parasitic charges can be created during CMUT fabrication, including [56-59]: 1) the interface trapped charges Q_{it}, due to the interruption of the periodic lattice structure. This type of charge can exchange charges with silicon in a short period of time; 2) immobile fixed oxide/nitride charges Q_f located at the silicon dielectric interface, which cannot be charged or discharged easily; 3) Oxide trapped space charges Q_{ot}, which are associated with defects in dielectrics. The reason for these defects could be radiation or electron injection or plasma induction; and 4) mobile ionic charge Q_m, which is a space charge largely caused by alkali ions such as sodium. These alkali ions have been a major problem due to the fact that the movement of these charges is strongly biasing dependent. They are mostly introduced by processing surroundings. Another possible contribution to the charge accumulation comes from secondary electron emitted by the dielectric on one electrode and attracted to the other electrode under negative bias voltage. These electrons become trapped by surface states.

An electric-field analysis was conducted here to explain the charging effect. Two electrical fields E_g and E_i exist in the air gap with the distance t_g and in the dielectric layer with the thickness t_i respectively. The direction of these two electrical fields corresponds to the polarity of the applied bias voltage V_p. The electric field E_g determines the electromechanical coupling of the transducer. The electric field E_i is considered parasitic since it actually reduces the achievable electrical field E_g in the air gap, when the bias voltage V_p is applied. The electric fields can be calculated using the equation [59]

$$E_g t_g + E_i t_i = V_p \tag{2-35}$$

Considering the electrical displacement for the surface area between the dielectric layer and the air gap, there is a second equation

$$E_i \varepsilon_i - E_g \varepsilon_g = 0 \tag{2-36}$$

where ε_g is the dielectric constant of vacuum (≈ 1). ε_i is the dielectric constant of the dielectric layer. Solving Equations (2-35) and (2-36), E_g and E_i can be expressed as:

$$E_g = \frac{V_p \varepsilon_i}{t_g \varepsilon_i + t_i \varepsilon_g} \tag{2-37}$$

$$E_i = \frac{V_p \varepsilon_g}{t_g \varepsilon_i + t_i \varepsilon_g} \tag{2-38}$$

Using the geometric parameters listed in table 2.3, the calculation for these electrical fields and the voltage drops can be obtained when a bias voltage V_p is applied to the CMUT.

44

PARAMETERS	VALUES
Dielectric thickness t_i	0.15 μm
Gap distance t_g	0.2 μm
Dielectric constant ε_g	1.0
Dielectric constant ε_i	5.7
Bias voltage V_p	100V
Voltage drop at air gap	88.3V
Voltage drop for dielectric layer	11.7V

Table 2.3 the voltage drops across the gap and dielectric layer

When a positive bias voltage V_p is applied to the CMUT, the charges move towards the surface between the dielectric layer and the air gap. The accumulated charge at the transition from the dielectric layer to the air gap is [59]

$$\sigma = \frac{dQ}{dA} \qquad (2\text{-}39)$$

This surface charge significantly affects the electrical flux density between the dielectric layer and the air gap. Therefore, equation (2-36) has to be rewritten as

$$\frac{\sigma}{\varepsilon_0} = E_i \varepsilon_i - E_g \varepsilon_g \qquad (2\text{-}40)$$

E_g and E_i can be rewritten as:

$$E_g = \frac{V_p \varepsilon_i \varepsilon_0 - \sigma t_i}{\varepsilon(t_g \varepsilon_i + t_i \varepsilon_g)} \qquad (2\text{-}41)$$

$$E_i = \frac{V_p \varepsilon_0 \varepsilon_g + \sigma t_g}{\varepsilon(t_g \varepsilon_i + t_i \varepsilon_g)} \qquad (2\text{-}42)$$

These equations demonstrate the parasitic effect of the charges. The electrical field E_g in the air gap of the transducer is further reduced by this surface charge, which results in lower electromechanical coupling.

When the applied bias voltage was turned down to zero, the surface charge σ in the transition range between the dielectric layer and the air gap is still active. The two electric fields in the air gap and in the dielectric layer will remain for a certain period of time and are rewritten as [59]:

$$E_g = \frac{-\sigma t_i}{\varepsilon_0 (t_g \varepsilon_i + t_i \varepsilon_g)} \tag{2-43}$$

$$E_i = \frac{\sigma t_g}{\varepsilon_0 (t_g \varepsilon_i + t_i \varepsilon_g)} \tag{2-44}$$

Notice that the polarity of the electric field in air gap in equation (2-43) is opposite to that of (2-41).

A most straightforward method to decrease the effect of dielectric charging is to use a bipolar AC rather than DC voltage actuation [60]. However, the charging effect cannot be eliminated completely and more complex actuation electronics are required. The other way to reduce the effect of the dielectric charging is by controlling the electrode and dielectric geometry, mainly the width of the gaps with exposed dielectric between electrodes and the thickness of the electrodes. Smaller gap can decrease the magnitude of charging induced drift and shorten the saturation time, resulting in reduced adverse effects of charging on stability. At the same time, careful consideration of operating conditions and design trade-offs are required before determining on the ideal gap size for a given application.

2.5 The Design of CMUT Cell

The conventional CMUT structure using silicon nitride as membrane material can be found in [14-16]. By contrast, the membrane material chosen here is polysilicon (simplified as poly). Nitride can maintain a higher internal (residual) stress (compressive or tensile, depending on the fabrication condition) than poly. The relatively large residual stress will increase the stiffness of the membrane, deteriorate the performance, and result in reliability problems. In addition, poly has a low aging rate and can reduce the complexity of the fabrication process.

The parameters of the CMUT structure include the thickness and lateral dimensions (the radius or the length) of the membrane and the gap distance beneath the membrane. The dimensions can be determined using FEA frequency analysis. The gap distance should be chosen to be small enough to yield good performance, but big enough so that the membrane does not touch the substrate when the membrane is deflected under ambient pressure. Another parameter that affects performance is the size of electrodes. Recent studies showed that electrodes with half the radius of the membrane will have broader bandwidth [40, 61]. When the electrode radius increases beyond half of the membrane, the fixed capacitance increases as well, but the increase in the free capacitance is relatively slow compared to the fixed capacitance. When using a doped poly membrane as an electrode, the size is fixed and not available for adjustment. An alternative approach is to change the bottom electrode size so that the peripheral electric field can be reduced and the influence of the parasitic capacitance can be reduced.

Although eliminating the dielectric layers between the two electrodes can reduce charge trapping, it will bring about another problem – short electric circuiting if operating

beyond pull-in point is needed. This problem can be overcome by using a novel structure – dielectric posts (columns) on the membrane as shown in Figure 2.10. It is worth noting that the real size of each dielectric column is about 1.5µm in diameter, much smaller than shown in the drawing.
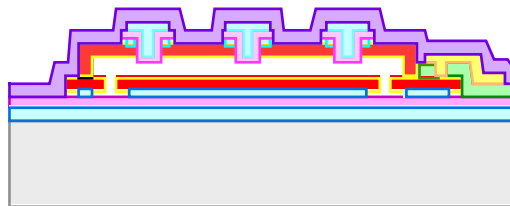
Figure 2.10 the cross section of the cell with dielectric post (the size of the post is represented disproportionally to the whole structure).

The topography of the membrane has some effects on the performance as well. Researchers [62] have done the Finite Element Analysis using a similar structure to that shown in Fig 2.11 a). The vertical membrane displacement has been significantly improved by etching trenches around the peripheral edges. This structure yields larger displacement more uniformly in the center. But the complexity of the fabrication of the structure also has been increased.
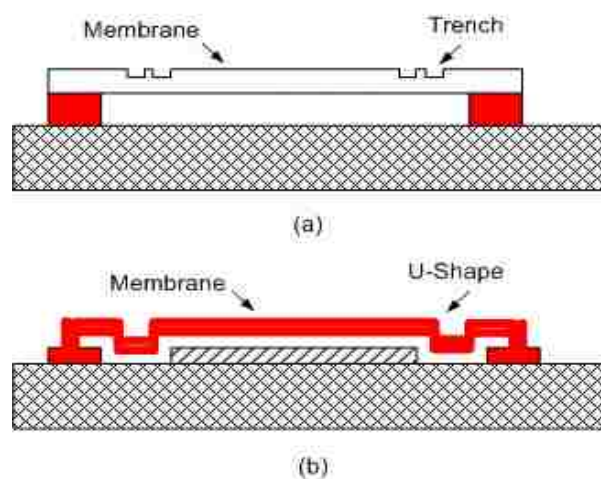
Figure 2.11 Membrane topography

In Figure 2.11 b), U-shaped membrane topography can be self-formed during the fabrication. No extra mask is needed. This U-shape at the edge region gave more flexibility for the deformation of the central part of the membrane. It allows more piston like transducer behavior and yields larger displacement more uniformly in the center.

2.6 Summary

In this chapter, the fundamentals of CMUT cell were addressed in detail. The simplified 1D model was used to derive the expressions for the electrostatic forces and output currents. Parameters such as capacitance and impedance were discussed in detail. Their influences on the device performance were also analyzed. It is demonstrated that the device performance not only depends on the medium, but also relies on the geometrical parameters of CMUT cells. A new structure of CMUT was proposed. This CMUT has a non-uniform membrane to increase the bandwidth, and the dielectric posts to reduce the charge-trapping problem. This chapter lays the foundation for CMUT fabrication as well as applications as described in the next chapters.

CHAPTER III

CMUT FABRICATION

3.1 Background

CMUT devices and arrays are fabricated using standard silicon IC fabrication technology [101]. Fabrication approaches can be categorized into two main groups: 1) surface micromachining technology and 2) wafer bonding technology [63]. For surface micromachining technology, the cavity underneath the membrane is created by depositing or growing a sacrificial layer on the carrier substrate. After the membrane deposition, the sacrificial layer is removed with an etchant.

In the wafer bonding method, the thin single crystal silicon layer of a silicon-on-insulator (SOI) wafer is used as the membrane material and silicon dioxide is used as the insulator and support structure. The gap cavities are formed on a second silicon wafer by etching the silicon using KOH. The wafer with cavities is then bonded with the SOI wafer. The active silicon layer on the SOI wafer will be used as CMUT membranes. The backside of the bonded wafer is ground and etched back to the buried oxide (BOX) layer of the SOI wafer to form the membrane. This BOX layer is then removed with buffered HF [64].

The wafer bonding technique involves fewer process steps than the surface micromachining method, which reduces the process turnaround time and potentially increases the yield [63]. However, there are some problems that prevent us from using this technique in this research. First, the cavity is defined by silicon etch using KOH. The KOH etching rate is not consistent. It is difficult to control the cavity depth without using

an etch-stop layer. The variation of the cavity depth will result in inconsistencies from device to device. Another disadvantage of the wafer bonding technique is that it requires an SOI wafer that has much higher cost than the common wafers.

3.2 Fabrication flow of CMUT

Polysilicon was chosen for the CMUT membrane material for multiple reasons as discussed in Chapter II. The fabrication steps are different from that of conventional nitride membrane CMUT. Figure 3.1a) illustrates the process flow for this design. The details of the fabrication process are contained in Appendix A. For comparison, the major difference with the traditional fabrication process will be discussed in this section.
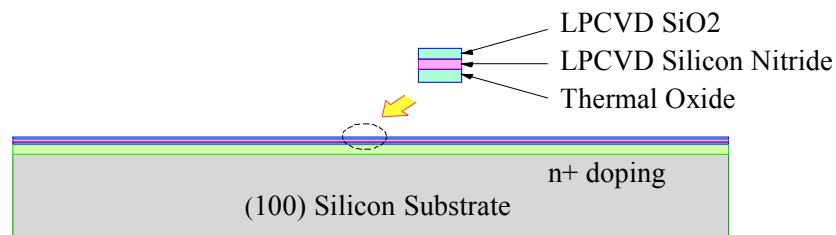
a) Dielectric stack
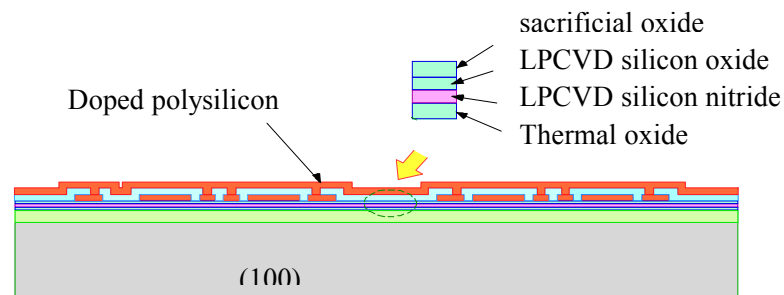
b) First Poly layer (POLY0) was deposited, doped and patterned. The sacrificial layer was deposited before the second layer of structural polysilicon (POLY1) is deposited, doped, and annealed

51

Top view

Poly membrane

LPCVD Oxide
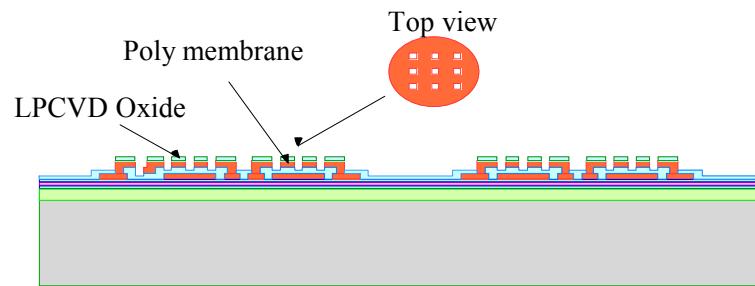
c) 500Å Oxide layer was deposited; the oxide and the second structural polysilicon were patterned

Poly membrane
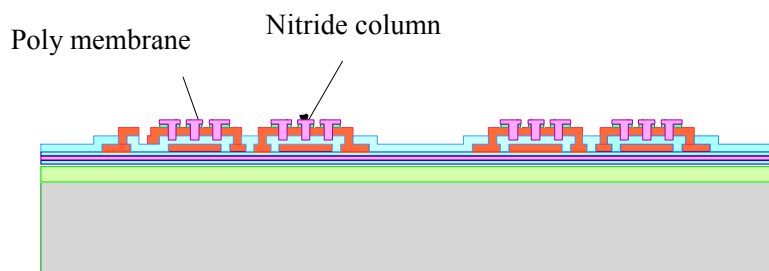
Nitride column

d) Dielectric post (silicon nitride column) formation. The nitride film filled into the dimple pits. This layer was patterned.

Nitride column

Poly membrane

LPCVD Nitride

Thermal Oxide
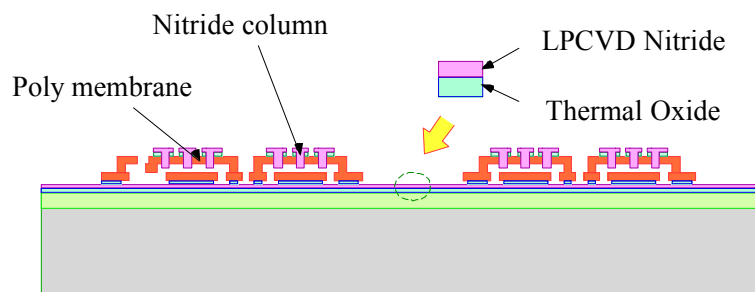
e) A wet HF:DI H$_2$O etching was used to remove the sacrificial oxide to release the POLY1 microstructures from the substrate
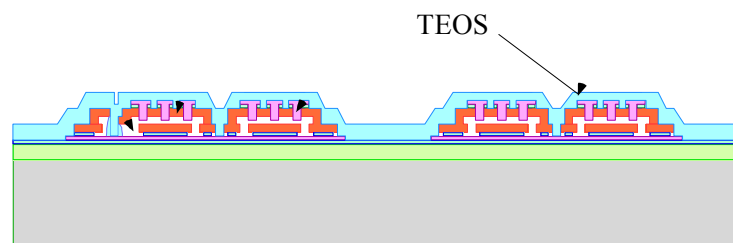
TEOS

f) Sealing the release holes with TEOS (PECVD Oxide); these thin-film deposition processes were performed in vacuum

Vacuum Chamber   TEOS
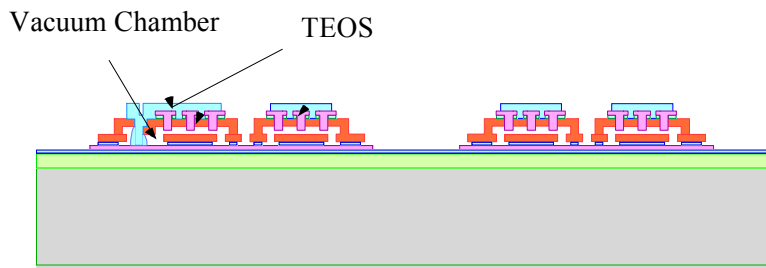
g) PECVD oxide (TEOS) patterning.

Metal interconnect
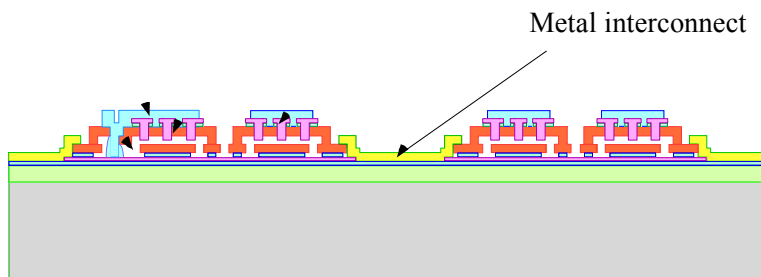
h) Metal interconnects were deposited and patterned

Vacuum Chamber   Poly membrane   Metal interconnect
TEOS   polymer
              Nitride column
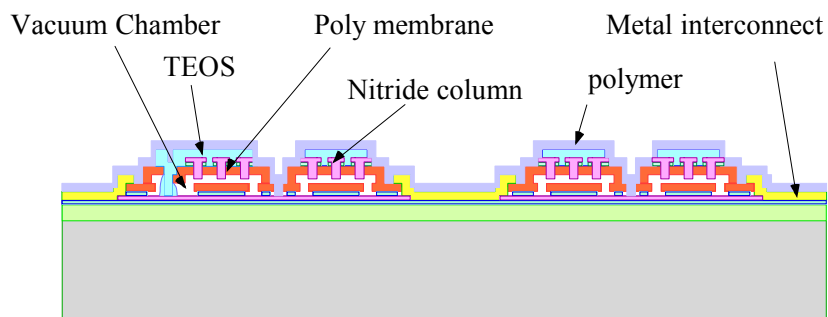
i): A polymer passivation layer was deposited and patterned

Fig 3.1 the schematic of the process flow

3.2.1 The Electrode Definition

In typical fabrication procedures, the substrate surface is heavily doped and acts as the bottom electrode. This bottom-plate parasitic capacitance from the doped layer to substrate degrades the performance of CMUT. In this research, dielectric layers combined with 2µm thick thermal oxide and 2500 Å LPCVD nitride served as structural

buffer to reduce the parasitic capacitance. This LPCVD nitride layer above the thermal oxide also prevents the oxide from being etched in the release step (see Figure 3.1a). A very thin LPCVD oxide (500 Å) is deposited right after this deposition step. This oxide layer is used to alleviate the charge buildup in nitride since nitride is more prone to trap charges than oxide during operation. Although the edge of this layer is exposed to the HF etchant in the follow-up releasing step, experiments showed that this would not cause severe damage to the structure.

The first LPCVD low stress poly (POLY0) is then deposited followed by phosphorous doping in POCL3 gas. The sheet resistance of doped poly is 13 ohm/sq. This poly layer will be lithography patterned and dry etched. Next, LPCVD PSG (Phosphosilicate Glass) is deposited as a sacrificial layer. The thickness of PSG is chosen about 300 Å thicker than the required gap distance because the follow-up PSG densification will condense the PSG and reduce the thickness. The densification is to prevent surface bubbles and reflowing of PSG in the subsequent high temperature processes. This PSG film is then patterned and dry etched to open the anchor trench for the second LPCVD poly (POLY1) deposition. This POLY1 film then goes through a heavy phosphorous doping and annealing and will act as the membrane (top electrode) (Figure 3.1b). Since the membrane itself is conductive, no metal is needed as the electrode.

3.2.2 The Sacrificial Layer Release Etching

After membrane deposition, the next important step is to release the sacrificial layer beneath the membrane to form the cavity. Before doing this, several process steps are conducted as shown in Fig 3.1 c-d). 500 Å LPCVD silicon dioxide is deposited first.

This layer vertically separates the POLY1 structures from the silicon nitride film that is to be deposited in the subsequent step. This top oxide and the second structural poly (POLY1) are patterned using a photolithography process and a dry etching. This etching process will etch through the POLY 1 layer and over etch into the sacrificial oxide to form 300-500 Å deep pits into the sacrificial oxide. These pits are filled with silicon nitride to form insulating columns (post) on the POLY1 membrane. This nitride layer also needs to be patterned. Dry etching is conducted to remove the nitride from the releasing-hole area. The close-up view of the dielectric post is given in Figure 3.2. These dielectric posts will help prevent the membrane from pulling down to the bottom electrode.

In the case of silicon nitride membrane in conventional design, the release etchant is potassium hydroxide (KOH), which has a good selectivity between polysilicon and Si_3N_4 (~400000:1). According to [32], this is a time-consuming step taking up to several days. The slow rate is due to the narrow and thin etch channels that limit the diffusion of KOH. Obviously, the long etching process is not desirable. In addition, the KOH etchant contains potassium ion, which is incompatible with CMOS process. It causes inconvenience in fabrication and makes it less possible to integrate CMUT with CMOS.

An LPCVD Low-temperature oxide (PSG) was chosen as the sacrificial layer. The PSG sacrificial layer is released in 49% straight HF solution (or 1:1 DI H20 and HF). The etch rate of PSG in straight HF is about 36000 Å /min. The total time of releasing process varies according to the dimension of the device. It normally takes 3 to 4 minutes for the membrane with 80 um diameter using straight HF. The partially released

membrane is shown in Figure 3.3. Therefore, the releasing is much faster than that of KOH. HF also has the advantage of being compatible with CMOS processes.
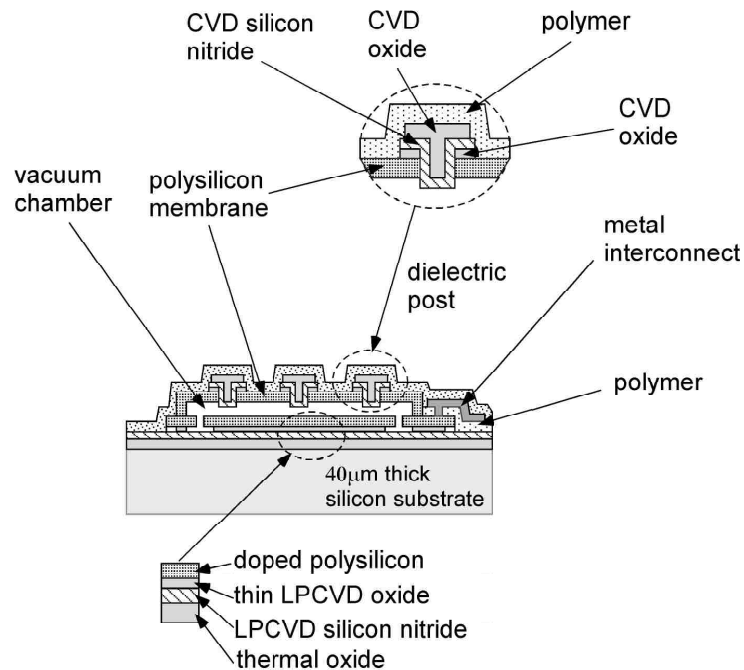
Figure 3.2 the cross section of dielectric post

A critical step in the release process is the drying of fluid inside the cavity after the wet etching process. When all the sacrificial material is removed, the wet etchant is removed and replaced with DI water. Then the DI water evaporate. Stiction problems arise during the drying process because the capillary forces from surface tension pull the membrane toward the substrate. If the membrane is not sufficiently stiff, these forces cause an irreversible pull-down of the membrane.
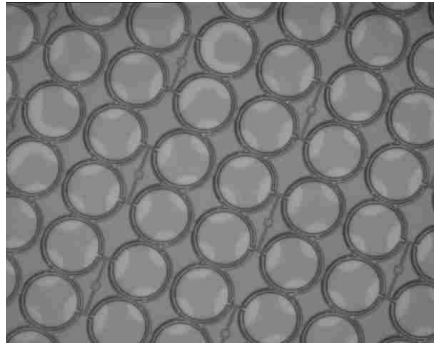
Figure 3.3 80um Membrane after 2mins releasing in Straight HF.

A so-called—Supercritical dry process was used to avoid this problem. The basic working principle is to replace the DI water with liquid carbon dioxide before drying at a critical temperature and pressure. At the proper temperature and pressure, carbon dioxide is in the supercritical phase in which there is no liquid-vapor interface, and therefore no capillary forces are present. In the cases where the membrane was stiff enough to overcome the capillary forces, the supercritical CO_2 steps were not necessary to prevent stiction. But it is still helpful to clean devices and purge contaminants or etching by-products from the gap.

3.2.3 Membrane sealing and metal interconnect deposition

Sealing the gaps after the release step enables immersion operation of CMUT by preventing the hydrolysis of water in the cavity under high electric fields and loading at the back of the membrane. Sealing also improves the performance by decreasing the loss and Brownian noise due to squeeze-film effects. The conventional sealing procedure adopts LPCVD nitride /oxide as the material. LPCVD nitride / oxide can give a comparably low pressure (~200 mTorr) for the cavity after sealing. The problem is that the LPCVD nitride has a very low sticking coefficient, which means a molecule will not stick to the wafer surface immediately, and some amount of nitride will deposit into the

cavity. A long release channel is always required in order to alleviate this problem. It is reported that approximately one-third of the initial cavity height will remain after the etch holes are completely sealed for the long release channel device [32]. This long release channel reduces the active area and degrades the performance. Another challenge is, the wafer must be pre-furnace cleaned before LPCVD process, which is not allowed after supercritical CO_2 drying because the cleaning solutions will enter into the cavity during this cleaning process, and will cause stiction problems again.

PECVD oxide (TEOS) is chosen as the sealing material in this research. It has no serious sticking problem; therefore the long-sealing channel is not required. The tradeoff of PECVD oxide is that the process pressure is 2.6 Torr that means the vacuum level inside the cavity after sealing is lower than that of LPCVD nitride. About 2 um thickness PECVD oxide (380 ˚C) is deposited to seal the releasing hole. A photolithography process and an etch process is used to pattern this sealing oxide. This etching process is performed in two steps to minimize the etch undercut. A time controlled plasma dry etch removes about 90% of the oxide layer using CF4+CHF3 gas. This etching process has a poor selectivity between SiO2 and polysilicon and also increases the surface roughness. Thus, to maintain the surface smoothness, the remaining 10% of the oxide is wet-etched in BHF solution with minimum over-etching time. The sealing oxide (TEOS) is removed except in the areas around the release hole and at the center of the membrane (Figure 3.1 f-g). As discussed in chapter II, the oxide left at the center of the membrane forms the boss, which improves the frequency response of the membrane.

The next step of the membrane sealing is negative tone photo-resist coating and patterning for metal liftoff and Cr/Au sputtering (400 Å /4000 Å). Cr is used to improve

adhesion. While thermal evaporation is used more commonly in the lab, sputtering can provide a better step coverage. The sputtered metal layer goes through the standard liftoff process before passivation. (Figure 3.1 h-i).
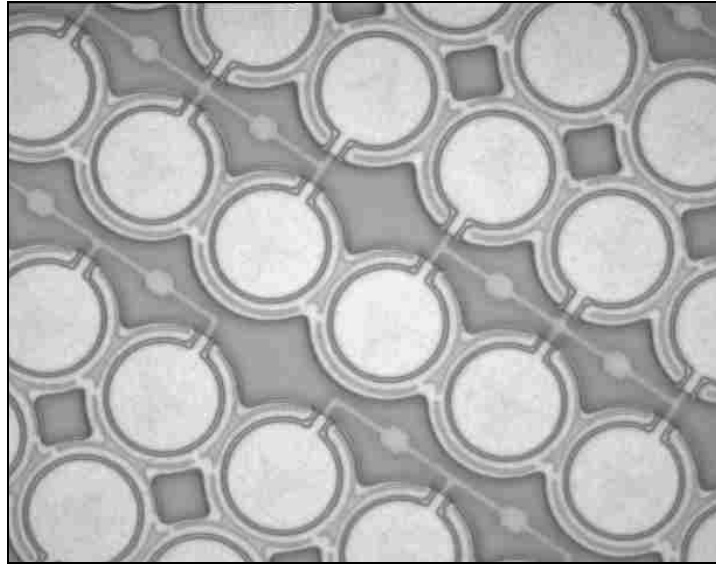
Figure 3.4 photograph of the sealing membranes, no boss is presented on the membrane

Figure 3.4 shows the SEM picture of the membrane without bosses after the above processes were finished. Forming bosses does not require extra process steps. They are formed during PECVD oxide deposition and patterning. This step also sealed the release holes. Figure 3.5 a) shows the cross-sectional schematics of a CMUT with a boss membrane. The cross section of a uniform thickness membrane without boss is shown in Figure 3.5 b) for the purpose of comparison. The picture of the CMUT with bossed membrane is shown in Figure 3.6.
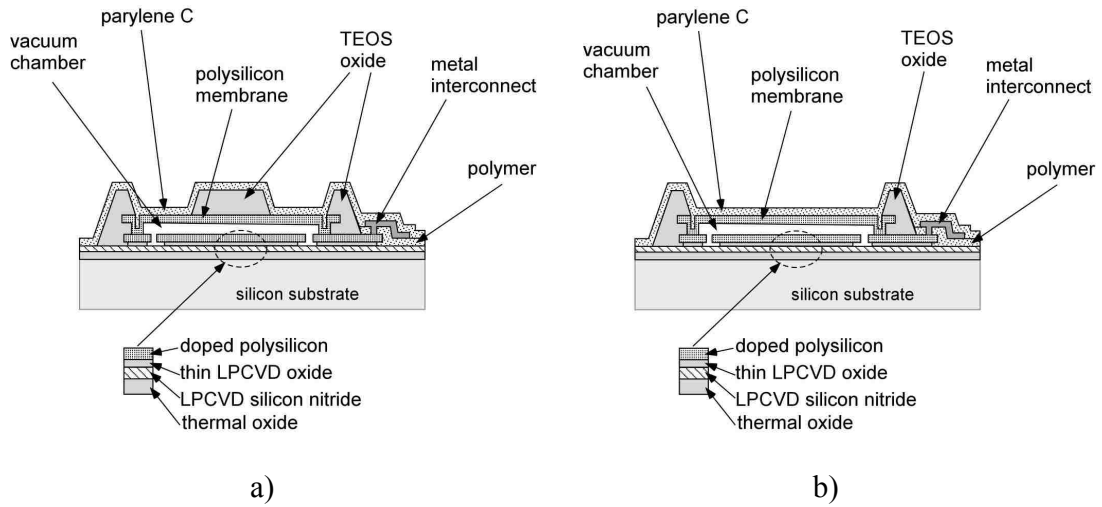
Figure 3.5: (a) Schematics of a CMUT with a bossed membrane. (b) Cross-section of a uniform-thickness-membrane CMUT built using the same fabrication process.
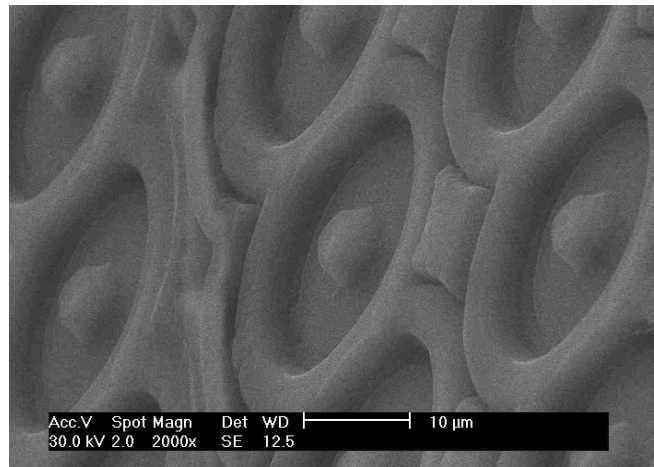
Figure 3.6 SEM of the CMUT with a bossed membrane

3.3 CMUT Cell measurements

Some primary measurements were performed after CMUT cells were sealed. A probe station was used for some of the measurements since the devices had not yet been wire-bonded.

3.3.1 The CMUT Membrane Displacement testing
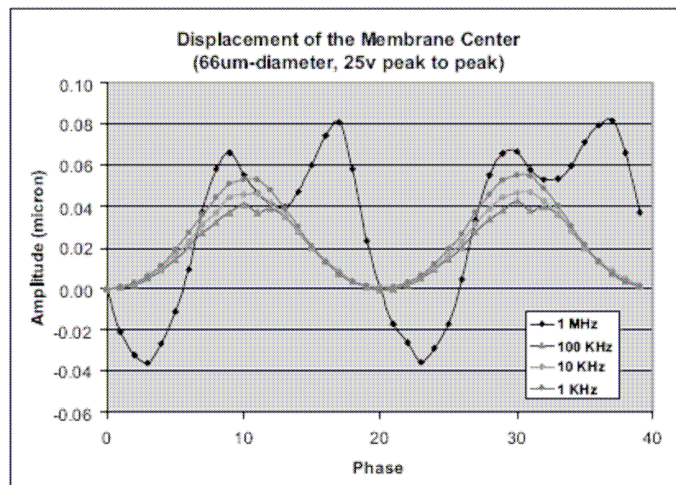
a)
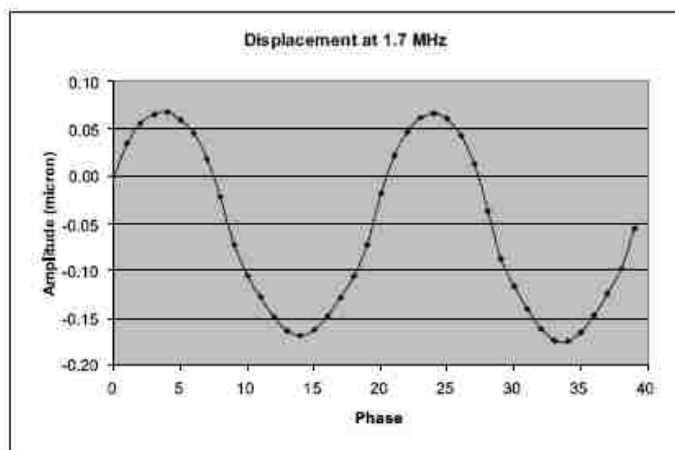
b)

Figure 3.7 the displacement at the center of a 66um diameter ultrasound emitter membrane under a 25V peak-to-peak electrical excitation at different frequencies.

The CMUT membrane displacement testing was conducted first. The device was tested in water using a hydrophone. The output of the hydrophone was connected to a high-gain bandpass amplifier before it was read out. UMECH MEMS motion analyzer (MMA) G2 was used to measure the frequency and amplitude response of the membrane

under electrical excitation at different frequencies and voltages. Figure 3.10 shows the displacement at the center of a 66um diameter membrane under a 25 V peak-to-peak electrical excitation. Figure 3.7 a) shows that the maximum peak amplitude (negative, pull down) is about 400 Å. While in Figure 3.7b) the membrane was vibrated at its harmonic frequency (1.7MHz). The maximum pressure generated was about 0.34ATM (34KPa).

3.3.2 The capcitance measurement
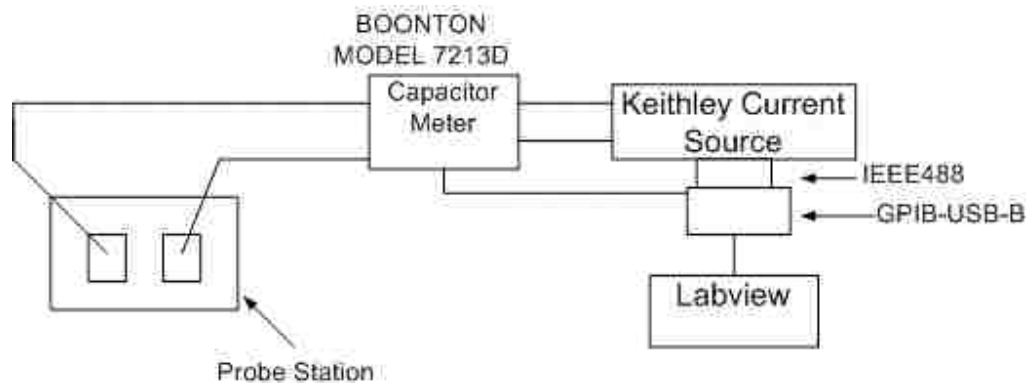
Figure 3.8 Set-up for CMUT capacitance Measurement

It has already been shown that the capacitance of the CMUT is proportionally related to the square of dc bias voltage (see equation 2-23). The C-V measurement was done in air using the experimental setup shown in Figure 3.8. The C-V curve was obtained as shown in Figure 3.9. the parameters of the device under test are shown in table 3.1.

PARAMETERS	VALUES
Membrane radius (μm)	46
Membrane thickness (μm)	1.5
Gap distance (μm)	0.2
Number of cells	100

Table 3.1 The parameters of CMUT

At zero bias voltage, the measured capacitance is about 29pF, which is much larger than the calculated value (20pF for 100 cells connected in parallel). This is due to various parasitic capacitance associated with our unoptimized structure. As mentioned in Chapter II, parasitic capacitance arises from the stray capacitance to the substrate at each of the transducer terminals in conjunction with the substrate contact resistance. These parasitic capacitances are independent of bias voltage and have weak frequency dependence compared to the membrane resonance. Due to the limit of the hardware setup, we could not increase the bias voltage to the point of membrane collapse. For comparison, the calculated value of the capacitance was shown in the plot.
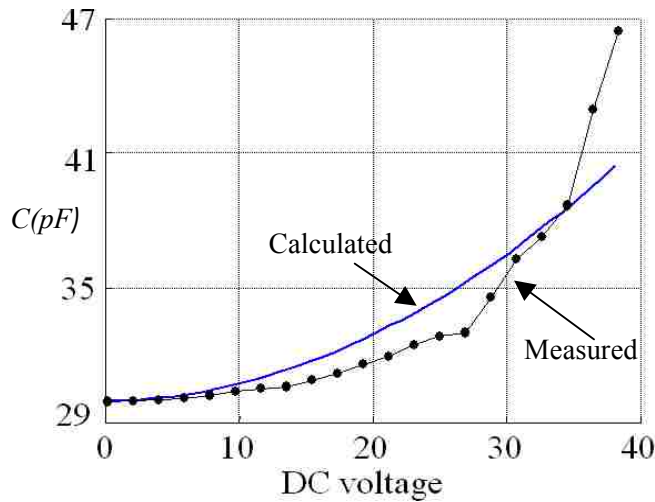
Figure 3.9. Capacitance vs DC bias voltage

The coupling coefficient K_T^2 was determined by using equation (2-33). To obtain K_T^2 from the capacitance versus bias voltage curve, a polynomial fit for the measured capacitance was performed to reduce the noise. The derivative of the capacitance was then calculated by using the fitted curve and was used for calculation of the electromechanical coupling efficiency K_T^2. The discrepancy is the result of the parasitic capacitance that is not accounted for by the model.
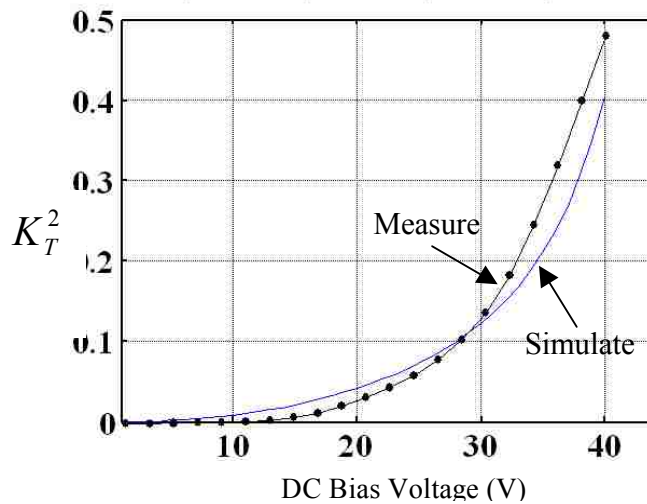
Figure 3.10 the coupling coefficiency

3.3.3 The input impedance measurement
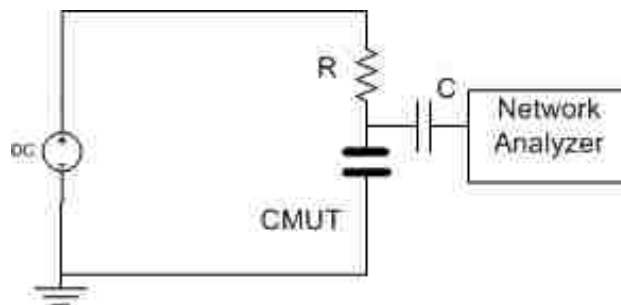
Figure 3.11 Experimental set-up for input impedance measurements

The electrical input impedance measurements provide a first look of the transducer acoustic activity. The measurements were performed with a vector network analyzer (Agilent 4396B, Agilent Technologies, Inc., Santa Clara, CA) that measured the complex input impedance of the transducer as a function of frequency. The measurement setup is shown in Figure 3.11. The network analyzer applies a small ac signal to measure the input impedance of the CMUT while sweeping the frequency. The capacitance works as a DC block to avoid the network analyzer being exposed to the high DC bias voltage supply.

The measurement was carried out in air. The plot in Figure 3.12 illustrated the measured and the simulated imaginary impedance.
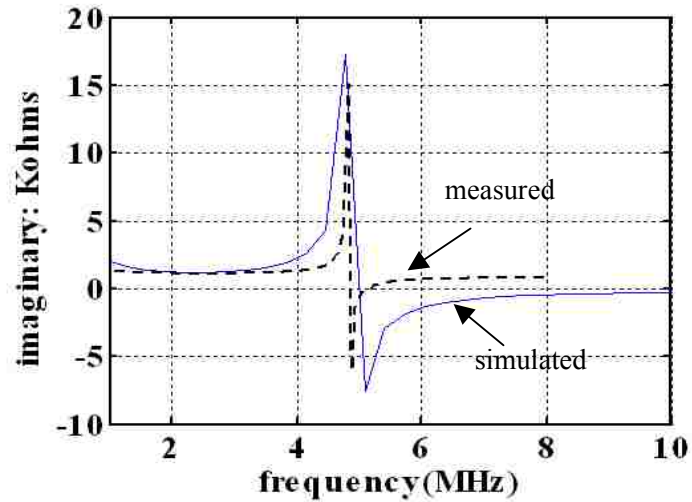
Figure 3.12 Electrical input impedance measurement in air in comparison with simulation results

3.4 Summary

In this chapter, the detailed fabrication steps were introduced, and were compared with the conventional CMUT fabrication process. This new fabrication approach can reduce the manufacturing turnaround time, and it is CMOS compatible. Using this fabricated CMUT cell, we obtained primary test results.

CHAPTER IV

CMUT ULTRASONIC TRASNDUCER ARRAY

4.1 Overview

Although acoustic waves with frequencies greater than 20KHz are considered ultrasound, medical ultrasound typically refers to frequencies from 1 to 10MHz or higher. As we have mentioned in chapter II, an ultrasonic wave is created and launched into the medium by electrical excitation of a transducer. The excitation signal is often a short pulse, modeled as amplitude modulated sinusoid:

$$p(t) = a(t)e^{-i\omega_0 t} \tag{4-1}$$

where $\omega_0 = 2\pi f_0$ is the carrier frequency.

This pulse wave is reflected and propagated back to the same or different transducer. A reflector at distance z from the transducer causes an "echo" pulse at time $t = \dfrac{2z}{c}$, where c is the sound velocity in the medium (1500m/s±5% in liquid or soft tissues of body, very different in air or bone), which relates the frequency f to the acoustic wavelength $\lambda = c / f$. Ultrasonic diagnostic imaging systems are mostly operated in this pulse-echo (reflection) mode. The images display the reflectivity of the object depending on the object shape and the material properties. Pulse echo systems can be classified as A, B, or M modes.

4.1.1 A-mode

The oldest and simplest type of pulse-echo ultrasound instruments uses A-mode (amplitude mode). This is performed by transmitting an ultrasonic pulse into the object

and the ultrasonic echoes received by the transducer are electronically interpreted and graphically displayed. A-mode has been used to produce one-dimensional ultrasound waves when in axial alignment.

4.1.2 B-mode

The primary use of B-mode (brightness mode) is diagnostic imaging of tissue structures. The image is typically made up of over a hundred separate lines of information. At the beginning of the sweep of the transducer, a pulse is fired and the echo data is received along that line. The system plots the echo data along that line based on depth, which is calculated by the time it takes for the echo to return. The brightness of the echo is determined by the strength of the reflection. The transducer then moves over a fraction of a degree, and fires the next pulse. This process is continued until the image is built up line by line.

4.1.3 M-mode

In M-mode (motion mode) the depth in tissue is displayed along the one axis while the other axes represent time. M-mode gives a real-time image of a moving structure in the beam direction. Due to the complexity of the data processing, the M-mode imaging is not the focus of this research.

4.1.4 Fundamentals of Transducer Arrays

Most ultrasonic transducers are used in the array scan format. A multi-element array will exhibit some unique characteristics since the elements mutually affect each other. Phase differences between neighboring elements occur when out-coming (transmitting) incoming (receiving) waves for each element can be specifically designed as a function of their spatial location. Therefore, aliasing in the spatial domain is a potential problem.

To minimize aliasing, the relation among the wavelength, the phase angle θ, and the inter-element spacing d must meet the requirement as expressed in the following Equation. [5]

$$\left|\frac{2\pi}{\lambda}d\sin\theta\right| \leq \pi \qquad\qquad (4\text{-}2)$$

or in a simplified format

$$\left|d\sin\theta\right| \leq \frac{\lambda}{2} \qquad\qquad (4\text{-}3)$$

Normally, setting $d \leq \dfrac{\lambda}{2}$ is preferred so that directions of arrival within a $\pm\pi/2$ range of angles can be unambiguously distinguished. Many scan formats of transducer arrays can be found in literatures. The most commonly used formats are linear phased array, annular array and two-dimensional array.

a) The Linear Phased Array

A linear phased array is usually about 1 cm wide and 1 to 3cm long, containing 32 to 128 elements. The ultrasonic beam generated by a phased array can be both focused and steered by properly delaying the signals going to the elements for transmission or arriving at the elements for receiving. Figure 4.1 (a) and (b) show how focusing and steering can be achieved with a five-element array. The pulse exiting the center element is delayed by a time R/c relative to the pulses exiting the elements on the perimeter, so that all ultrasonic pulses arrive at point P simultaneously. The disadvantages of the phased arrays are their complexity and presence of grating lobes.
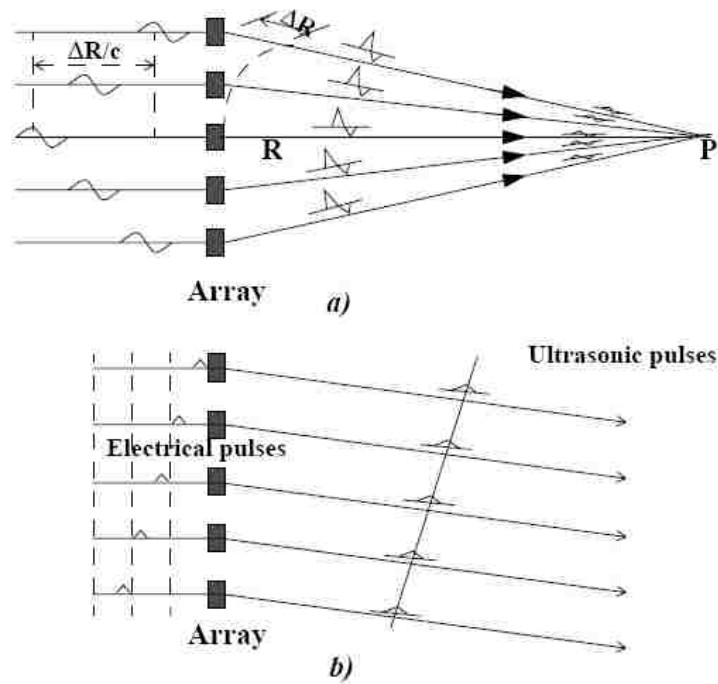
Figure 4.1 a) linear phased array focusing b) Steering of beam produced by linear phased array [65]

b) Two-dimensional arrays

The linear arrays can be focused and steered only in one dimension i.e. beamwidth improvements are restricted in the so-called azimuth direction. Since they only have a single element in the elevation direction, they cannot be steered and focused in this direction. Using two-dimensional arrays may alleviate this problem by arranging elements in a plane as shown in Figure 4.2.
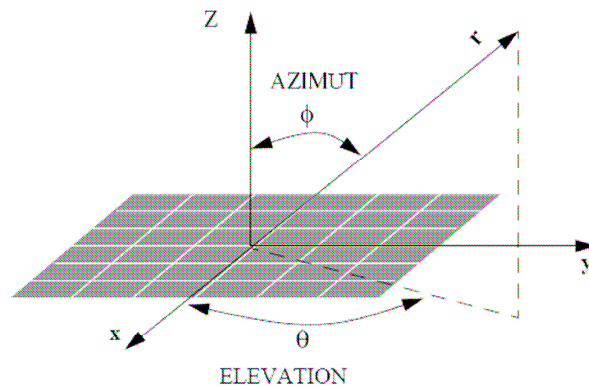
Figure 4.2 a two-dimensional planar array both with Cartesian and spherical coordinates given [66].

The array could also be curved in both azimuth and elevation dimension in order to allow focusing [67]. The major disadvantages of two-dimensional arrays are their great complexity, the large number of transducer elements, and the large amount of electronics that must be integrated, on the transducer array. It is very difficult to fabricate small two-dimensional arrays with piezoelectric materials for high-frequency applications.

c) Annular Array
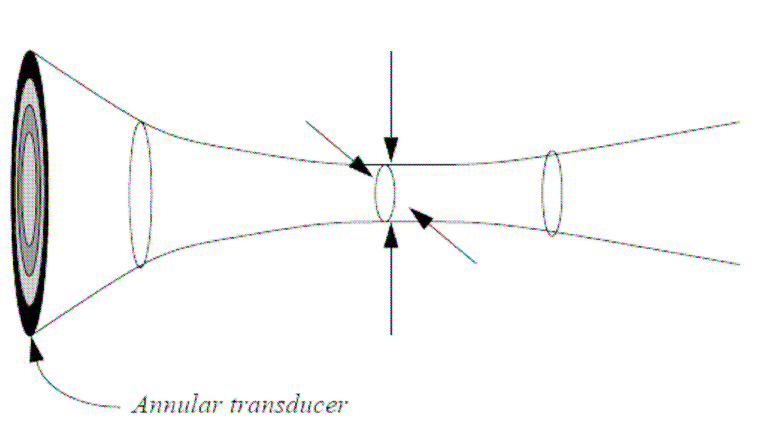
Figure 4.3 Symmetric electronic focusing in the plane and transverse to the plane of the beam with annular phase array [68]

70

The annular array (transducer) is often used for electronically focusing. Annular transducer are composed of a set of concentric circular elements (rings) as illustrated in Figure 4.3, where one obtains a steerable focus by individually delaying the signal to and from different elements. The advantage of an annular transducer is that the electronic focusing is the same in all directions normal to the beam, i.e., focus is symmetric.

4.1.5 Beamforming

The steering and focusing of arrays is performed by applying phase or time delays of the signals. This operation is called beamforming [69, 70]. Beamforming can be performed in the analog or the digital domain. High quality analog beamforming is becoming impractical for large numbers of channels, and digital beamforming has gradually become popular thanks to the availability of low-cost and high performance digital signal processors and ADC. Digital beamforming can greatly improve the delay accuracy and reduce the quantization noise and it allows higher frequency operation.

4.1.6 Image quality

The most important goal in biomedical ultrasound beamforming is to achieve "optimum image quality" such that the best clinical diagnosis can be obtained. Several parameters control the quality of an image such as lateral resolution, axial resolution, and frequency. Resolution is an important factor that determines the imaging quality. Resolution transverse to the beam is called the lateral resolution, and is determined by the width (main lobe width) of the beam (-6 dB beam width) [70].

The axial resolution of a transducer is determined by the spatial extent of the transmitted ultrasonic pulse .The image range resolution determined by the length of the transmitted pulse is given by:

$$\Delta r = c \frac{\Delta T}{2} \qquad\qquad (4\text{-}4)$$

where ΔT is the pulse length measured at -6 dB relative to the peak of the pulse envelope.

Higher frequency ultrasound devices obviously have a higher image resolution. In addition to resolution improvement, high-frequency ultrasound allows decreased aperture size and further miniaturization of the transducer. At higher frequencies, the wavelength becomes smaller. Therefore, the inter-element spacing (pitch) must be smaller. For a given frequency, an array with more elements will have a larger aperture and can have higher lateral resolution. The increased number of element however will also increase fabrication complexity because more interconnects are needed. For applications such as an intravascular ultrasonic system, the aperture size is limited to 1 to 2 mm and is typically no less than 10λ.

4.1.7 Far-field and Near-field Regions

For sound waves that have wavelengths comparable with the structures they encounter, diffraction causes the wave to deviate from straight-line propagation. Diffraction effects increase as the physical dimension of the aperture approaches the wavelength of the radiation. Diffraction of ultrasound radiation results in interference that produces dark and bright rings, lines, or spots, depending on the geometry of the object causing the diffraction [71, 72].

Because of diffraction, the acoustic beam emitted from the transducer will increase its diameter with distance and the field components in the beam will exhibit fine structure vibration, both along its length and across its diameter. Similarly to optics, there are two

distinct regions of interest, the near-field (Fresnel) region, and the far-field (Fraunhofer) region. Within the Fresnel region, the outside diameter of the beam remains approximately uniform; the beam spreads beyond this region [73]. Figure 4.4 illustrates the pressure profile of an unfocused circular transducer. The beam has little spreading within the near field and has a beamwidth about as wide as the diameter of transducer.
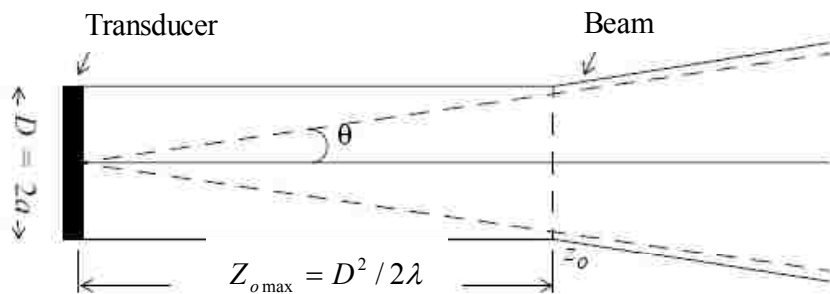
Figure 4.4 the pressure profile of an unfocused circular transducer [73]

The far field applies when the observation plane is far away from the aperture, i.e. when [73], [74]:

$$r_{01} >> \frac{a^2}{\lambda} \qquad (4\text{-}5)$$

4.2 Biomedical application

The prototyping of minimally invasive devices including a multi direction imager and an implantable blood flow meter is the main goal of this project. Biocompatibility is essential for the devices for implantable applications. A CMUT array in contact with living tissue or inside the conductive and corrosive environment of living animal must have a biocompatible material coated on the device and provide electrical isolation to the active areas of each element. This coating should also acoustically match the polysilicon membrane and the surrounding medium to eliminate unwanted reflections [75]. One good

candidate material is Parylene C. The flexural rigidity of Parylene C is low due to its small Young's modulus (2.7GPa). The low flexural rigidity reduces the effect of the coating on CMUT performance. Another choice is polydimethylsiloxane (PDMS). Compared to Parylene C, PDMS has an even smaller Young's modulus (0.5 MPa). Its acoustic impedance is about $2 \times 10^5 \, gm/cm^2 \, \sec$, that is close to the transmission medium such as the tissue fluid ($1.48 \times 10^5 \, gm/cm^2 \, \sec$). PDMS however cannot be lithographically patterned, and therefore cannot be easily employed since fabrication (patterning) of the coating material is needed. Furthermore, PDMS swells easily and degrades in the presence of organic fluids. Parylene C is stable and resistant to organic-solvent attack, being insoluble in all organic solvents up to 150°C. No biological degradation reactions have been reported thus far.

4.3 Blood Flow rate metering

The design and fabrication of the prototypes and related techniques will be discussed here. One is CMUT blood flow rate metering. Due to its miniature size, this tool can be implanted close to target vessels deep inside the tissue without introducing significant disruption to the tissue. A cross-sectional dimension of this probe-shaped ultrasonic transducer array could be smaller than one tenth the diameter of a laser Doppler flowmeter. Figure 4.5 shows the schematic of the ultrasonic blood flowmeter. On this array, the distance between the neighboring ultrasound transducer element and the pitch of the ultrasonic phase array are accurately defined by photolithography and dry etching. This high-precision array design makes it possible to accurately relate the phase shift of the echoes to the flow rate. Arrays comprising 24 to 32 ultrasonic elements have been

included in the design. Suspended polysilicon drum structures can be used as the transducing element to generate and sense ultrasonic waves.
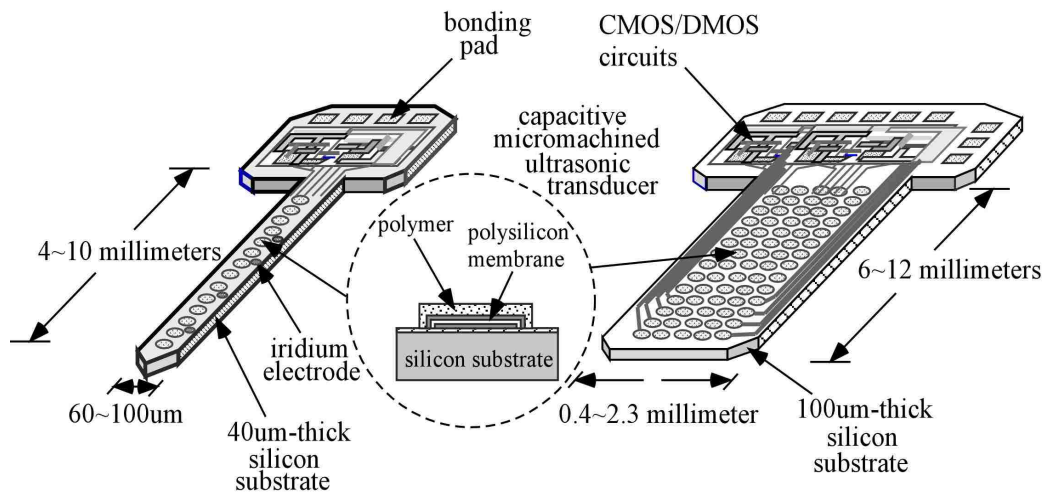
Figure 4.5: Schematic of the flowmeter probe.

The array fabrication builds upon the CMUT cell process steps described in Chapter III. For biomedical applications, especially for implantable devices, physical dimension must be miniaturized. After the fabricated CMUT cells are coated with 1μm Parylene C as passivation layer, the substrate is micro machined using a masked double-sided dry etching process as shown in Figure 4.6.
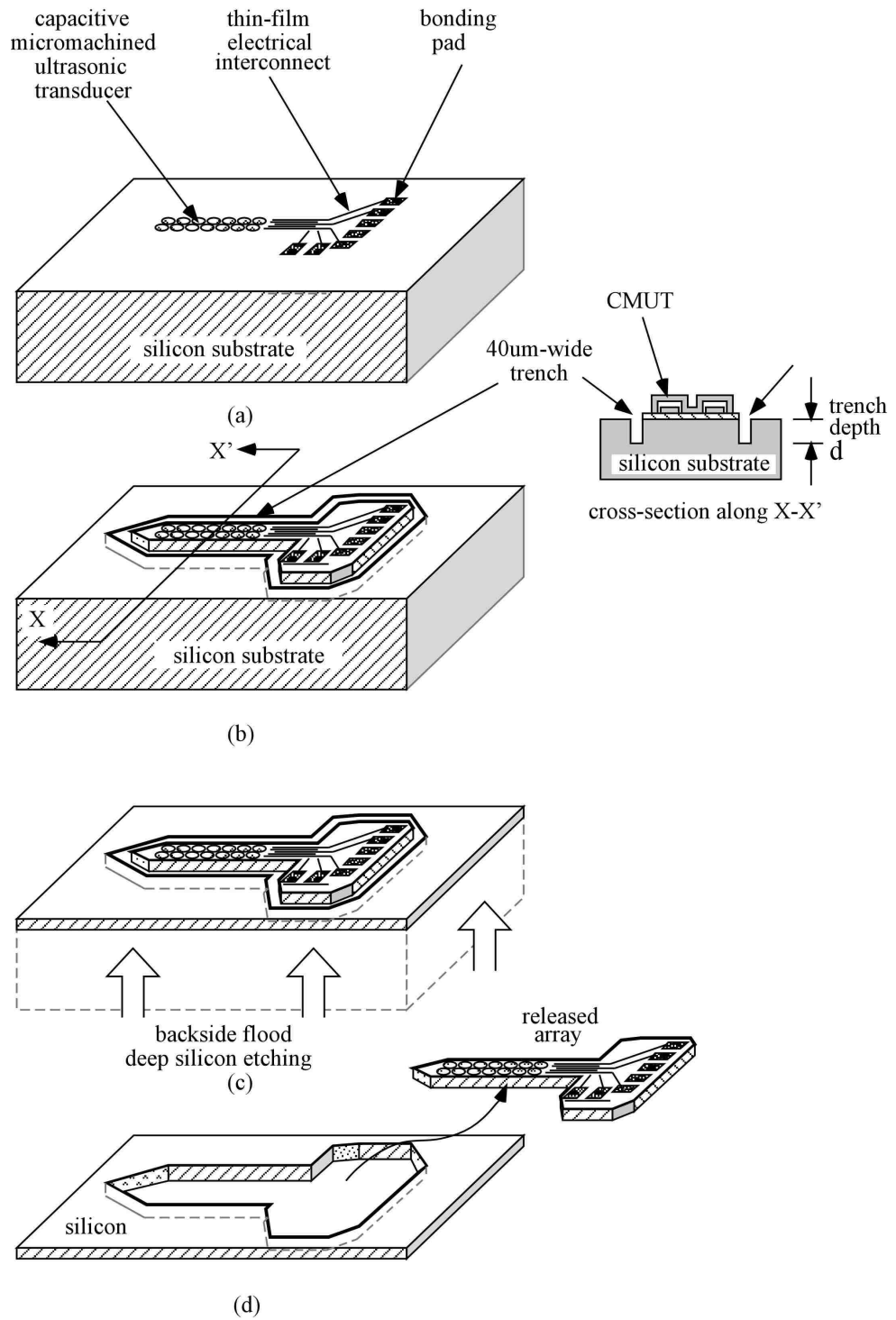
Figure 4.6 Process flow for the transducer array after the CMUT cell has been built up

In addition to miniaturization, micromachining the substrate thickness also reduces cross talk from Lamb waves [76] propagating in the substrate. This is important to improve signal-to-noise ratio and the device performance of the transducer. According to the experimental data, the lamb wave-related crosstalk level is reduced by 2.3 dB if the substrate thickness is reduced from 550μm to 40μm as used in this device design [76].

Figure 4.7 shows the SEM photograph of a one-dimensional ultrasound stimulator array. The probe-shaped silicon substrate is 40 μm thick, 80 μm wide and 2.5 mm long. Figure 4-10 is the picture taken after the array was bonded with PCB board.
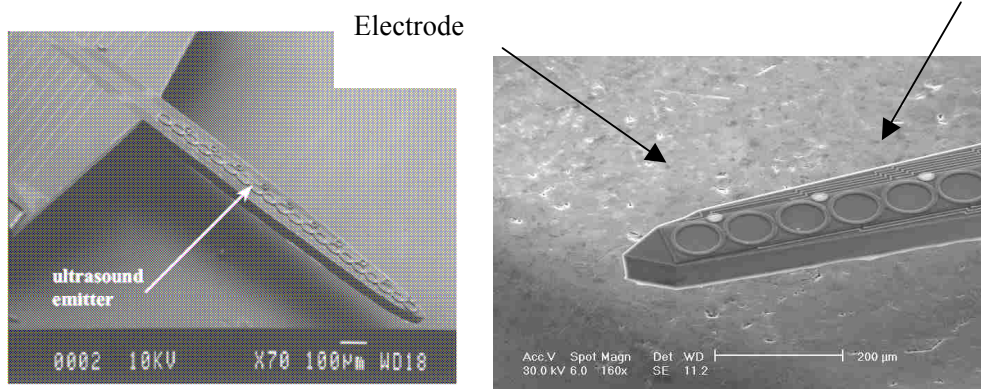
Figure 4.7 SEM photograph of a 1D ultrasound array. The smaller circular device beside the ultrasound membrane is the iridium electrode designed for electrical stimulation.
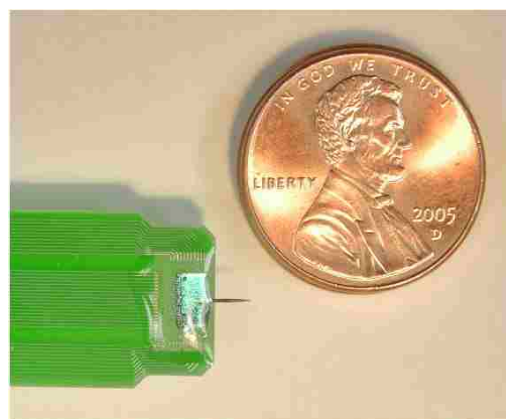
Figure 4.8 the ultrasonic transducer array after being bonded on a printed circuit board.

4.4 Multi-directional Imager

4.4.1 Design

Like all other imaging processes, resolution of ultrasonic imaging depends on the wavelength of the ultrasound used. High-resolution imaging requires use of high-frequency ultrasound which attenuates rapidly in tissue. Laboratory scale ultrasound platforms scanning from outside the body therefore have difficulty acquiring high-resolution images for anatomical structures deep inside the tissue. In order to obtain the anatomical details of organs/tissue and/or the complete view of internal structures at a region of interest inside the body, one approach is to invasively implant the ultrasonic transducer inside the body to generate the real time 3D images from the simultaneous multi-direction imaging.

The multi-direction-looking imager in Figure 4.9 has multiple sections of an ultrasonic transducers array. The device plates, each typically measure 0.8 mm (width) ×0.8 mm (length) ×100 μm (thickness), are folded into a three-dimensional prism structure.
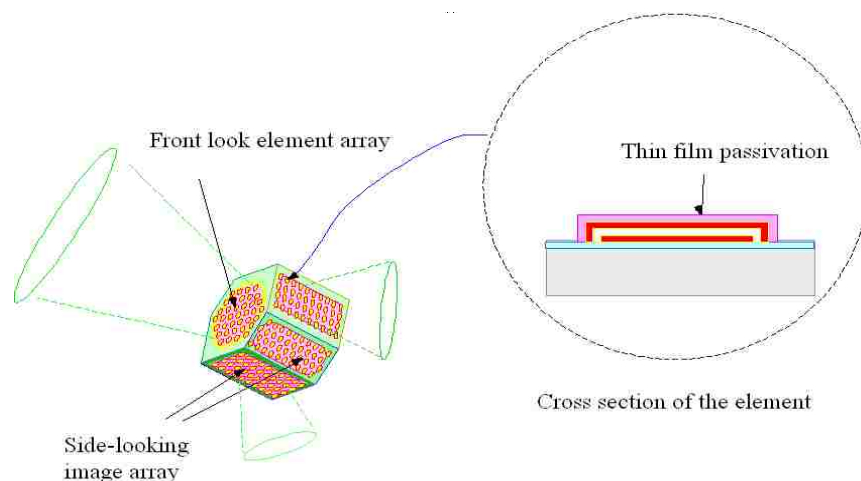
Figure 4.9: Monolithic 3D ultrasonic transducer array for multiple-direction-looking medical imaging.

This multi-looking imager has not only front-looking function, but also all-around side-looking imaging capability, and thus has the potential to provide a panoramic 3D real-time image for diagnosis.

4.4.2 Multi-dimensional imager fabrication

a): Device shape patterning.

Dry Etching

b): wet flood etching from the backside was used to thin the wafer to approximately 80-140 μm thick.

c): A photolithography and a dry etching from the backside to form deep trenches.
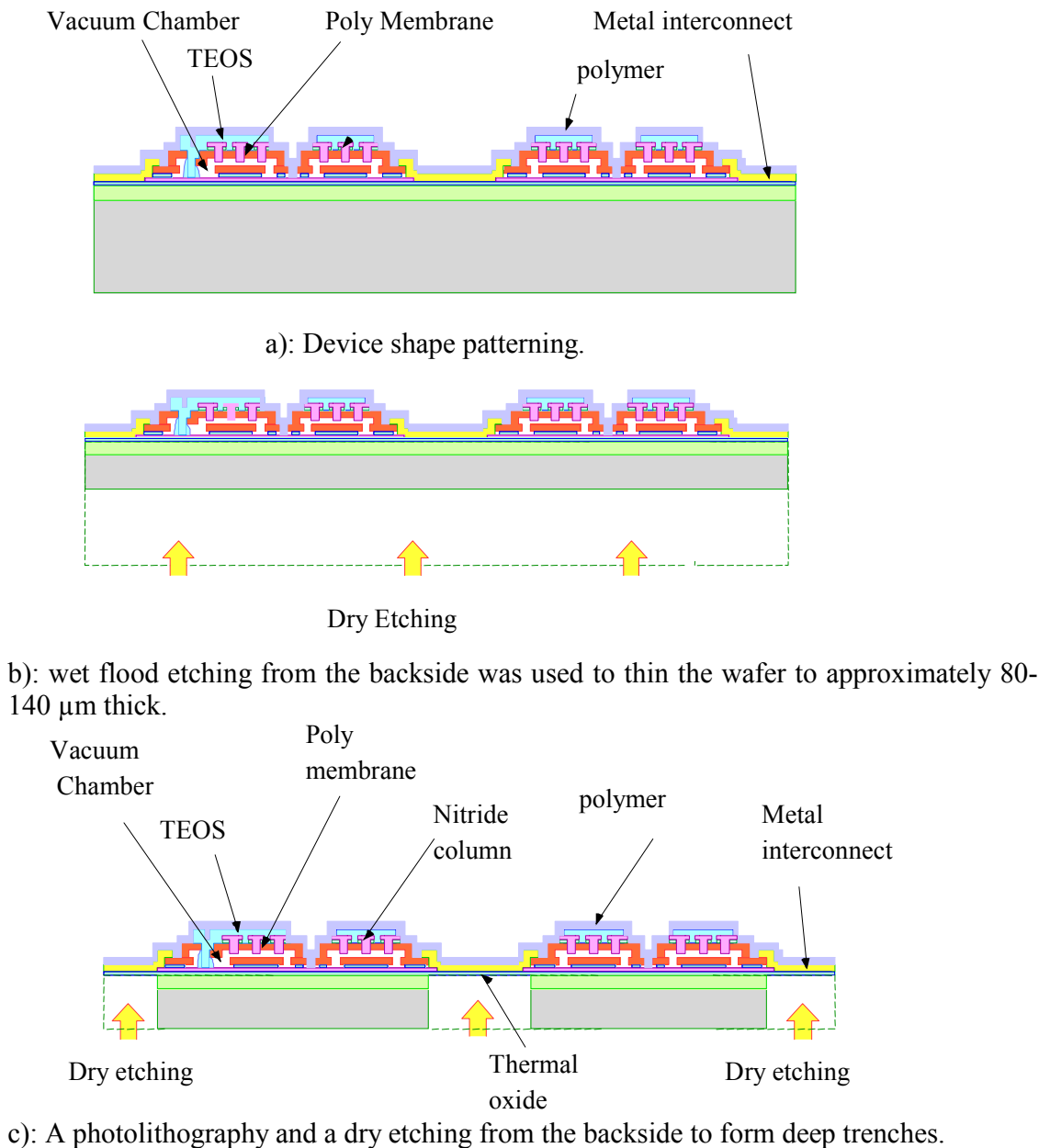
Figure 4.10 Process flow for multi-side imager

The CMUT cells were first coated with parylene C. Device shape was defined by lithography and then dry etched. A wet HF-Nitric flood etching from the backside thinned the wafer to approximately 80-140 μm thick. A glass carrier wafer protects the front side of the process wafer during this wet etching. This transparent glass wafer also allowed backside photolithography patterning to create a recess under the connection area after the thinning process. The silicon substrate under that area was then completely etched away. The plates were connected to each other by flexible parylene thin-film ribbons as shown in Figure 4.11. Figure 4.12 shows the individual patterns of plate for different scan-format. All photos were taken under an optical microscope.
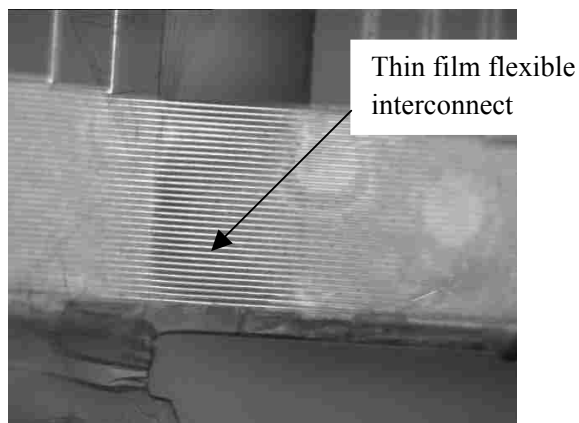
Figure 4.11 the thin film structure at the connecting area
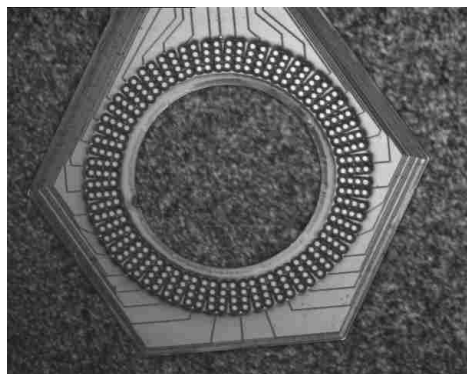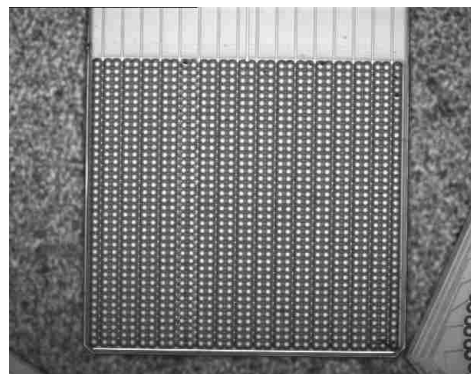
a) Annular array   b) 1-D array

Figure 4.12: The transducer array after dry etching release.

For CMUT cells with different shapes such as the circular or the square (rectangular), close-up photos of the cells are shown in Figure 4.13.
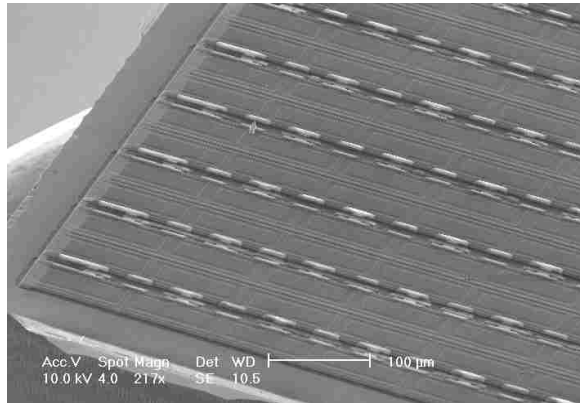
a) Rectangular shape
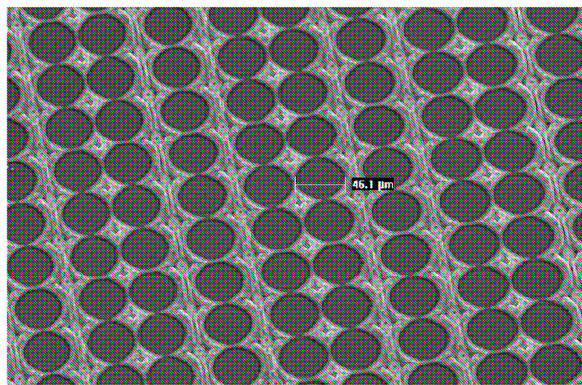
b) Circular shape
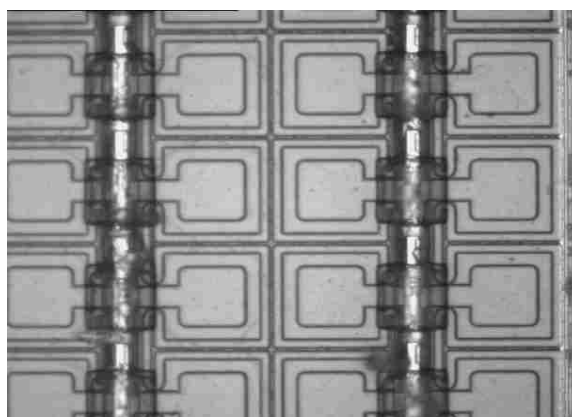
c) Square shape

Figure 4.13   photos of CMUT cell shapes   a) Rectangular shape, b) The circular shape, c) Square shape

4.4.3 Assembly

After substrate release, the device was folded and assembled into a silicon prism under a magnifying glass. It took about 20 minutes to manually assemble the planar array into a hexagonal silicon prism. It was found that the dielectric membrane could be bent more than 90º without damaging the thin-film electrical interconnects sandwiched in the membrane. However, multiple back and forth bending beyond 90º would break some of the electrical interconnects and cause open circuit connection failures. After assembly, the cavity inside the prism was filled with epoxy such that the whole structure was glued in one piece. The filling materials are the 1:1 volumetric mixture of Biphenyl Epoxy Resin (GC electronics, Rockford, Illinois) and the hardener (polymercaptan). After the filling process, the 3D imager prism was cured in oven for 30 minutes at 90ºC. Figure 4.15 is a photograph of a seven-imager prism after assembly. This device integrates one front-looking annular imager and a six side-looking planar imager array on a silicon prism for intravascular ultrasound imaging. The circular hole in the middle of the front-looking imager is for the guiding wire.
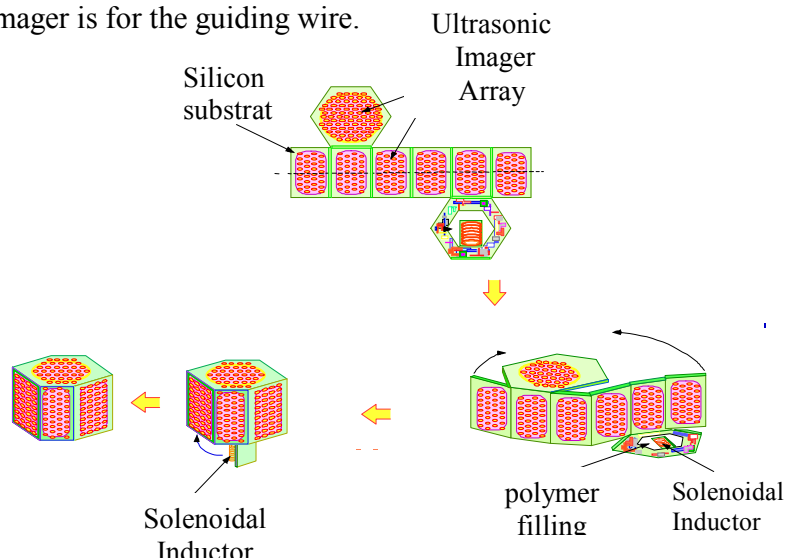
Figure 4.14 the assembly of the multi-looking imager.

82

Figure 4.14 shows the whole assembly process. The 3D imager prism is wire bonded to a printed circuit board to prepare for testing. Hexagonal imager prisms with a cross-sectional width ranging from 1 to 4 mm and a prism length ranging from 2 to 4 mm were prototyped. The size of the imager array was approximately 10 times the wavelength of the ultrasound transmitted from the transducer. Further miniaturization of the imager prism is possible with transducers of higher frequencies.
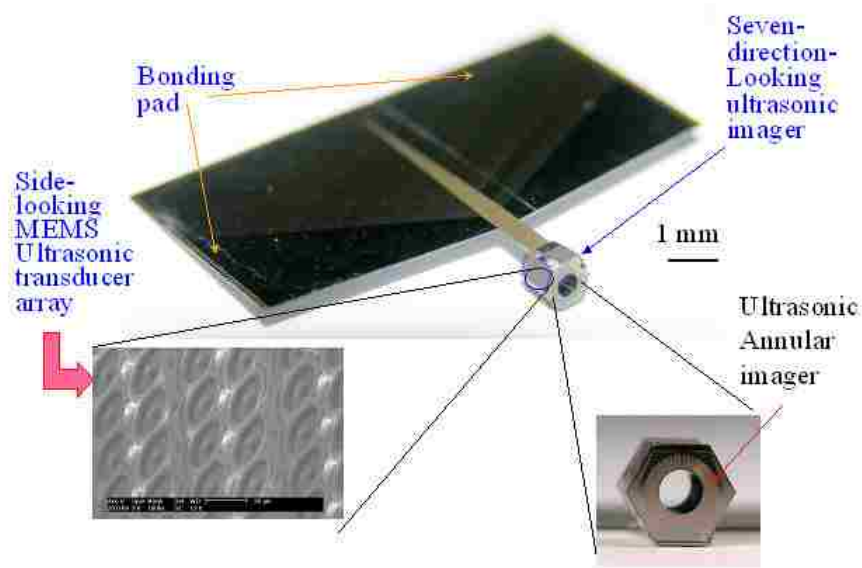
Figure 4.15 Assembled monolithically integrated seven-direction-looking ultrasonic imager.

4.5 Image –Guided Therapy

4.5.1 Introduction

Recent research has shown that High Intensity Focused Ultrasound (HIFU) [77], or Focused Ultrasound (FUS), can be used to rapidly kill tissue (directly applicable to cancer treatment) and to stop internal bleeding by cauterizing injured organs or blood vessels. The future goal of therapeutic ultrasound for surgery can be enabled through the

marriage of high performance ultrasound imaging and high intensity focused ultrasound technology. This approach is called Image-Guided Therapy (IGT) [31,104].

In this section, a high-intensity CMUT design will be analyzed. The difference of the fabrication steps between the high-intensity element and the image element along with their "marriage" will be addressed respectively.

There are two important figures of merit for high-intensity CMUT design. One is the displacement per cycle and another is displacement per volt. Displacement per cycle is defined as the difference between the average displacements of just-collapsed and just-snapped-back membranes. The collapse voltage and snapped-back voltage calculation refer to equations (2-14) and (2-15). Displacement per volt of the CMUT was calculated as the ratio of the displacement per cycle to the difference between collapse and snapback voltages. According to literature [77], both figure of merit should be as large as possible in order to have a higher output pressure.
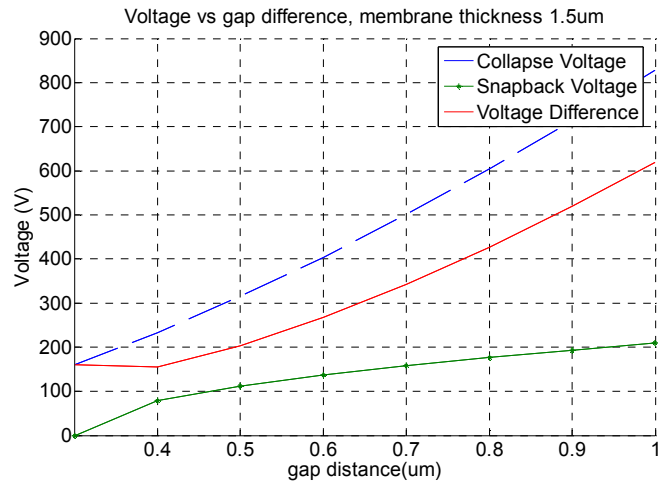
a)
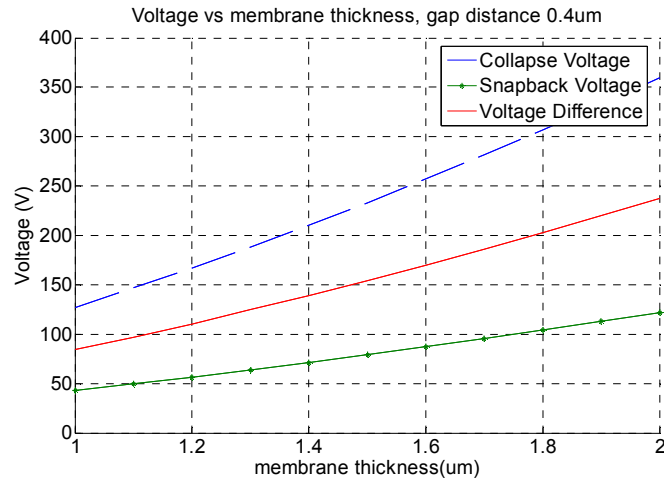
b)

Figure 4.16 a) Voltage vs gap distance (the membrane thickness is 1.5 μm); b) Voltage vs membrane thickness (gap distance is 0.4 μm)

Achieving a higher displacement per cycle requires a larger difference between collapse voltage and snap-back voltage. It is essential to calculate the difference between the snapback voltage and the collapse voltage according to different membrane parameters. As shown in Figure 4.16, by increasing both the membrane thickness and the gap distance, both the collapse voltage and snapback voltage will be increased. Obviously, the larger gap distance will have larger value of the voltage difference. However, the collapse voltage is limited by the maximum allowed voltage that could be applied to the device, especially for those in the biomedical applications.

Another important metric for a high intensity CMUT is the dynamic response time constant. The lumped dynamic model of this device can be described a using first-order spring damping mechanical system and its analogy in the electrical domain: the RC model. When the membrane works in a fluid medium, the lumped equivalent resistance can be approximated as [40]:

$$R_{eq} = Z_a \frac{(\varepsilon_0 t_m + \varepsilon_i t_i)^4}{V_{DC}^2 \varepsilon_0^2 \varepsilon_i^4 \pi a^2}$$ (4-6)

If we approximate the capacitance as $C_0 = \dfrac{\varepsilon_0 \varepsilon_i \pi a^2}{t_g + \dfrac{\varepsilon_0}{\varepsilon_i} t_i}$ (4-7)

The time constant:

$$\tau = R_{eq} C_0 = Z_a \frac{(\varepsilon_0 t_m + \varepsilon t_i)^4}{V_{DC}^2 \varepsilon_0 \varepsilon^3 (t_g + \dfrac{\varepsilon_0}{\varepsilon_i} t_i)}$$ (4-8)

In order to have smaller time constant τ, so that the membrane can have a fast response to the input pulse, we need to reduce the membrane thickness t_m and increase the gap distance t_g.

In summary, increasing the membrane thickness and gap distance will result in a large voltage difference between the collapse voltage and snapback voltage. This will consequently allow large pulse voltage as the input and therefore, will increase the value of displacement per cycle. On the other hand, in order to have faster response to the input pulse, the membrane thickness needs to be reduced. In addition, layout/fabrication issues need to be considered when designing the CMUT geometry. The membranes might have the same thickness for both imaging and high-power for the sake of simplicity of the fabrication. In this research, several combinations of the CMUT geometric parameters (membrane thickness, dimensions, gap distance) were used.

4.5.2 CMUT Annular Ring

Annular ring transducer array are commonly used for focused transducer. The geometry of high intensity CMUT membrane ring is shown in Figure 4.17. To some

extent, the membrane ring can be regarded as a curved long rectangular-shaped membrane, whose natural frequency mainly depends on dimension of the width. Therefore, the natural frequencies are mainly determined by the cross-section but not altered by the location of the ring.
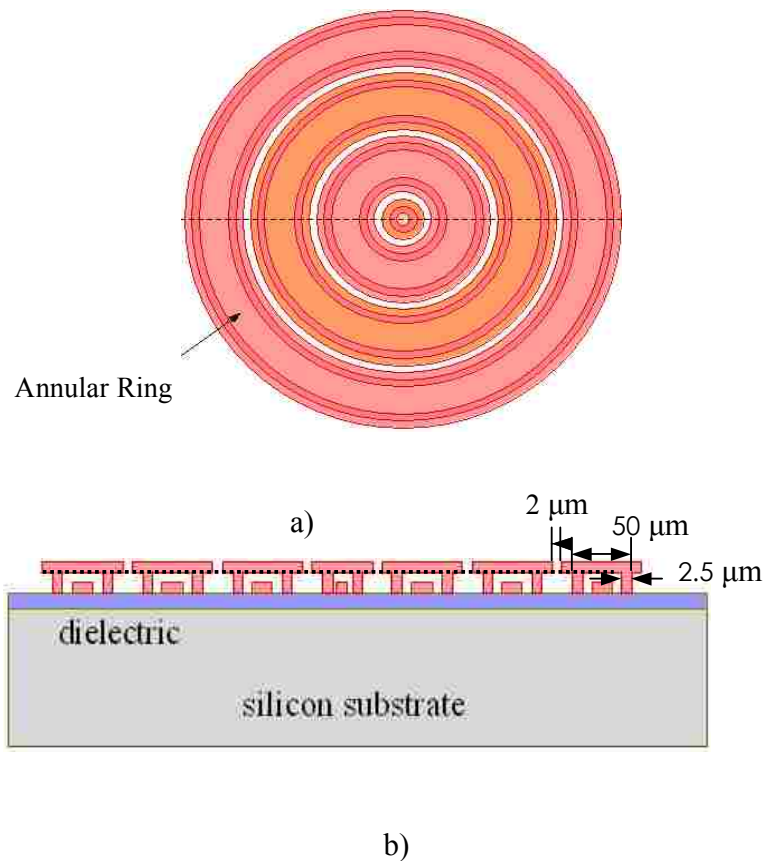
Figure 4.17 The Schematic of CMUT elements Ring for high-intensity application

Results from Finite Element Analysis are shown in Figure 4.18. The results of different combination of membrane parameters (the width of the ring, the gap distance) in Figure 4.19 provide guidelines for the selection of geometry of the ring.

87
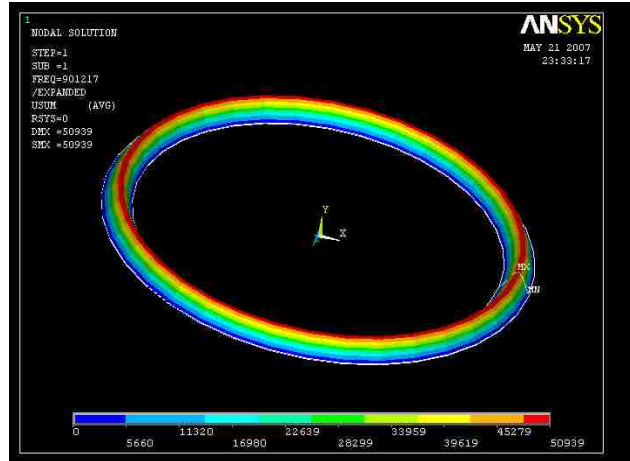
a)
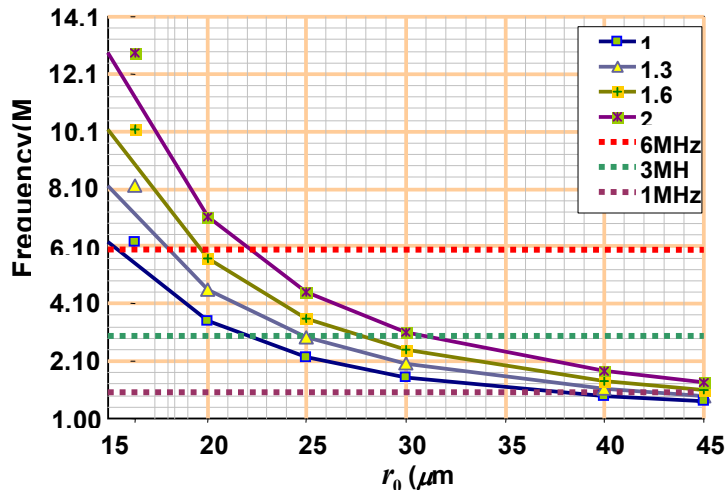
b)

Figure 4.18 a) the FEM of the High-intensity CMUT ring, b) the frequency vs ring width

4.5.3 The CMUT Annular Ring Fabrication

The fabrication of high intensity CMUT element combined with imaging element is more difficult compared to the fabrication process described in Chapter III and Sections 4.3 and 4.4. To have different gap distance for high-intensity elements and imaging elements, an extra Mask (#2A) was used to pattern the sacrificial PSG and then etch it back before the steps of lithography #2 (Anchor). This etching process was time

controlled to obtain a relatively precise gap distance for the imaging elements. The poly1 layer was then deposited and patterned as usual, and another thin LPCVD nitride (1000Å) and poly layer (3000 Å) were deposited respectively. These two layers were used to increase the thickness of the membrane. They were patterned using the same mask (#2A) for sacrificial layer etch-back. The rest of the fabrication steps were the same as the one for multi-directional imager. The fabricated high intensity CMUT with imager elements is shown in Figure 4.19.

Image elements

Ring elements

a)

b)
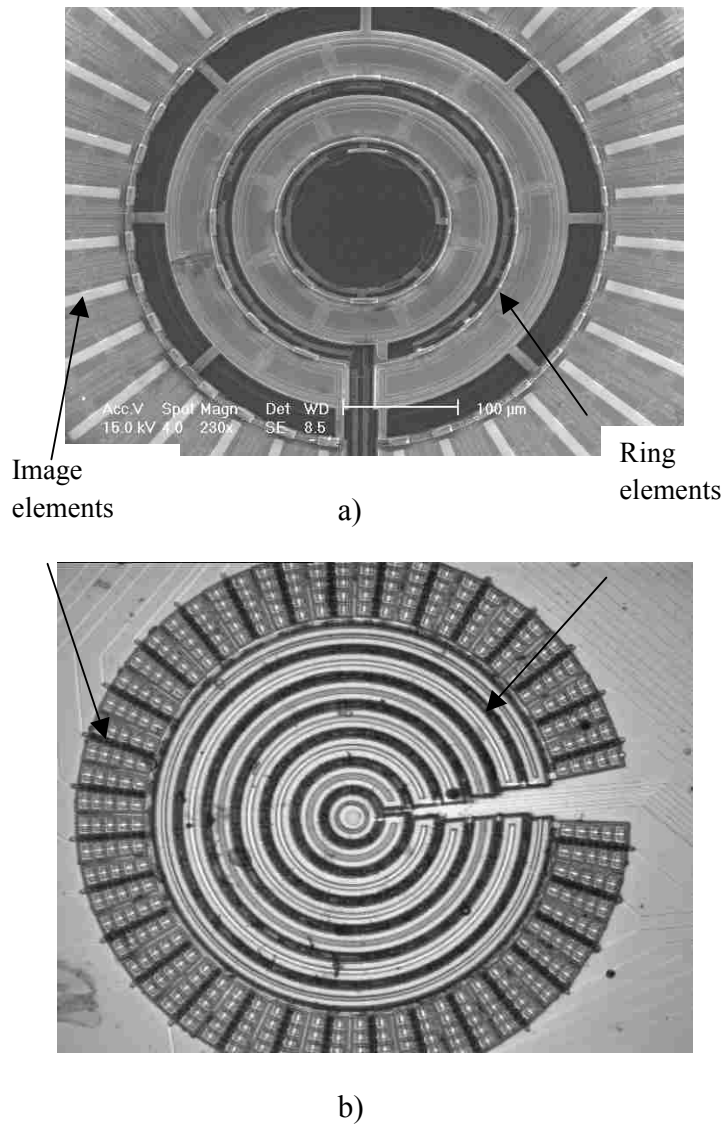
Figure 4.19 Photos of the High-intensity CMUT a) 2 ring elements b) 12 ring elements

4.6 Summary

In this chapter, the basic principles of CMUT arrays were introduced at first. This provided us a design guideline for the CMUT transducer array arrangement. The specific requirement for the biomedical application such as the biocompatible material encapsulation was discussed. Three prototypes for different applications were described: The invasive blood flow metering, the minimally invasive multi-imager, and the image-guided therapy array were fabricated.

CHAPTER V

CHARACTERIZATION OF CMUT ARRAYS

The characterization of CMUT devices is important to validate the theoretical models, and to provide parameters for interface circuit design. The characterization steps in this research include frequency performance evaluation for transmit and receive mode as well as angular response measurement.

This chapter describes the methods used for experimental characterization of a CMUT array element in receive and transmit modes. The results are compared to theoretical predictions. The experimental results presented in this chapter primarily aim to confirm the viability of the CMUT in applications, rather than to demonstrate an optimized system. This chapter is organized as follows. The first two sections present the experimental setup and results for the CMUT operating as receiver and transmitter respectively. The characterization results regarding the angular response of the CMUT array element is presented in section 5.4. In section 5.5, issues such as CMUT-Fluid interaction, sensitivity, and noise will be analysed. Finally, the charge trapping effect on CMUT performance will also be discussed.
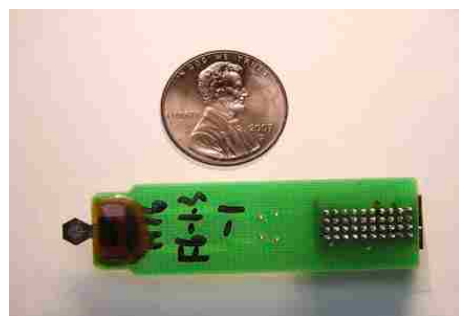
a)   b)

Figure 5.1 the wire-bonded device on PCB

The device under test was wire-bonded to a custom-designed PC board (see Figure 5.1 a and b) and encapsulated after a primary electronic probe test. The detailed procedure can be found in Appendix B. Since all the tests are conducted in fluidic medium (oil or water), the bonding pads need to be encapsulated with insulating epoxy to prevent any electrical leakage. The PCB with a male connector (40pins, 0.05" pitch) provided a bridge (interconnection) between each element of the array and the readout/excitation circuit. This allows up to 39 elements (one pin for GND) of the array to be connected to the readout circuit. Table 5.1 lists the parameters of the devices used for the following measurements.

CELL DIAMETER (OR LENGTH) (μM)	46 / 80 (CIRCULAR)
	45X45 (SQUARE)
Element Pitch (μm)	150 /200
Number of Cells per element	150
Membrane Thickness (μm)	1.0 /1.5
Insulating layer thickness (μm)	0.3
Silicon Substrate Thickness (μm)	100
Gap Distance (μm)	0.2

Table5.1 CMUT Parameters for characterization

5.1 Characterization of CMUT as Transmitter

Transmit mode characterization focuses on the pressure amplitude of the signal that is generated by the membrane. The experimental setup shown in Figure 5.2 was used to characterize the CMUT in transmit mode. The CMUT transducer array was immersed in a tank filled with water (or vegetable oil) and was driven by narrow-band pulses generated by a pulse generator (PANAMETRICS 5072PR). A focused transducer was

used to receive the ultrasounds signals transmitted from the CMUT. For comparison, both of the devices with and without a boss on the membrane were used for the measurement.
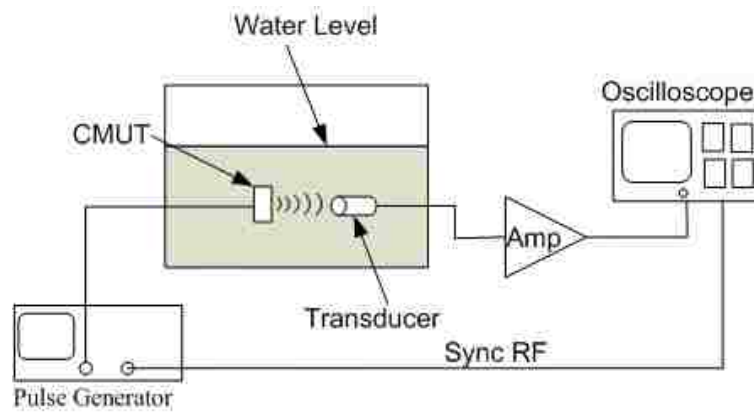
Figure 5.2 the block diagram of the experimental setup for CMUT transmitting mode;

The square shaped CMUT (45μm by 45μm, membrane thickness 1.5μm) and circular shaped CMUT were used in this measurement. Their layout is shown in Figure 5.3.

a)   b)
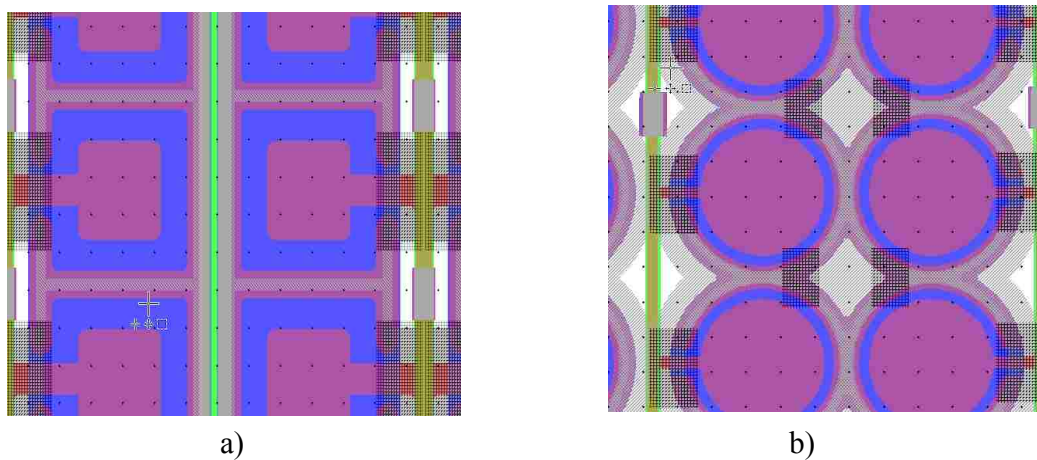
Figure 5.3 Layout of different shapes of cells   a) square, b) circular

The signals transmitted by the CMUT transducer and received by the commercial focused transducer are shown in Figure 5.4. Their frequency spectra are shown in b) and d) respectively. The frequency response was digitally filtered to remove the out-of-band noise. The –6dB fractional bandwidth line was drawn in the figure. For circular shaped

CMUT, the center frequency is about 5MHz with 70% fractional bandwidth; for square shaped CMUT, the center frequency is 4.5MHz with 100% fractional bandwidth.
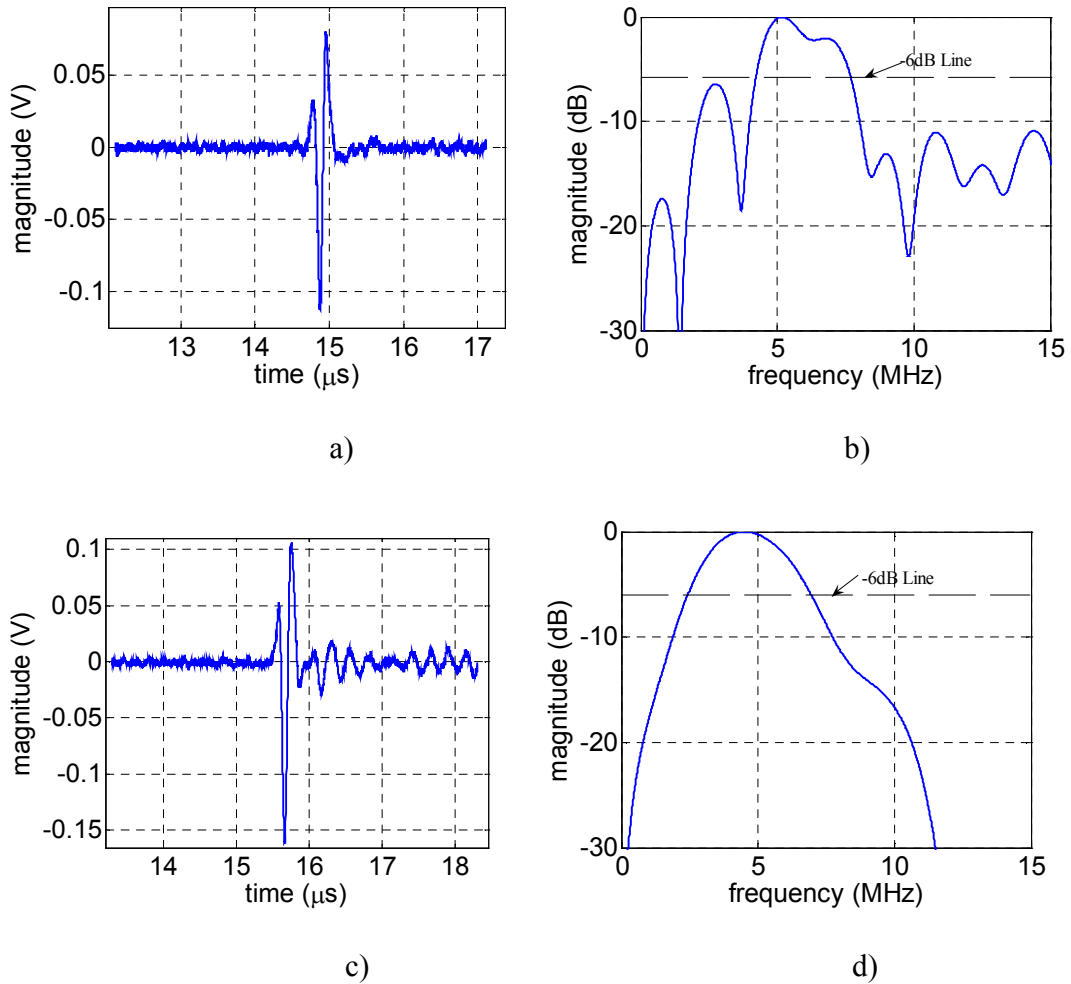
Figure 5.4 a) the ultrasound signal transmitted by a circular transducer and received signal by a piezoelectric transducer in water. b) Frequency spectrum of a); c) the ultrasound signal transmitted by a square transducer and received by a piezoelectric transducer. d) Frequency spectrum of c).

It seems that the square CMUT has a higher fractional bandwidth than the circular one. The detailed explanation of this phenomenon is not yet clear. It could possibly be interpreted that the square shaped membrane has larger fill factor value than the circular membrane. The fill-factor is defined as the ratio of the total membrane area to the

element area. This determines the effective radius (length) of the element, and the radiation impedance of the medium surrounding the CMUT. According to [107], the fractional bandwidth increases when the fill-factor increases.

For comparison, the experiments were conducted for CMUT with and without boss on the membrane respectively. The CMUT devices were immersed in water. Fig. 5.5 shows the frequency response of ultrasound signals transmitted from the CMUT (46 μm in diameter, 1.5 μm in thickness) when they were triggered by a 5V peak-to-peak, 200ns wide electrical impulse under 20V DC bias. Fig. 5.5 (a) and (c) are spectra of ultrasound signals transmitted from a planar 46mm-diameter CMUT (46P) device in water and vegetable oil, respectively, while Fig. 5.5 (b) and (d) are spectra of ultrasound signals transmitted from a bossed 46 μm -diameter CMUT device (46B) in water and vegetable oil, respectively. The diameter of the oxide boss on the 46 μm-diameter membrane is 15 μm, which covers 11% of the membrane area. Due to a slightly better acoustic impedance match between the transducer and vegetable oil vs the transducer and water, the ultrasound power output in vegetable oil is higher than in water for the same device under the same electrical excitation. The height of the oxide boss is about 3μm. The corresponding measurement on high and low cut-off frequencies, as well as fractional bandwidths of spectra are listed in Table 5.2. The fractional bandwidth of the membrane increased from 15% to 92% in water, and from 26% to 62% in vegetable oil with addition of the 15μm-diameter oxide boss. The increase of fractional bandwidths from bossed CMUT devices is mainly due to the increase of the high cutoff frequencies ($f_{+, 6dB}$). The low cutoff frequencies ($f_{-, 6dB}$) are almost the same for the devices with and without boss.

For example, the low cutoff frequencies of devices 46P and 46B are 2.4 and 2.5MHz, respectively, while their high cutoff frequencies are 3.1 and 4.75MHz, respectively.
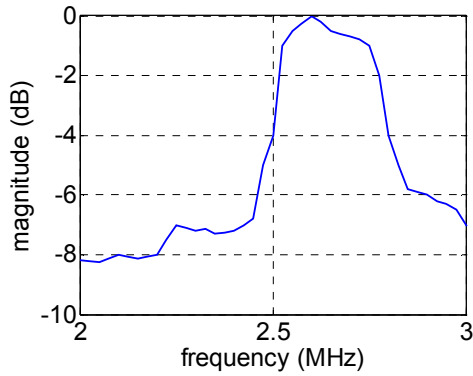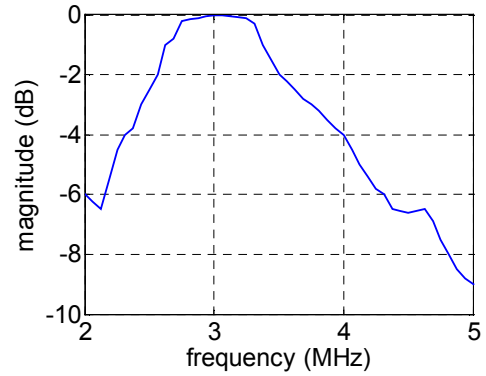
(a)   (b)
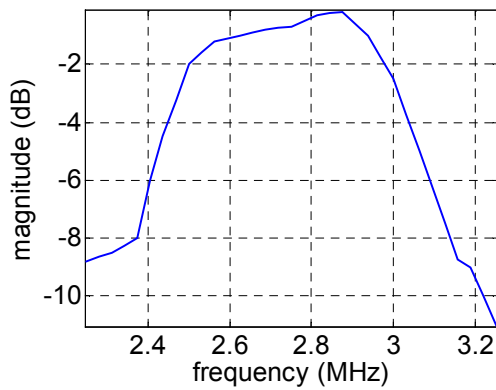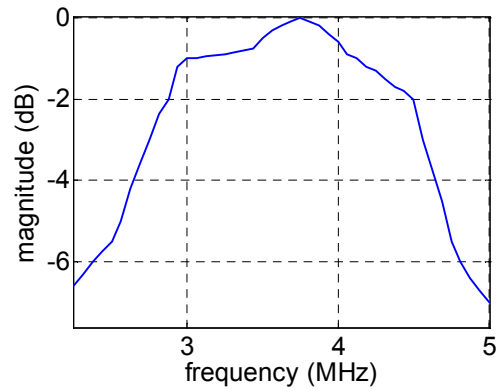
(c)   (d)

Figure 5.5 Spectra of the ultrasounds transmitted from a 46μm-diameter CMUT device (a) without boss, in water; (b) with a 15μm-diameter boss, in water; (c) without boss, in vegetable oil; (d) with a 15μm-diameter boss, in vegetable oil. The transducer was triggered by a 5V peak-to-peak, 200ns wide electrical impulse under 20V DC bias.

	LOW CUTOFF FREQUENCY (MHZ)	HIGH CUTOFF FREQUENCY (MHZ)	BANDWIDTH (MHZ)	FRACTIONAL BANDWIDTH
46P in water	2.45	2.85	0.4	15%
46B in water	2.25	4.2	2.95	92%
46P in vegetable oil	2.4	3.1	0.7	26%
46B in vegetable oil	2.5	4.75	2.25	62%

Table 5.2 Low cutoff frequency, high cutoff frequency, and bandwidth of devices 46P, 46B, in water and vegetable oil.

5.2 Characterization of CMUT as Receiver

Working as a receiver, dc bias on a CMUT is required to supply electrical charge to the electrodes. The setup is shown in Figure 5.6 a). The CMUT is charged using resistor R. As described in chapter II, the condition $R \gg 1/C_c$ must be fulfilled to avoid a current flow over the voltage source for the bias voltage. A decoupling capacitor C_c is commonly used to connect the CMUT to amplifier circuits, ideally in parallel to the device capacitance C_w of the CMUT itself. If an ideal operational amplifier is assumed, only the current flowing to the virtual ground point of the amplifier is responsible for the output voltage of the operational amplifier. The time constant τ increases from $\tau = RC_w$ to $\tau = R(C_w + C_c)$.

If the resistor R is large enough, the overall charge Q stored on the CMUT electrode is approximately constant with respect to the signal frequency. This means that the change Δc (t) in the capacitance value of the CMUT is detected by measuring the output current under an initially constant charge Q on the CMUT electrodes. In Figure 5.6a), it can be seen that voltages across the CMUT and the decoupling capacitor C_c are

approximately equal. (R_{in} is through transmission input resistance with a very small value). Given the assumption that the change $\Delta c(t)$ in the capacitance value of the CMUT is small in comparison to the device capacitance C_w, the output current from the decoupling capacitor is expressed as below:

$$i = C_c \frac{d}{dt}\left(\frac{Q}{C_w + \Delta c(t) + C_c}\right) = -\frac{C_c Q \frac{d\Delta c(t)}{dt}}{(C_w + \Delta c(t) + C_c)^2} \qquad (5\text{-}1)$$

Where $Q = V_{bias}(C_w + C_c)$ is the total charge stored at the CMUT electrodes and in the decoupling capacitor. Therefore, the decoupling capacitor must be dimensioned large with respect to the device capacitance C_w of the transducer at the cost of a large time constant with respect to the bias voltage.

a)
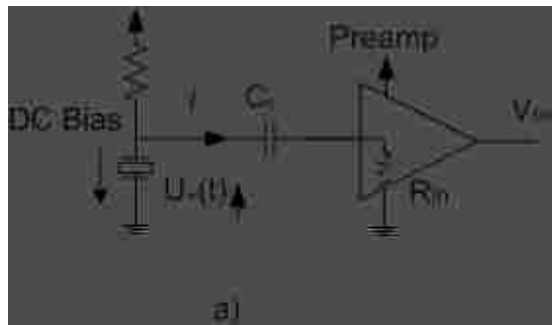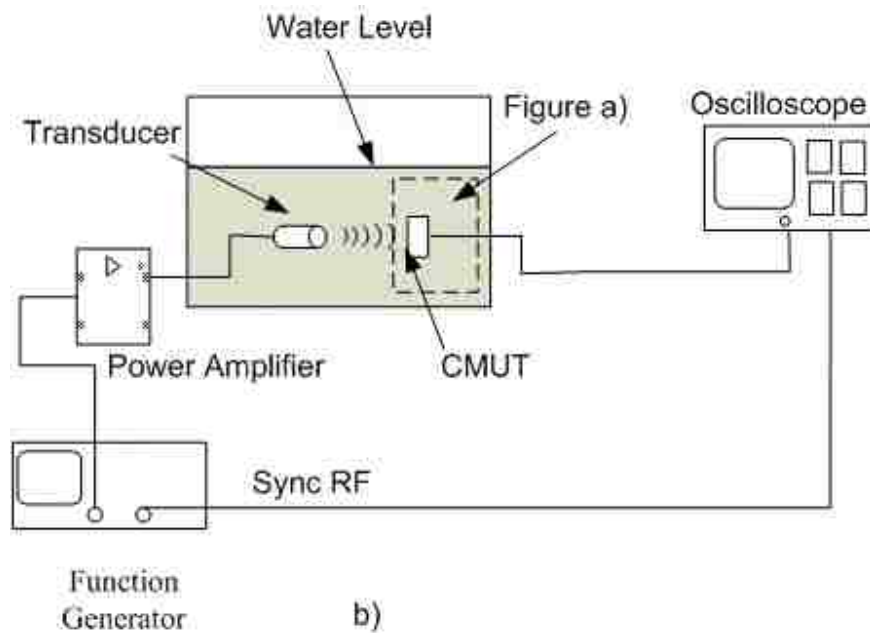
Figure 5.6 the experimental set-up for CMUT receiver measurement

Figure 5.6 b) shows the schematic of the receiver characterization experimental setup. The experiment was conducted in a water tank with the MEMS ultrasonic transducer working as a receiver to receive ultrasound signals transmitted from a commercial piezoelectric ultrasound transducer. A function generator (Agilent 33120A, Palo Alto, CA) generates electrical pulses for exciting a piezoelectric ultrasonic transducer. The CMUT was biased and then connected to the embedded pre-amplifier of the pulse generator (PANAMETRICS 5072PR) before being connected to the oscilloscope. The pre-amp has large input impedance and low output impedance 50Ω, functioning as a buffer as well. Figure 5.7 is the picture of the ad hoc DC bias setup.
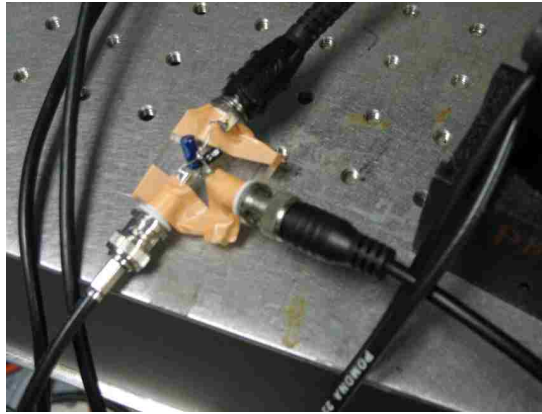
Figure 5.7 the bias setup in the test

The received signal, after 30dB amplification, in time domain and its frequency spectrum is shown in Figure 5.8. The central frequency of the receiver spectrum was about 5.0MHz, and the −6 dB fractional bandwidth is 116%.
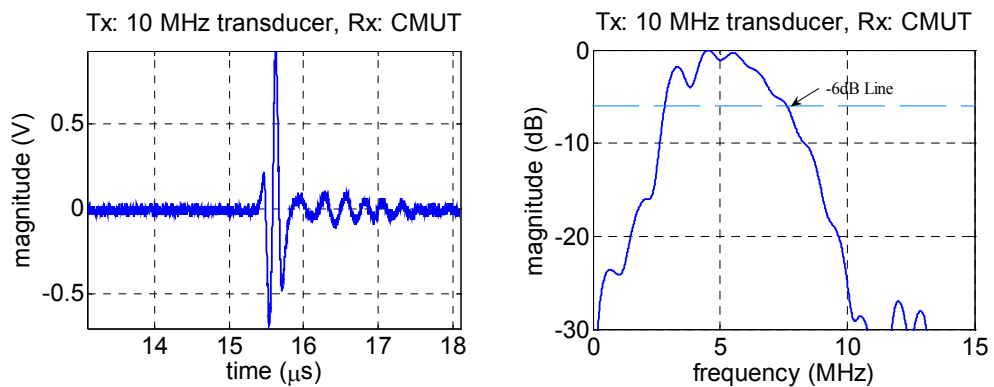
Figure 5.8 a) Received Signal; b) spectrum of a)

5.3 Pulse-Echo Testing

The setup for pulse-echo measurement is as shown in the Figure 5.9. The pulse was generated from the pulse generator (Olympus 5077PR), with a pulse width about 50ns and amplitude of 100 volts.
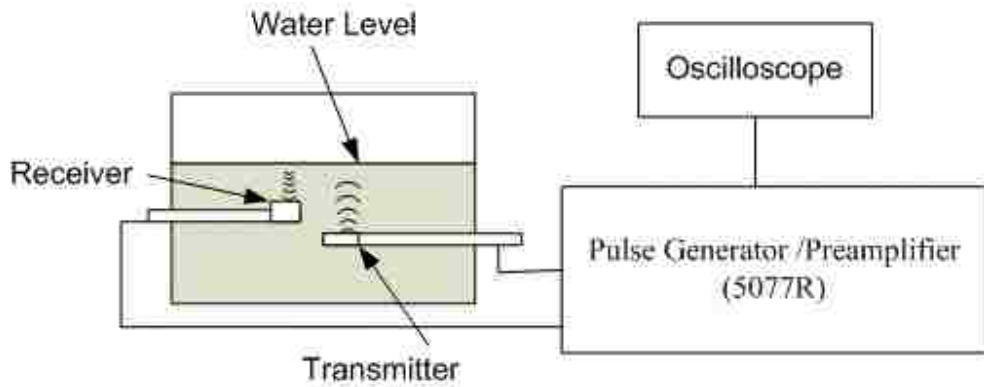
Figure 5.9 the schematic of Pulse-echo setup
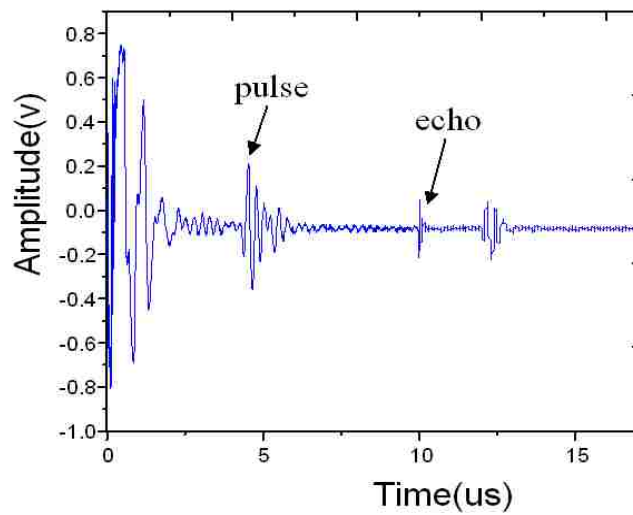
Figure 5.10 the Pulse-echo Impulse response

The echo signals reflected by the water level can be seen in Figure 5.10. The corresponding frequency response is shown in Figure 5.11. This frequency response is centered at 5.8MHz with 60% fractional bandwidth.
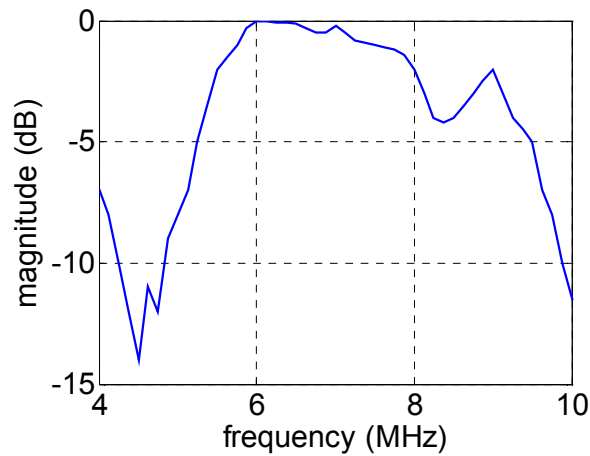
Figure 5.11 the pulse-echo Frequency Response in frequency domain

5.4 Measurement of Angular Response (Radiation Pattern)

The term radiation pattern comes from the field of antenna design, which refers to the directional (angular) dependence of radiation from an antenna or other source. Ultrasonic transducers are also characterized with respect to their radiation patterns [15-16]. The basic physical structure of an immersion CMUT is a solid silicon plate with fluid on both sides. The boundary conditions associated with CMUT provide the environment for the excitation and propagation of various spurious modes such as Lamb waves and Stoneley waves that cause cross talk [78-79]. The angular response of the radiation pattern of a transducer array element is an important design parameter for the imaging system. For a high quality imaging system, a broad radiation pattern is desired. Cross talk between the array elements can also be identified from the radiation pattern. However, to get a highly accurate measurement of angular response of an array element is very challenging due to many precise mechanical alignments required for the process. We fixed the axial direction of the CMUT horizontal in the tank. The hydrophone was mounted on stage

capable of rotating and linear translation. The alignment was achieved by moving the hydrophone to get the maximum amplitude of the received signal. A basic experiment conducted to measure the radiation pattern is shown in Figure 5.12.

a)
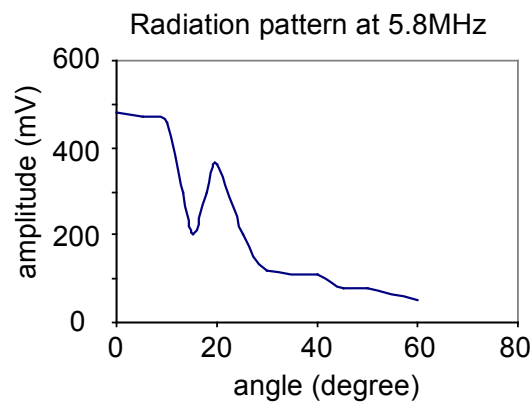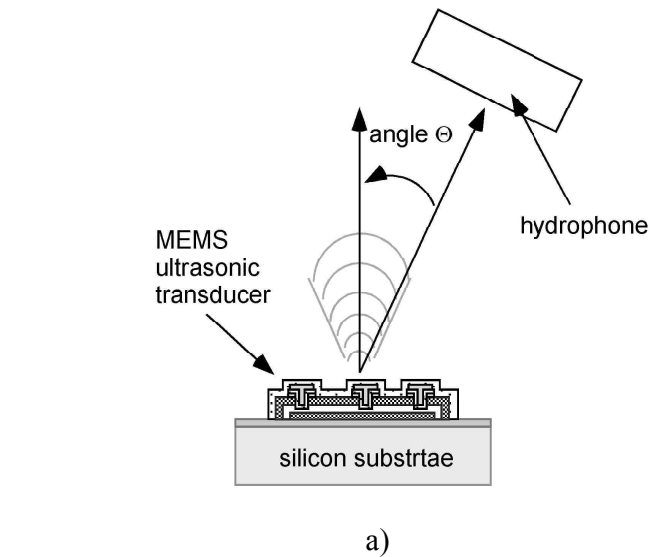
Figure 5.12 (a) Experiment setup   b) Radiation pattern plot

The radiation pattern measurement result of a 46um-diameter device in water is shown in Figure 5.12 b). It is often considered that the radiation pattern's dip in amplitude near 15 ° is due to Lamb wave crosstalk. An effective approach to reduce this crosstalk is to reduce the thickness of substrate.

5.5 Discussion

5.5.1 CMUT–Fluids Interaction

Knowing the bandwidth change due to the addition of a membrane boss provides us preliminary information about the acoustic interaction between the media and CMUT devices. To further characterize the acoustic field transmitted by a CMUT device in a specific media, we employed finite element analysis. Using the 46μm membrane in water as an example, an axisymmetric membrane similar to Fig. 2.11 was created inside water. Considering the numerical accuracy and efficiency, the computational domain is taken to be 50 times larger than the width of membrane. We discretized the domain by 4-node elements PLANE42 for the membrane and FLUID29 for the fluid. The analysis was carried out by a harmonic analysis in which a sinusoidal, arbitrary uniform force (0.5μN, in this analysis) was imposed on the bottom of membrane. Pressure distribution inside the fluid can be calculated accordingly. We analyzed the pressure over frequencies from 1MHz to 10MHz. The results were then compared to the experiments in Fig 5.5(a) and (b). As shown by the dashed line simulation results in Fig 5.13, one effect of the boss on acoustic transmission is to shift up the peak values of pressure (resonance) and make it relatively pronounced. Therefore the estimates on the peak dB values were found around 2.50MHz for the planar membrane and 3.15MHz for the bossed one from FEA, while 2.55MHz and 3.20MHz, respectively from the experiment.
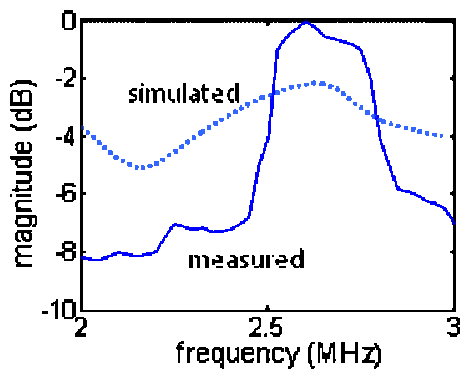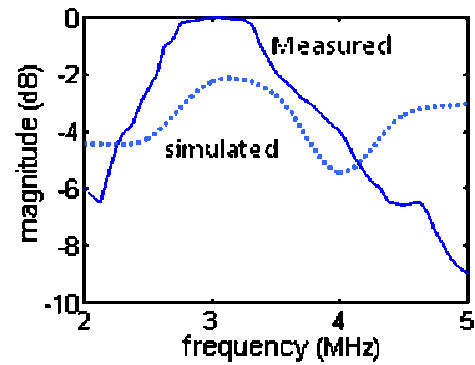
(a)   (b)
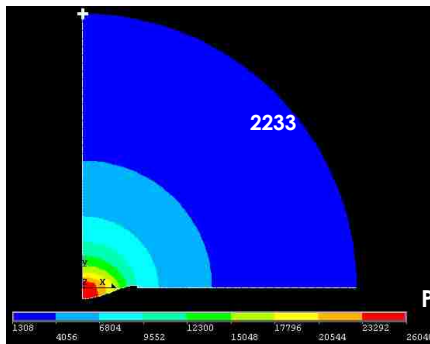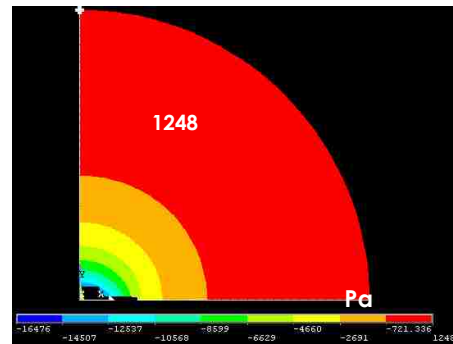
(c)   (d)

Figure 5.13 FEA for the spectrum of ultrasounds transmitted by a 46 μm -diameter (a) without boss in water; (b) with a 15μm-diameter boss in water. (c) and (d) are the corresponding pressure contours under the vibration of membrane at frequency 2.5 and 3.0MHz by a uniform .force 0.5μN.

The dashed lines in Figure 5.13 (a) and (b) are the results from FEA at the location of 11.5×10^{-1}mm, 90° above the center of membrane (marked by + on the pressure contours in (c) and (d)).

5.5.2 Open-circuit sensitivity

One important performance metric for CMUT receiver is the receiving sensitivity [5] that is the measure of how much voltage a transducer generates when terminated by an

open circuit at the electrical port for a unit pressure input [5]. Taken into account the equivalent circuit of the amplifier, the figure 5.5a) could be redrawn as in Figure 5.14.
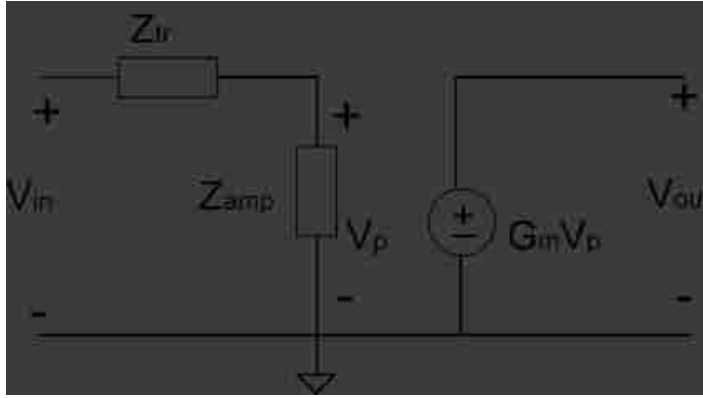
Figure 5.14 the equivalent Circuit of the readout circuit

Z_{tr} is used to represent the impedance of the transducer. Z_{amp} is the impedance seen at the input of the amplifier and considered to have a very large value. G_m is the gain of the amplifier. V_{in} is the voltage generated by the transducer while V_{out} is the voltage measured at the output (the oscilloscope). Therefore, if considering P_{in} as the input pressure to the transducer and defining the unit of *OCRS* as decibels relative to *1V/μPa*. The open circuit receive sensitivity (*OCRS*) for the *CMUT* can be calculated as

$$OCRS = \frac{V_{in}}{P_{in}} = 20\log(\frac{V_{out}}{G_m} \frac{Z_{tr} + Z_{amp}}{Z_{amp}} \frac{1\mu P_a}{1V P_{in}}) \quad\quad (5\text{-}2)$$

The commercial transducer must be characterized so that the pressure produced by it at a known location and the pressure field mapping can be used as the input for the above calculation. Using a characterized focused transducer as a transmitter and placing the CMUT at the same distance from the transmitter, we can estimate the acoustic pressure on the surface of the membrane. Strictly speaking, the detailed calibration data of the transducer pressure at different frequencies and the amplifier gain are needed for

compensation in calculation. In this experiment, the available transducer was once calibrated with its output pressure of 2.6*MPa* at 10*MHz* at its focal point, but no detailed pressure field was provided. After measuring the output of the CMUT under different dc bias voltage, we could obtain the approximate receiving sensitivity of CMUT as shown in Table 5.3.

DC BIAS (V)	5	15	20	30	40
Sensitivity (nV/Pa)	1.27	10.8	17.22	32.53	59.95
Sensitivity in dB	-297	-279	-275	-269	-264
Hydrophone sensitivity [80]	300nV/Pa (-250.5dB) at 3MHz (8dB amplifier) dimension: .5mm in diameter				

Table 5.3 the sensitivity of CMUT receiver

The CMUT element (100 cells, 46um in radius) under test has effective area of 0.24mm^2. As the dc voltage increases, the output sensitivity is increased. This value however is not very precise due to the transmitter frequency bandwidth mismatching with the CMUT frequency response. The sensitivity of the commercial hydrophone with approximately the same area was listed here for comparison. According to [80], the commercial hydrophone (size: 5mm in diameter) sensitivity is 300nV/Pa at 3MHz when measured at the output with submersible preamplifier (8dB gain). The real sensitivity is 120nV/Pa, corresponding to -258.5dB. It is about 6dB higher than our CMUT. If increasing the dc bias higher than 40V, it is possible to achieve higher sensitivity than the commercial hydrophone.

5.5.3 Noise analysis

The above sensitivity analysis includes no consideration of the random noise, which is an integral part of the system. The noise sources include the CMUT mechanical noise, and the electrical noise from the related circuit.

a) The inherent Noise

A well-known mechanism for mechanical/thermal noise is Brownian motion. For capacitive sensors, such as condenser microphone, the mechanical noise is mainly due to squeeze film damping. For a sealed CMUT, the squeeze-film damping and resulting noise can be ignored due to the high level of vacuum inside the sealed chamber. But there is another damping effect when the CMUT works in the liquid medium. It is related to the radiation resistance [48]. Nyquist's Relation gives the spectral density of the fluctuating force (mechanical noise) related to any mechanical resistance [81]

$$F = \sqrt{4k_B TR} \quad (N/\sqrt{Hz}) \qquad (5\text{-}3)$$

or the fluctuation pressure related to any acoustic resistance

$$p = \sqrt{4k_B TR_{acs}} \quad (Pa/\sqrt{Hz}) \qquad (5\text{-}4)$$

where $k_B = 1.38 X 10^{-23} J/K$ is the Boltzmann constant. Radiation resistance can be significant dissipation mechanism above 10 KHz. The simplified form of mechanical radiation resistance is approximated closely (for ka<1) by [48]

$$R_r = \rho c \pi a^2 (ka)^2 /4 \quad N.s/m \qquad (5\text{-}5)$$

where k is the acoustic wave number (ω/λ), ρ and c are the density and sound speed of the fluid, and a is the effective radius of the element.

Another important factor, flicker noise or *1/f* noise, exists in a wide variety of physical phenomena which are often related in the fact that the noise power is proportional to approximately *1/f*. the origin of *1/f* noise is not well understood, so it is hard to discount its importance on theoretical grounds. However, it can be shown experimentally that *1/f* noise is not significant for ultrasonic transducers operating in the MHz range by measuring the noise level as a function of frequency and noting that the characteristic *1/f* frequency dependence does not extend into the MHz range.

The electrical noise existing in the circuit includes the thermal noise of the bias resistance, and the parasitic resistance along the interconnection. However, the RMS value of noise $\sqrt{KT/C}$ was estimated small thanks to the large coupling capacitance ($4.7\,\mu F$). The RMS value is estimated to be $0.3\,\mu V$. Therefore, the peak value of noise contributed by bias circuit is approximately $\pm 1\mu V$, which is negligible. There are also noises coming from the instruments such as the amplifier and the oscilloscope etc. The total noise of the whole system can be evaluated using equivalent noise pressure.

b) The equivalent Noise Pressure

The equivalent noise pressure measurement was conducted by zeroing the input pressure, that is, the CMUT will not provide any acoustic signal but noise to the oscilloscope. The entire signal obtained by oscilloscope is regarded as noise contributed by the peripheral circuit and CMUT. The measured RMS noise signal is $1.52 \times 10^{-4} V$ in the frequency range from 0 to 15MHz. Therefore, the minimum detectable voltage was around $39.2 nV/\sqrt{Hz}$. The equivalent noise pressure is about *1.18KPa*.

5.6 Charge effect analysis

Electrical and acoustic testing was performed to identify charging problem associated with the dielectric layer between the CMUT electrodes. A CMUT device with a dielectric layer was biased at 40V. for two hours. The DC bias was then removed in a subsequent receive-mode experiment using this device as the receiver. It was found that even without a DC bias, this device was able to receive ultrasound signal from the transmitter. Fig. 5.15 shows the signal received by this device without a DC bias has the opposite polarity of the signal with the DC bias. This indicates that the trapped electric charges in the dielectric layers moved along the electric field and accumulate at the surface (see section 2.4). The surface conduction results in the self-biasing when the external biasing voltage was removed. However, at the zero bias status, the diffusion process takes place. Due to the large size of the trapped charges (ions) in comparison to the silicon oxide/nitride atoms in the dielectric layer, the movement (diffusion process) through the dielectrics has a large time constant in comparison to other kinds of polarizations. If it is assumed that there is no lateral component of the electrical field in the oxide layer, after a few minutes (5 ~10 mins) the charges again are evenly distributed in the oxide layer, and therefore the polarization of the transducer is lost.

For the purpose of comparison, another CMUT device of the same diameter and membrane thickness but with nine 2μm×2μm nitride posts on the polysilicon counter electrode was used in a similar electrical acoustic experiment. The posts significantly reduce the contact area between the polysilicon counter electrode and the nitride film. The device was biased with 40V DC. In the receiving experiment, the device was used as the receiver without a d.c. bias to receive ultrasound. It was observed that only after about

four hours of prior d.c. bias can this device start to receive ultrasonic signal without a d.c. bias. It was therefore concluded that the smaller the direct contact area between the nitride film and the conductor polysilicon, the lesser the charging problem. Additionally, although the dielectric post reduced the charge-trapping problem, there still exist other charge-trapping sources in this device.
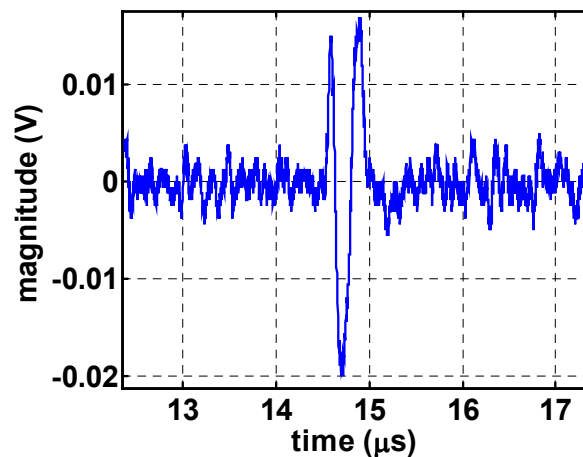
Fig 5.15 Received signal of CMUT without DC bias.

5.7 Summary

A thorough investigation on the device performance was conducted in this section. The characterization was discussed in first two sections. Results have shown that the CMUT are capable of working both as transmitters and receivers. Some issues such as CMUT-fluid interaction, the sensitivity/noise were also analyzed. Finally, the charge trapping issues were also considered through the experiment.

CHAPTER VI

ULTRASONIC IMAGING

Demonstration of image acquistion is critical to producing a better evaluation of the potential of CMUT for medical applications. In this chapter, efforts to demonstrate ultrasonic imaging using a 1D CMUT array are described. The photoacoustic images for lobster nerve cord are presented.

6.1 Experimental Setup

Demonstration of imaging is critical to making a better assessment of CMUT's potential for ultrasound imaging. In this study, a 1-D CMUT array was used. Figure 6.1 a) shows our experimental setup used for imaging with one of the CMUT array on the 3D prism as the receiving transducer. Similar to the receiving test, the pulse generator connected to a commercial transducer was used to transmit a negative acoustic signal. A copper wire phantom with a diameter of 0.5mm was placed in the focal zone of the transmitting transducer (V312, Panametrics Inc., Waltham, MA) and the CMUT device was placed perpendicularly to the transmitting transducer and facing the wire phantom.

The conventional approach is to have all array elements simultaneously receive the signals. With the aid of multi-channel multiplexer/amplifier and ADC and corresponding PC control board, the multi channel RF signals will then be filtered, digitized and processed to reconstruct the image. Constructing such a multi-channel receiving system including the hardware and software is time and cost consuming and not a major task of this project. A simple but effective alternative method was employed in this research. One element of the whole element array was selected to receive the signal during each

pulse cycle. Figure 6.2 illustrates the scheme of using single element to capture the data. The CMUT was carried by a translation stage driven by a motorized linear actuator (T-LA60, Zaber Technologies Inc., Richmond, BC, Canada) as shown in Figure 6.1 b). Therefore, the selected element i could move to locations possessed by other elements. For instance, at time i, it received the reflected signal pulse at the position i. It then moved to the next position $i+1$ before the next reflected signal pulse arrived. Consequently, at time $i+n$, this element moved to the position $i+n$, and correspondingly catches $i+nth$ signal pulse. The signal caught at each position will be saved for processing. Using this method, the signals received by one element at different time and location would be regarded as if they were received by multiple elements simultaneously. The received signals were amplified and digitized by an oscilloscope and transferred to the computer. The image reconstruction was done using MATLAB.
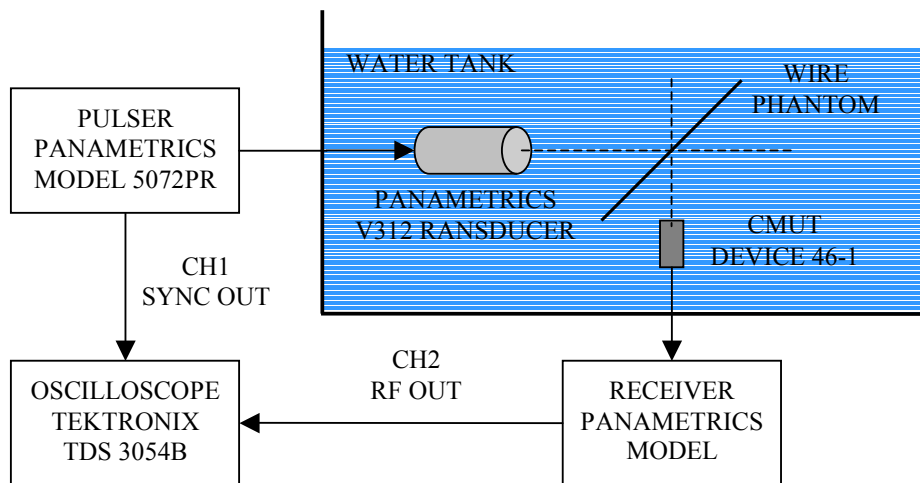
a)
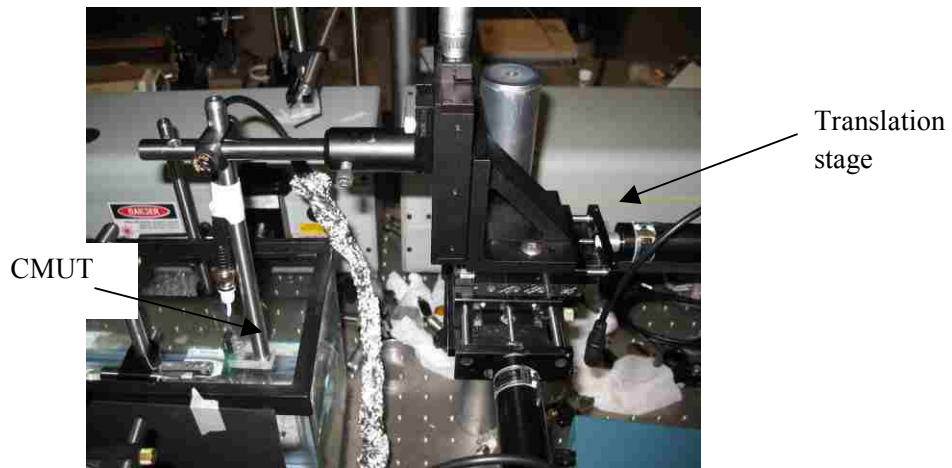
b)

Figure 6.1 Experimental setup used for CMUT device as a receiver. a) Schematic, b) The picture of setup
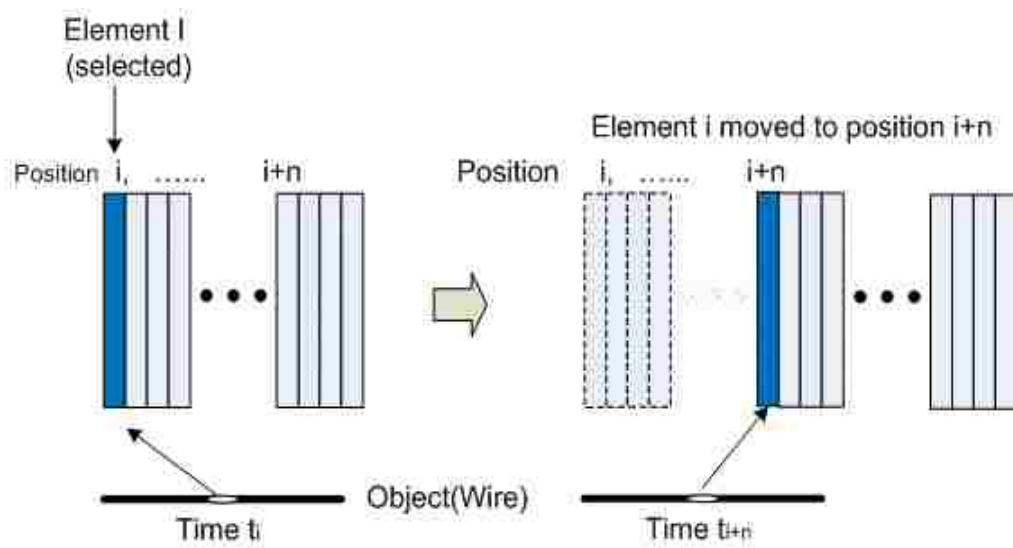
Figure 6.2 Scheme for signal receiving using signal element to form B-mode imaging.

6.2 Image Reconstruction

Prior to image reconstruction, a digital filter with 2~10MHz passband is applied to the raw data to eliminate out-of-band noise. A synthetic aperture focusing technique (SAFT) was employed for imaging reconstruction. That is, for every point in the image

plane, geometric focusing delays (i.e., the time required for sound waves to propagate from the image point to the receiving transducer) were applied. The delayed signals from all contributing array elements were then summed. The beamforming can be expressed as:

$$U(x,z) = \sum_{i=1}^{m} w_i[x,z]s_i[k]$$ (6-1)

where

$$k = round\{f_s(\frac{\sqrt{(\Delta x_i)^2 + (\Delta z_i)^2}}{c} + t_0)\}$$ (6-2)

In the expression above, $U(x,z)$ is the value of the image pixel in discrete space represented by sample indices (x,z), and $w_i(x,z)$ represents the weighting (Gaussian function) for the *ith* element position during receive operations. The round value of equation (6-2) is to pick the closest sample to the calculated exact time point. t_0 is the offset value of the time including the time for sound waves to propagate from the transmitting transducer to the imaging object. Δx_i and Δz_i are the distances from the sample point *(x, z)* to the position *(xi, zi)* of the transducer elment *i* respectively. *s* is the receive signal. f_s is the sampling frequency and c is the speed of acoustic wave. The final reconstructed B-scan image with 18mm image depth and 20mm image width is displayed with dynamic ranges of 12dB and 6dB in Figure 6.3 a) and b) respectively.
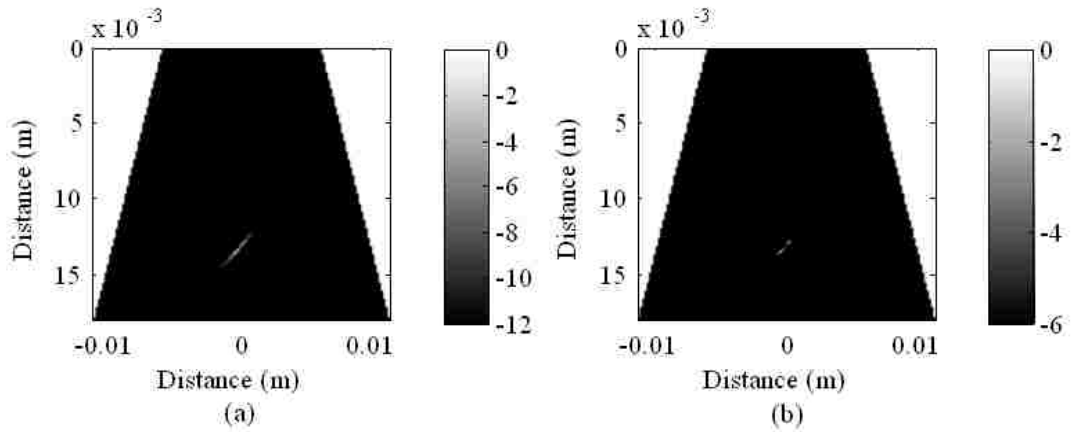
Figure 6.3: The reconstructed B-mode image of a metal wire tip with display dynamic ranges of (a) 12dB and (b) 6dB.

The lateral and axial projections of point-spread function are shown in Figure 6.4. An important observation made on PSF is that it exhibits a smooth monotonic fall-off in amplitude. It is also worth noting that the using –6dB roll-off points for the given PSF gives us the image axial and lateral resolution for the image system. The measured -6dB lateral beamwidth is 1.84mm and the measured -6dB axial pulse length is 1.81mm. From the discussion in Chapter IV, the axial resolution defines the ability of the system to distinguish neighboring targets spaced in the axial direction, while the lateral resolution defines the ability of the system to distinguish two neighboring point targets along the lateral direction. Those two parameters are not only determined by the transducer properties (the bandwidth, the quality, element pitch etc), but also by the signal pulse condition (width, frequency). Therefore, to increase the image resolution, in addition to the CMUT performance improvements (bandwidth), one can increase the inter-element "pitch" by increasing the signal pulse catching points, and/or shortening the pulse duration of the transmitter.
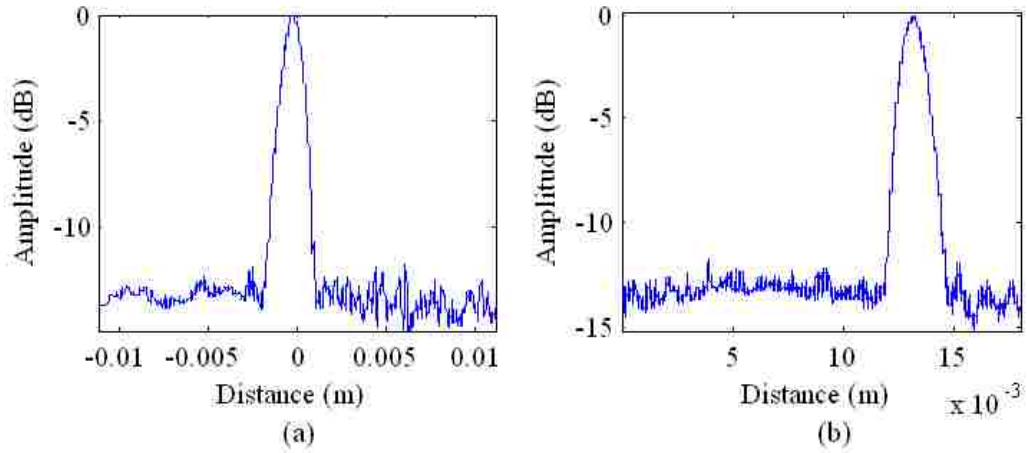
Figure 6.4 the point spread function projections in (a) lateral and (b) axial directions.

6.3 Photoacoustic Testing

Photoacoustic imaging combines high optical contrast with fine ultrasonic resolution, making it a viable alternative to other modalities used for imaging biological tissue. In photoacoustic imaging, optical absorbers of a pulsed laser source produce acoustic transients captured using a conventional ultrasound receiver. The detected photoacoustic waves are post processed to form an image of the optical absorbers. When a near-infrared (NIR) laser source is used, photoacoustic imaging has an added benefit of good penetration in biological tissue. The acoustic pressure, $p_0(r)$, immediately following a short laser pulse can be modeled as [82]

$$p_0(r) = (\frac{\beta c^2}{C_p})H(r) \qquad (6\text{-}3)$$

where β represents the thermal conductivity, C_p the specific heat capacity, c the speed of sound and $H(r)$ the absorbed energy map [83]. Thus, the initial pressure depends on the

117

distribution of absorbed laser energy and a leading constant term that represents the efficiency of converting heat to pressure, which is 0.11 for water at room temperature [84]. Moreover, H depends on the fluence, as well as tissue properties, including absorption and scattering coefficients and an anisotropy factor. Following light excitation, acoustic waves propagate according to the classic second order wave equation. An ultrasound receiver is used to capture acoustic waves and reconstruct the absorbed energy map.

Previous photoacoustic imaging work has typically relied on a single mechanically scanned piezoelectric transducer for detection of the laser-generated ultrasound. Using a CMUT array in place of a mechanically scanned element has a number of advantages. Large, two-dimensional arrays can be reliably fabricated using CMUT technology. A transducer array greatly speeds up the data acquisition time for a given aperture size. CMUT array geometries such as the ring array have also been demonstrated [5]. A ring array has the practical benefit that the laser light can come through the hole in the center of the array.

The experimental setup for Photoacoustic tomography using CMUT for the image of a wire (suture) (diameter 0.7mm) is shown as in Figure 6.5. In order to have a better image resolution, the diameter of the suture needs to be as thin as possible. A tunable laser source (Surelite^{TM} OPO, Continuum, Inc) was used to generate laser pulses with power density set as 10mJ/cm^2. This is lower than 20mJ/cm^2 – the ANSI standard for safe illumination [85]. The frequency is 20Hz. The wire (suture) phantom is protected by waterproof epoxy. The sensitive areas such as the BNC cable were wrapped with Aluminum foil to reduce the environment interference.

Similar to the ultrasound image acquisition described above, a single channel (element) was employed instead of all the elements on the CMUT receiver (parameters listed in table 5.1) due to the limit of readout circuit channel capability. The CMUT was carried by a translation stage so that it could move along the suture at a constant rate while scanning the suture to generate enough frames for beamforming. After the CMUT received the acoustic signal generated by the thermal expansion of the suture, the signal was amplified with a 40dB gain with an amplifier (Model 5073PR, Panametrics Inc., Waltham, MA). The RF signal was then digitized by an oscilloscope (TDS 3054B, LECROY) and transferred to the computer.
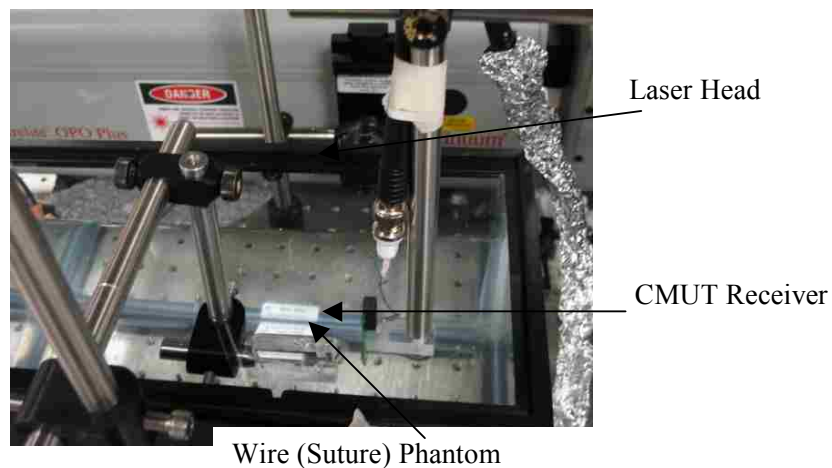
Figure 6.5 photograph of the experimental setup for photoacoustic imaging
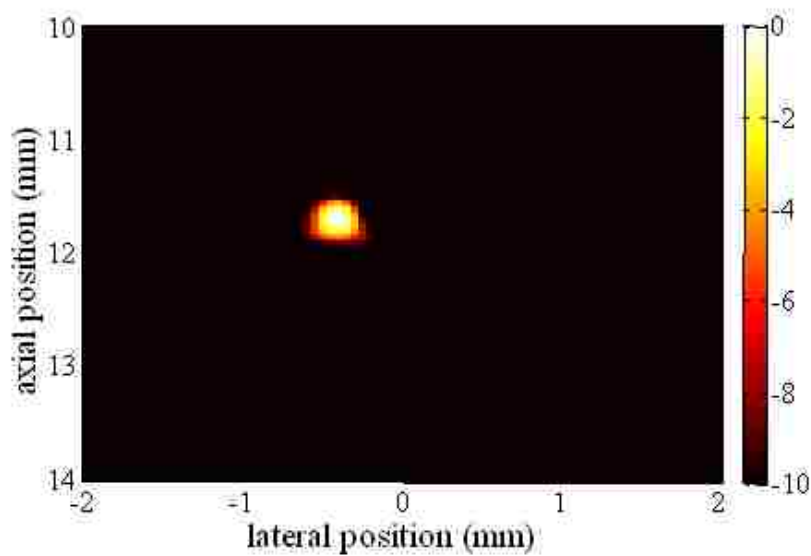
Figure 6.6 the photoacoustic image of suture

Similarly, by using B-form reconstruction method as discussed previously, the photoacoustic image of the cross-section of the suture was obtained as shown in Figure 6.6. At the dynamic range 10dB, it can be seen that the resolution is 300um laterally and 350um along axially.

By taking advantage of the photoacoustic techniques, another experiment was conducted to obtain the image of a lobster nerve cord (see the setup in Figure 6.7 and 6.8). The abdominal segment of the nerve cord was excised, stained (with dye NK2761) and positioned in the testing water tank. The laser source created the approximate illumination pattern (0.2x2cm) on the nerve cord illustrated by the dotted ellipse depicted in Figure 6.7. The CMUT device was placed perpendicularly to the laser beam axis and facing the nerve cord. The laser fired at PRR of 20Hz with the wavelength at 700nm. The power intensity is about 20mJ/cm^2.

Similarly, imaging reconstruction was conducted after signal data collection. The reconstructed photoacoustic image of a stained nerve is presented in Figure 6.9.
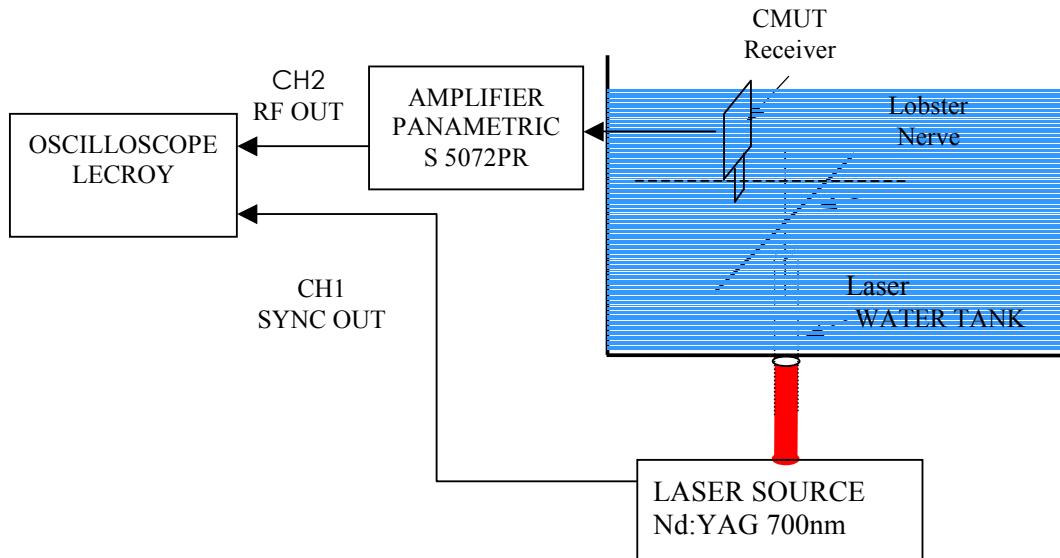
Figure 6.7 Schematic set-up for the photoacoustic imaging system

a)   b)
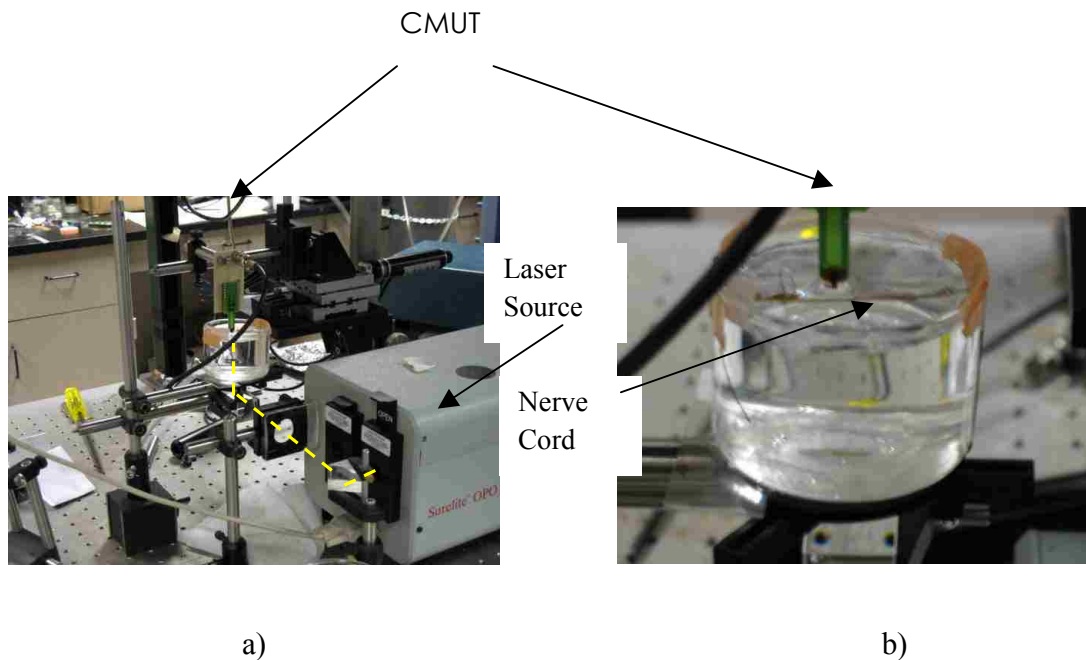
Figure 6.8 Photograph of the experimental setup.

The laser beam (yellow dotted line in a) goes from the bottom of the water "tank" and generate an illumination pattern on the nerve as shown in b). The CMUT mounted on a custom PC board worked as a receiver.
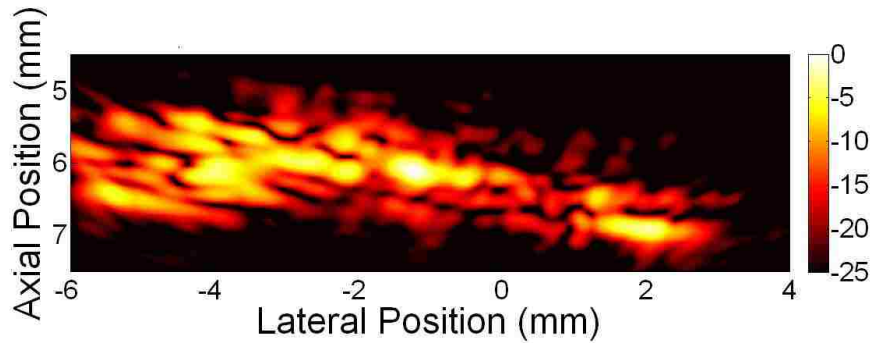
Figure 6.9 Beamformed Photoacoustic image (dynamic range =25dB) of the nerve stained with NK2761. Laser illumination was 700nm with an energy density near 20mJ/cm^2.

The photoacoustic image experiment using the commercial transducer instead of CMUT as the receiver was conducted. The setup is shown in Figure 6.10. The clinical used SonixRP Ultrasonic System was employed. The probe with 128 lines required 128 laser pulses. An FPGA (ezFPGA-C6-8, Dallas Logic Inc, Plano, Texas) provided synchronization between the laser and SonixRP. The Figure 6.11 gives the reconstructed image by SonixRP system. Comparing to photoacoustic image in Figure 6.9, with the same dynamic range (25dB), the image resolution is at relatively same level.

Figure 6.10 the photograph of the experimental setup using SonixRP System
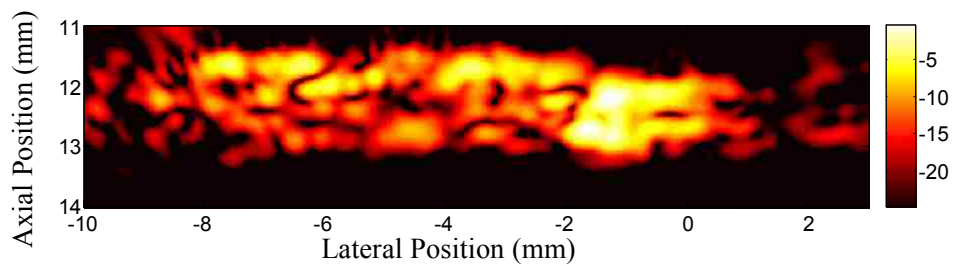
Figure 6.11 Beamformed Photoacoustic image (dynamic range =25dB) of the nerve stained with NK2761. Laser illumination was 700nm with an energy density near 20mJ/cm2 (Using SonixRP)

6.4 Summary

The pulse-echo images and photoacoustic images were created using a CMUT array element as a receiver with reasonable dynamic range. This demonstrates the viability of CMUT technology for ultrasound imaging.

CHAPTER VII

DISCUSSION

This project aims at the potential of CMUT for ultrasonic biomedical diagnosis and treatment from the perspectives of device structure, fabrication, and characterization. In addition to the achievements mentioned in chapter *IV* and *V*, some primary results should be discussed here. Section 7.1 will give some testing results using the fabricated high intensity CMUT discussed in chapter IV. In section 7.2, the primary results for blood flow-metering will be illustrated. CMUT is claimed to have better solution to integrate with supporting electronics, some approaches for CMUT-CMOS integration will be discussed in section 7.3. In addition, from the past experience, the encapsulation of the CMUT is also of importance and will be discussed in section 7.4.

7.1 The primary result for high intensity CMUT

We have already discussed the design guideline for the high intensity CMUT as well as its fabrication method in chapter IV. Similar to CMUT for imaging applications, the fabricated high intensity CMUT will be wire-bonded to the PCB for testing. The layout of the High Intensity CMUT is shown in Figure 7.1. There are 12 annular ring elements. The element pitch is 45μm. The gap distance of annular ring elements is about 0.35 μm. The elements at the outer circle are designed for imaging whose gap distance is 0.2 μm.

a)   b)
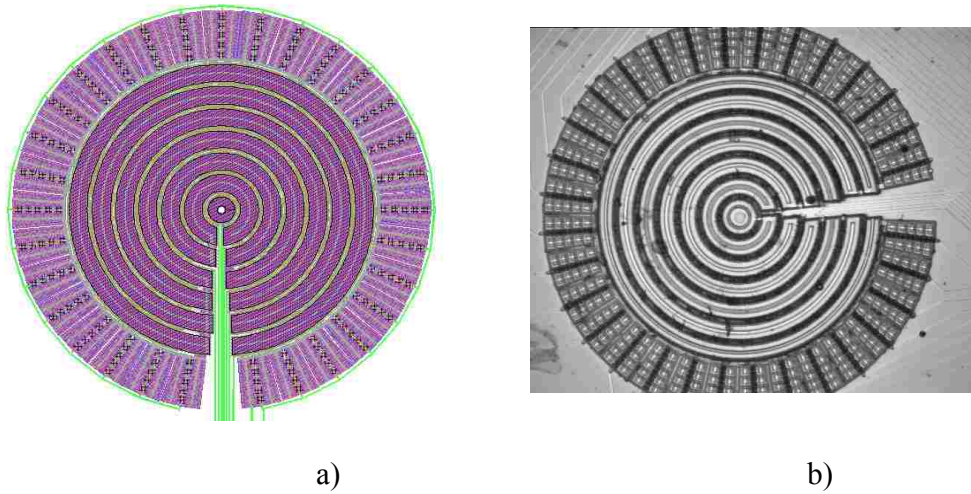
Figure 7.1 the High Intensity CMUT ring   a) the layout, b) the picture after fabrication

A commercial hydrophone (HMA, ONDA) was adopted to measure the output pressure of the CMUT operating as transmitter. A negative unipolar pulse was applied to the CMUT with zero DC voltage. The pulse width was 2us. The output signal is shown in Figure 7.2.
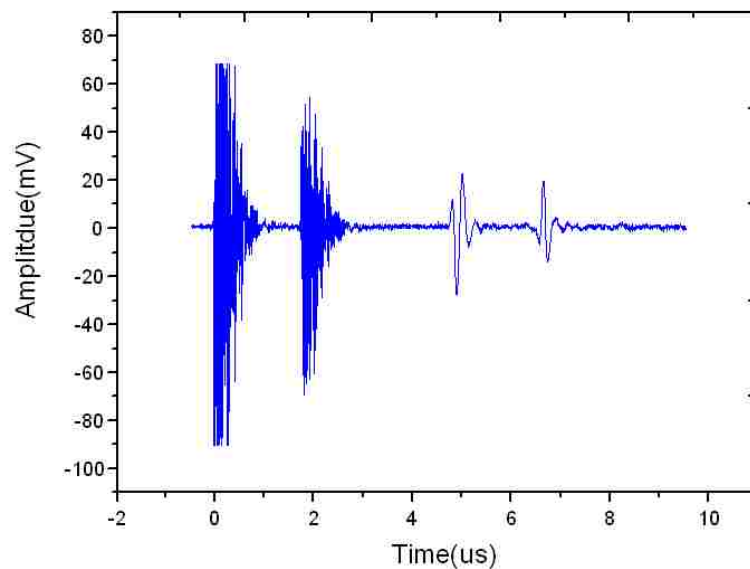
Figure 7.2 the output signal of high power element

By varying the pulse amplitude from 100V to 400V, and increasing the dc bias voltage from zero to 180V, we can obtain the output with different combination of ac actuation voltage and dc bias voltages. The converted output pressure using the sensitivity listed in this hydrophone datasheet [86] is demonstrated in Figure 7.3.
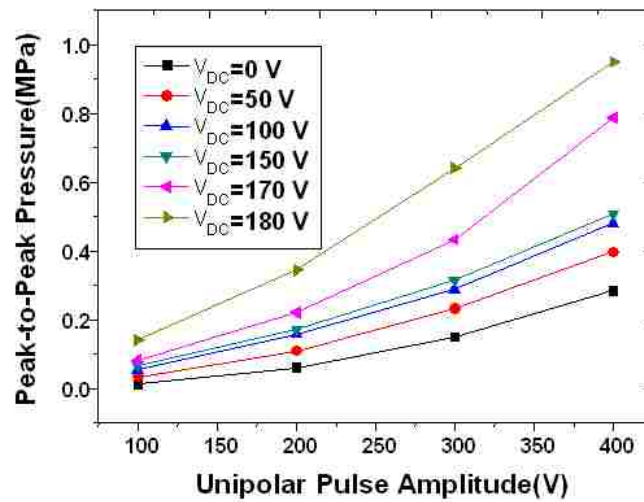
Figure 7.3 the output pressure (MPa) vs. the ac actuation voltage

When the AC amplitude and the dc bias DC increase, the output will increase accordingly. The output pressure could reach 0.95MPa when the AC actuation voltage is 400V and the dc bias voltage is 180V. Accounting for attenuation and diffraction losses, the pressure on the CMUT surface is greater than this value. It is worth noting that all the ring elements are electrically tied together. There is no phase delay between the elements to form the focal point in this experiment due to the limit of the peripheral circuits. Otherwise, we would expect higher power intensity.

7.2 Blood Flow metering [87]
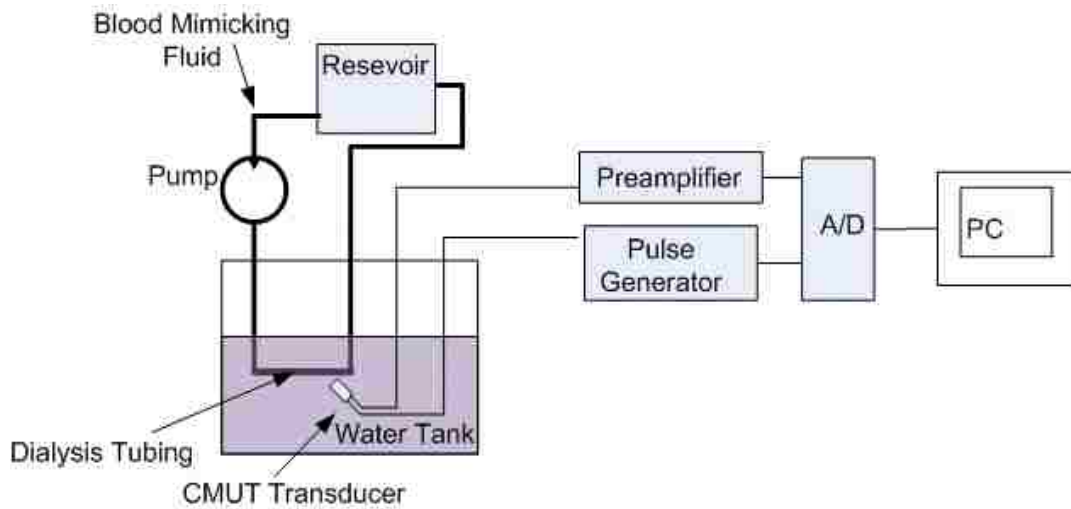
Figure 7.4 the block diagram of the blood flow meter experimental setup

The block diagram of blood flow velocity metering experimental setup is shown in Figure 7.4. This system consists of two parts: the extracorporeal circulation network and the CMUT control circuit. Extracorporeal circulation is a procedure used in cardiac surgeries for which the blood circulations are controlled by an artificial setup, e.g., a mechanical pump, instead of the patient's heart. A commercial peristaltic pump (Master flex, Cole-Palmer instrument company, Vernon Hills, IL) with the capacity to pump 50-500 ml/min was used in this system to drive a blood mimicking fluid (CIRS model 046, Tissue Simulation Technology, Norfolk, VA) to circulate through a rubber tubing system in this experiment. The blood mimicking fluid had physical characteristics (density, viscosity and particle size) and acoustical properties (velocity, backscatter and attenuation) close to that of blood, thus providing a useful mimic for blood flow measurement. The external diameter of the rubber tube is 4.8mm. It was filled with a blood mimicking fluid and submerged in a water tank in this experiment. In order to

compare with the real value of the flow rate, a laser Doppler monitor was first employed to monitor the real time flow velocity of this mimicking fluid.

The CMUT array probe was oriented at 60º with respect to the orientation of the flow tube in the measurement. The ultrasound beam was focused upon the center of the tube in order to ensure maximized ultrasound energy projection on the scatters (the blood mimicking fluid). The CMUT devices were excited by a pulse generator (Olympus 5077PR) with a 100V tone burst signal with a center frequency of 2.2 MHz width and PRF 2 KHz. The signal from the receiver was pre-amplified and then was sent to the A/D converter with a sampling rate of 200MHz. Finally, the signal was sent to the computer for data processing. The parameters of the data collection system were summarized as follows.

ITEMS	VALUES
Transducer center frequency	2.2MHZ
Signal sampling rate	50MHz
Pulse repetition frequency	2KHz
Transducer 6-dB bandwidth	0.8MHz
Ultrasonic measurement angle	60 degrees
Volume flow rate	200 ml/min
A line length (2000 samples)	20us
Acoustic velocity	1500m/s
Amplifier gain	40dB
Amplifier Bandwidth	400MHz

Table 7.1 The Parameters for the data collection system

The time-domain method was used for the data processing [87]. In the time domain approach, the correlation function describes the degree of relationship between two

received ultrasound echoes and plays an important role in determining the blood flow velocity. The details of this method can be found in reference [87]. A flow rate resolution of 1.5mm/s was achieved in the measurements.

7.3 CMUT Integration with CMOS Electronics

CMUT have potential to be integrated with CMOS electronics because of the compatibility of CMUT fabrication process steps with CMOS process steps. The choices for integration of electronics with CMUT can be broken down into two basic categories: 1) Monolithic integration in the same chip 2) Flip chip bonding the CMOS chip to the transducer array substrate.

7.3.1 Monolithic Integration

Monolithic integration of CMUT with electronic circuits has been proposed in literatures [88-89,106]. It has been demonstrated that a modified CMOS or BiCMOS process could be used to fabricate Ultrasonic transducers on the same silicon substrate with electronic circuits.

a) Post-processing

Post processing is a modular approach to integration, where the CMOS is processed first in one module, and then the microstructures are processed in a following module. The modularity ideally allows the flexibility for micromachining, but unfortunately, this attractive idea is accompanied by many technical problems. The temperature ceiling of the post-CMOS process puts a limit that the high-temperature microstructure process is not allowed after CMOS process. Although the low-temperature fabrication technology emerged using low –temperature PECVD nitride as CMUT membrane, the quality of this

PECVD nitride is still a notable concern [64]. A two-polysilicon four-metal (2P4M) CMOS process was used for sensor fabrication in [90]. The Metal3 and Metal4 layers not only served as CMOS interconnection, but also acted as the electrodes of the MEMS sensor. This approach reduced the complexity of the fabrication. However, control over the gap distance is very limited due to the fabrication process.

b) Mixed Processing

The mixed processing is the approach where the process steps of CMOS and micromachining are intermixed in one process flow. The advantage of this technique is that a process can be designed such that all high temperature steps can be done first before any low temperature materials are present. The disadvantage is that each new product with dissimilar technological requirements requires a significant amount of design investment. This approach therefore might be suitable for the matured, mass production line in industry. Motorola has developed a mixed process for the integration of a two-poly-silicon pressure sensor with on-chip CMOS circuits. Analog Device Corp invested in the mixed process for the inertial sensors with CMOS electronics. However, it is very difficult to achieve this process at university facilities.

7.3.2 Flip-chip bonding

Another approach of integration is to fabricate the electronics and the transducers on separate wafers and then integrate with wafer bonding [89, 91]. In this way, high temperature processes can be used to fabricate high density and high performance CMUT arrays with high yield and uniformity.

From discussion in Chapter IV, the CMUT array (especially 2D array) usually requires element pitch smaller than $\lambda/2$ in order to reduce the aliasing. For the CMUT

working with frequency at 5MHz or more, the element pitch is expected to be 150μm or less. One of the major problems associated with this small element pitch array is to address each element effectively. Through-wafer interconnect technology provides an approach to connect the transducer elements vertically to the bonding pads on the backside.

7.3.3 Through-Wafer Interconnect

Through-wafer interconnects not only shrink the dimensions of the array, but also reduce the parasitic capacitance from the conductive column to the substrate and the series resistance. Many processes have been previously used to fabricate through-wafer interconnects [92-97] including wet etched or dry etched polysilicon filled interconnects [98]. It has been demonstrated using KOH or TMAH etching [92][95]. However, this approach results in a poor aspect ratio and/or large footprint at the wafer surface. Since the advent of deep reactive ion etching (DRIE), double side ICP dry etching has been employed to produce deep holes. The holes are filled with dielectric layers and then in-situ doped polysilicon (for low frequency application) or metal (copper). However, the relatively large holes (20μm or larger in diameter) designed to meet the aspect ratio (20:1) for regular thickness wafers resulted in topography that brings difficulties for the followed uniformly photo-resist spinning. In addition, it's difficult to fill up the through holes larger than 10μm without metal electroplating method, which is normally not allowed at the early stage of CMUT fabrication.

Different from the research in those literatures, we proposed a new through-wafer interconnect structure, in which an air isolated gap was formed between the interconnect column and the dielectric layer and the substrate ground. Since air has relatively low

dielectric constant, the parasitic impedance will be greatly reduced; in order to overcome the challenges for process steps following the through-wafer etch, the size of the via was largely reduced. The fabrication of this through-wafer interconnect can integrate with the followed process of CMUT array successfully. In what follows, the fabrication steps were be given in detail.

Thinner (300μm) silicon wafers are used rather than regular 500μm-thick substrates was adopted, which allows smaller through-hole etching (6~8μm). The process started with 1.0um thermal oxidation for DRIE mask (as shown in Figure 7.5). This mask can help reduce the chipping and cracks around via induced by the lengthy deep etching process. The thermal oxide layer was patterned and then removed by RIE, following approximately 150min DRIE from both sides using an STS tool with alternating etch and passivation cycles. Because etch-rates for features with dimensions shorter than 30um in at least one dimension are significantly reduced, the through wafer hole shape is chosen as 8μmX35μm trench instead of a round hole with 8μm in diameter. Oxygen plasma ashing was then performed in order to remove the residual materials or by-products from the Si dry etch. After removing the etching mask, another 2um thermal oxide was grown followed by deposition of 0.3μm LPCVD nitride and 0.4μm LPCVD oxide. A thick LPCVD LTO (1.3μm) was deposited at 400°C as sacrificial oxide layer. This sacrificial layer was then patterned and dry-etched. A layer of in-situ doped LPCVD Polysilicon (1μm) was deposited. This poly layer filled up the trench holes to form a continuous conduction path through the wafer. It also worked as the support beam for this conduction path and the structural material for the bottom electrode of the CMUT array. After flood etching of the backside polysilicon, the sacrificial layer was released in

straight HF solution. The released interconnect with the support beam was illustrated in Figure 7.6 a). From the experiment, no inconvenience was caused during the process after the trenches were formed.

a) Start with <100> n type wafer with 300um thickness, oxidation and patterning of the etch mask

b) Dry etching from both side to form through via (Litho #1 & #2)

c) Thermal oxidation, LPCVD nitride/oxide deposition Sacrificial Layer LTO deposition

d) Sacrificial layer patterning, etching (Litho#3) and flood etching (back)

e) In-situ doped poly deposition, patterning

f) HF releasing

Figure 7.5 the process flow of the air-isolated interconnect through wafer fabrication
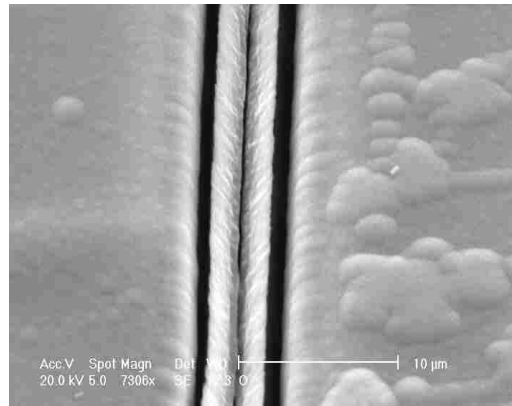
a)
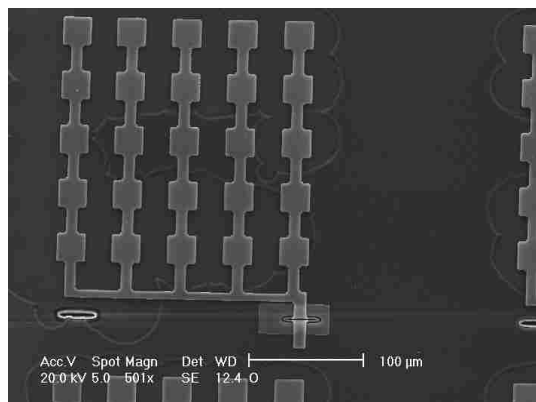
b)

Figure 7.6 the SEM pictures of the CMUT array after the deposition of the bottom electrode

7.4 The Encapsulation

Encapsulation is a mandatory step to protect the CMUT from contacting the water/living tissue and to provide electrical isolation. Parylene C has been used and the coating must be thin to minimize effects on device performance. Parylene C has been proved to be a good passivation material for chronic neural testing [99]. But for the devices with moving parts like CMUT, the motion-caused stress can result in cracking and pinholing of parylene C. Normally the parylene C film was patterned (oxygen plasma dry etching) for the purpose of the exposure of bonding pad area. This patterning was

proved to weaken the parylene C adhesion to substrate and result in the parylene film delamination [100]. This delamination caused the current leakage when operated in liquid. In the past experiment, we have observed that air bubbles were generated on the surface of the CMUT plate after a long-term test. This was the indication that the water was likely decomposed into Hydrogen (H_2) and Oxygen (O_2) due to the current leakage.

To alleviate this problem, the CMUT was wire-bonded before the parylene coating so that the parylene patterning to open the bonding pad area was not necessary. Our recent experiment showed that, with this modification, no air bubble were generated at the CMUT surface under the similar testing condition.

7.5 Summary

Several topics were discussed in this chapter. The primary test result of high-intensity CMUT was presented in section 7.1. It demonstrated the capability of CMUT working as high-intensity Ultrasonic Transducer for the treatment/therapy. The blood flow rate metering using CMUT was discussed in section 7.2. In section 7.3, the approach to integrate the CMUT with CMOS was analyzed. The fabrication of air-isolated through wafer interconnection was given in detail. Finally, the issue regarding the encapsulation was addressed.

CHAPTER VIII

CONCLUSION

CMUT arrays can deliver comparable device characteristics to their piezoelectric counterparts and shows advantages in manufacturing cost and system compatibility for medical diagnosis/treatment. The key advantages of the CMUT technology can be summarized as ease of fabrication, improved sensitivity and bandwidth and relative independence of the material properties. Taking advantage of bulk micromachining technology which allows high-precision shaping on the silicon substrate of CMUTs, miniature CMUT arrays for intravascular ultrasonic imaging, blood flow rate metering, and image-guided therapy have been successfully developed in this thesis work. In the following, a summary of this work will be made and the future work will be suggested.

8.1 Conclusion

Miniature CMUT arrays for minimally invasive medical applications have been developed. A two-layer polysilicon surface micromaching process has been developed for fabricating the CMUTs and several novel device designs, including a surface-micromachined bossed membrane, have been used for improved device performance. Polysilicon was chosen as the building material for the CMUT membrane. Compared to the silicon-nitride-membrane CMUT devices, the polysilicon-membrane CMUT requires a much shorter release time in the fabrication process and delivers excellent mechanical characteristic as the key part of an acoustic transducer. A novel dielectric post structure was also developed for the CMUT devices for preventing membrane shorting. Combining the CMUT process with the bulk-micromachining process which shapes the silicon

substrate into miniature platforms, three different CMUT arrays for minimally invasive applications have been developed: the monolithic three-dimensional CMUT array for panoramic vision, the needle-shaped CMUT array, and the ultrasound image-guided therapy chip.

A comprehensive characterization of these miniature CMUT arrays has been accomplished on the device level. Preliminary imaging experiments using these devices have been demonstrated. In these characterization experiments, membranes with different shapes were tested for comparison with results predicted by finite element analysis.

An air-isolated through wafer interconnection structure was designed and preliminary testing structures were prototyped, aiming for use for CMUT through-wafer inter-connection. Prototypes and preliminary testing results for an ultrasound image-guided therapeutic chip has also been demonstrated.

Overall, the major contributions of this thesis work include:

1) A two-layer polysilicon surface micromachining process mixed with a bulk micromachining process was developed for fabricating the CMUT devices.

2) A CMUT with a bossed membrane was designed, prototyped, and characterized. It was confirmed through the testing results that the acoustic bandwidth was improved over its planar-membrane counterpart due to the bossed membrane structure.

3) CMUT devices with an array of dielectric columns embedded in the membrane were developed for preventing membrane shorting. Preliminary testing results of

these devices have shown that this design was helpful in alleviating the charge trapping problem.

4) A novel architecture to integrate several planar CMUT arrays on a 3D hexagonal silicon prism for viewing the front direction and 360º side directions simultaneously was constructed. The size of these hexagonal imager prisms from 1 to 4 mm in cross-sectional width across the hexagon and from 2 to 4 mm along the prizm length, which is small enough for many internal imaging applications.

5) A CMUT probe was developed as the prototype for minimally invasive blood flow rate metering. A flow rate resolution of 1.5mm/s was achieved in the measurements

6) A high-Intensity CMUT Annular Rings structure was developed. The output pressure from an unfocused annular ring reaches as high as 0.95MPa. The design could be potentially used for ultrasonic therapy or image-guided therapy.

7) Preliminary experiments using a CMUT array for photoacoustic imaging was demonstrated.

8) Finally, a preliminary study on the fabrication of an air-isolated through wafer interconnect was conducted for the integration of the CMUT and CMOS electronics.

8.2 Recommendations for Future work

Looking into the future, the success of CMUT relies on the further improvement in the following aspects.

8.2.1 The CMUT design and fabrication

There are research opportunities in the improvement of design/modeling and fabrication, which include 1) the CMUT-medium interface modeling; 2) novel CMUT structure construction, 3) new fabrication techniques; 4) reduction of cross-talk effects; 5) development of theoretical models for new operation regimes, 6) front-end and backend circuit design, 7) improvement of interconnection and 8) packaging schemes. Better acoustic models to explain the reactions between the CMUT and the surrounding medium need to be established. New CMUT structures and fabrication techniques to reduce the parasitic and charging trapping problems are still under investigation. For further development of the three prototypes for minimally invasive applications in this research, increasing the frequency of operation is an area that needs to be explored sufficiently.

8.2.2 Therapy and treatment

Through advancement on the device and system level of ultrasonic transducers, the applications of ultrasound in medicine extend beyond diagnosis and reach the domain of treatment and therapy. With the ability to produce acoustic pressure levels larger than 1MPa, CMUT devices are more than capable of being used for ultrasonic treatment including changing the tissue temperature or cell membrane properties, as well as ablation.

8.2.3 System integration

An ultrasonic system is composed of many building blocks which are not limited to the transducer arrays, such as the front-end circuits, ADCs, beamforming schemes. One of the important areas of research remaining to be explored is the integration of all the blocks to form a specific clinically useful instrument. Packaging is a related area, which

requires attention for the implementation of these systems. Medical instruments have to comply with certain regulations that result in an extended set of specifications regarding material choices, electrical limits and temperature limits. Therefore, the design of these instruments demands a collective effort from technologists and clinicians.

8.2.4 Application oriented issues

Small, portable physical form factors, high resolution, and real-time 3D imaging capabilities are the major directions being pursued by CMUT-based medical ultrasonic systems. Fabricated using processes adapted from those used for integrated circuits fabrication, CMUT can potentially be manufactured at a low cost. This cost advantage makes CMUT suitable for many applications not possible with the piezoelectric devices. For example, an affordable CMUT array can be added on many of existing medical instruments to provide additional diagnostic information for improved diagnostic results

The application of CMUT is not limited to biomedicine. A CMUT microphone [103-104] was proposed to solve the problems in the audio range/harsh environment that traditional MEMS microphone could not reach. Many techniques in this application are still waiting to be explored. In conclusion, future research can be directed towards the development of new fabrication and design, the increased levels of integration, higher operating frequencies, lowering manufacturing cost, or combinations of these depending on the application of interest.

APPENDICES

APPENDIX A

PROCESS FLOW OF CMUT FABRICATION

1 Start Wafers Preparation: Silicon 5-10 Ω -cm, n-type (or p-type), <100>
    scribe numbers on process and control wafers
    Piranha clean (H_2O_2 :H_2SO_4= 1 : 1) 20 min
2. Dope Substrate (optional)
  2.1 Pre-Furnace Clean
    RCA organic clean (NH_4OH : H_2O_2 : DI water =1 : 1: 5), 85°C, 10 min,
    HF dip (HF : DI water = 1: 10), 30 sec.
    RCA ionic clean (HCl : H_2O_2 : DI water = 0.85 : 0.85 : 5), 85°C, 10 min
    Q-rinse until resistivity > 15M Ω .

  2.2 POCl$_3$ Dope (n-type) Substrate
Furnace:	B3
Program:	PHOSDEP2
Parameter table	POCL DEP
Temperature:	950 ^{o}C
Deposition time:	30min
Drive-in time	1hr
O_2 flow:	110
Low N_2 flow	275
Control wafers:	Cl and C2

3. Thermal Oxidation   **(target thickness 2um)**
Furnace:	B2
Temperature:	1100 ^{o}C
Deposition time:	
Drive-in time	1hr
O_2 flow:	110
Low N_2 flow	275
Control wafers:	Cl and C2

4. LPCVD Oxide/Nitride (optional)
Furnace:	C4
Program:	HTO4HR+
Parameter table	CVD
Temperature:	920˚C
Deposition rate:	~50Å/min

5. LPCVD Polysilicon   **Target: 0.5um**
Furnace:	C3
Program:	LSPOLY
Parameter table	FRANCIS
Temperature:	588˚C
Deposition time:	2hr10min

6. POCl$_3$ Dope the polyslicon layer
Furnace :	B3
Program:	PHOSDEP2
Parameter table:	POCL DEP

Temperature:	950˚C
Depostion time	10min
Drive-in time:	1hr
O2 flow:	110
Low N2 flow:	275
Control wafers:	C5 and C6

7. Lithography Mask #1 POLY0

7.1 Spin Photoresist 1813

spin speed	4K/min
spin time	30sec
softbake	1min @ 115˚C
Thickness	1.3um

7.2 Expose and Develop

Aligner:	MA6
Exposure time:	6sec
Developer:	MF319
Develop time:	1.1min

7.3 Descum

Equipment	March Asher
O_2 flow:	17 sccm
Pressure:	250 mTorr
Power:	80W
Time:	1min

7.4 Poly0 etching

Equipment	Plasma Therm
SF_6:	12sccm
O_2	3sccm
Pressure	10mTorr
Power	50W
Time	
Etch rate	~600A/min

Rotate wafers 180° at half time

7.5 Strip Photoresist

Chemical	PRS2000
Time	5min

Visual inspection and probe to detect opening of the dielectric layer

8 Dielectric (Oxide/Nitride) deposition (optional)

8.1 Pre-furnace clean

8.2 Oxide/Nitride doposition (500Å/800 Å)

Furnace:	C4
Program:	OX/NT
Parameter table	CVD

9 Oxide (PSG) deposition (outsourcing to Berkeley)

thickness:	0.3um

10 PSG densification

10.1 PFC (No HF dipping)

10.2 Densification

Furnace:	C4
Program:	N2ANNEAL
Parameter table	OXIDATION
Temperature:	1000ºC

Deposition time: 0
Drive-in time   1hr

For PSG as the sacrificial layer, densification is necessary before depositing poly 1 layer. Undensified PSG will result in bubbles on the surface, the reflow during the consequent high temperature process such as doping and annealing will result in poor step coverage and cause device short.

---

11 Lithography Mask 2 Anchor

11.1 Spin Photoresist 1813
spin speed   4000rpm
spin time   30sec
softbake   60sec
Thickness   1.3um

11.2 Expose and Develop
Aligner: MA6
Exposure time: 5.5sec
Developer: MF319
Develop time: 1.1min
Hard bake   No

11.3 Descum
Equipment   March Asher
O_2 flow: 17 sccm
Pressure: 250 mTorr
Power: 80W
Time: 1min

11.4 Anchor etching
Equipment   Plasma Therm
CHF_3 15sccm
CF_4 15sccm
Pressure   40mTorr
Power   100w
Rotate wafers 180° at half time

11.5 Strip Photoresist
Chemical   PRS2000
Time   10min

Visual inspection and probe to detect opening of the dielectric layer
The etch time varies with the thickness of oxide. The normal etch rate is 150A~200A/min
Visual inspection and probe detection (a little bit over etch allowed

---

12 Lithography Mask 2A HIGHPOWER   (OPTIONAL, For High-power devices)

12.1 Spin Photoresist 1813
spin speed   4000rpm
spin time   30sec
softbake   60sec
Thickness   1.3um

12.2 Expose and Develop
Aligner: MA6
Exposure time: 5.5sec
Developer: MF319
Develop time: 1.1min
Hard bake   No

12.3 Descum
Equipment   March Asher
O_2 flow: 17 sccm
Pressure: 250 mTorr
Power: 80W
Time: 1min

12.4 Time controlled Etching

Equipment	Plasma Therm
CHF_3	15sccm
CF_4	15sccm
Pressure	40mTorr
Power	100w
Rotate wafers 180° at half time	

12.5 Strip Photoresist

Chemical	PRS2000

13 Poly 1 Deposition

13.1 PFC

13.2 Poly 1 deposition   (low stress Poly)

Furnace:	C4
Deposition time:	4hr20min

13.3 Phosporous doping

Furnace:	B3
Deposition Time	30min
Drive-in time	20min

13.4 Annealing

Furnace:	B4
Annealing time	1hr

14 Lithography Mask 3 POLY1

14.1 Spin Photoresist 1827

spin speed	4000rpm
spin time	30sec
softbake	60sec
Thickness	2.7um

14.2 Expose and Develop

Aligner:	MA6
Exposure time:	13sec
Developer:	MF319
Develop time:	1.1min
Hard bake	90sec

14.3 Descum

Equipment	March Asher
O_2 flow:	17 sccm
Pressure:	250 mTorr
Power:	80W
Time:	1min

14.4 Poly1 etching

Equipment	STS
C_4F_8	90sccm
SF_6	40sccm
Pressure	15mTorr
Power	Control Power 15W, coil Power 800W
Time	15mins
Rotate wafers 180° at half time	

14.5 Strip Photoresist

Chemical	PRS2000

- Using STS to avoid stringer structure. The etching selectivity of STS is better than Semigroup and Plasmatherm RIE

15 LPCVD Oxide Deposition / Poly deposition

15.1 PFC

15.2 LPCVD oxide Deposition   **C4**   **800Å**
15.3 Poly Deposition   **C3**   **0.3um (or 0.6um)**

16 Lithography, MASK #4 HIGHPOWER

16.1 Spin Photoresist 1827

spin speed	4000rpm
spin time	30sec
softbake	60sec
Thickness	2.7um

16.2 Expose and Develop

Aligner:	MA6
Exposure time:	13sec
Developer:	MF319
Develop time:	1.1min
Hard bake	90sec

16.3 Descum

Equipment	March Asher
O_2 flow:	17 sccm
Pressure:	250 mTorr
Power:	80W
Time:	1min

16.4 Poly1 etching

Equipment	STS
C_4F_8	90sccm
SF_6	40sccm
Pressure	15mTorr
Power	Control Power 15W, coil Power 800W
Time	15mins

Rotate wafers 180° at half time

16.5 Strip Photoresist

Chemical
Time

17 Sacrificial layer Releasing

17.1 Release etching

chemical   HF:Diwater =1:1   7mins

17.2 Rinse with DI water   (10mins)
17.3 IPA and Methanol   (30mins)
17.4 Supercritical CO2 drying
17.5 Visual inspection and Probe detection

18 GSI-PECVD Deposition

SiH_4	15% Tar
N_2O	99% Tar
He	50%
Temperature	380ºC
Thickness	3.0um

19 Lithography Mask 5 SEAL

19.1 Spin Photoresist 1827

spin speed	2000rpm
spin time	30sec
softbake	60sec @110C
Thickness	2.7um

19.2 Expose and Develop
Aligner:	MA6
Exposure time:	22sec
Developer:	MF319
Develop time:	1.1min
Hard bake	90sec

19.3 Descum
Equipment	March Asher
O_2 flow:	17 sccm
Pressure:	250 mTorr
Power:	80W
Time:	1min

19.4 PECVD Oxide etching
Equipment	Semigroup RIE
CHF_3	25sccm
CF_4	25sccm
Pressure	40mTorr
Power	180W
Time	~100min
Etch rate	~300Å/min
Rotate wafers 180° at half time	

19.5 Strip Photoresist (Piranha clean)
Chemical	H_2O_2 (800ml)+H_2SO4 (960ml)
Time	15min

---

20   arylene C deposition
Equipment :	PDS2010
Thickness	~3um

---

21 Lithography Mask #6 PARYLENE
21.1 Spin Photoresist 9260
spin speed	4000rpm
spin time	30sec
softbake	5min@100ºC

21.2 Expose and Develop
Aligner:	MA6
Exposure time:	50sec
Developer:	MF400
Develop time:	2hr30min
Hard bake	5min@100ºC

21.3 Descum
Equipment	March Asher
O_2 flow:	17 sccm
Pressure:	250 mTorr
Power:	80W
Time:	1min

21.4 Parylene C etching
Equipment	SemiGroup RIE
O_2	100sccm
Pressure	100mTorr
Power	150W
Etch rate	1500Å/min

21.5 Strip Photoresist
Chemical	Acetone +IPA

notes: PR stripping * (hot PRS2000 no longer than 5min)

22 Lithography Mask #7 METAL

22.1 Spin Photoresist AZ 5214
spin speed	1000rpm
spin time	30s
softbake	1.5min @ 90ºc

22.2 Exposer and developing
Aligner:	MA6
Exposure time:	2sec
Hot plate Baking	1.5min @115ºc
Flood Exposure time	90Sec
Developer:	MF319
Develop time:	1.5min
Hard bake	

22.3 O$_2$ Descum   2mins
22.4 BHF dipping
Chemical	Buffered HF
Time	30sec

23 Metal Sputtering and Liftoff

23.1 Sputtering Cr/Au (300A/4000A)
23.2 Liftoff
Immerge the sample into Acetone for overnight
Use DI water gun to blow the surface gently.
Immerge into Acetone for overnight
DI water gun gentle blow
Swapping the surface softly

24 Passivation (oxide and Polymer)

24.1 PECVD oxide deposition (2000A)
24.2 Parylene C coating   1um

25 Lithography Mask #8 PADOPEN

25.1 Spin Photoresist   1827
spin speed	2000rpm
spin time	30sec
softbake	1min@110ºC

25.2 Expose and Develop
Aligner:	MA6
Exposure time:	22sec
Bake	(optional)
Developer:	MF319
Develop time:	1.1min

25.4 Polymer etching on both side (back and Front)
RIE etching   10min
Probing to detect the opening pad
25.5 Strip photoresist
Acetone and IPA, DI water to rinse off

26 Lithography Mask #9 SHAPE

26.1 Spin Photoresist   AZ9600
spin speed	2000rpm
spin time	30sec
softbake	5min@100C

26.2 Expose and Develop

Aligner: MA6
            Exposure time: 60sec
             Developer: MF400
            Develop time: 2.5min
             Hard bake   5min@100C
       26.3 Oxygen plasma Descum
       26.4 RIE etching
            Dry etching to cut through dielectric stacks
            RIE etch on the backside to remove the stack layers of dielectrics
            STS etch 30~40um trenches into silicon substrate

 27 HF_Nitric Wafer Thinning
       27.1 Photoresist Coating   AZ9260
             speed   4000rpm
              hard baking   15sec @115ºC
       27.2 Flip the wafer and glue it with a glass wafer
       27.3 Hard baking for 20min
       27.4 HF_Nitric wafer thinning for about 30mins (follow the SOP of HF-Nitric wafer thinning)

 28 Lithography Mask #10 BACKTRENCH
       28.1 Spin Photoresist   AZ9260
             spin speed   2000rpm
             spin time   30sec
             softbake   5min@100ºC
       28.2 Expose and Develop
            Aligner: MA6
            Exposure time: 60sec
            Developer: MF400
            Develop time: 2min30sec
             Hard bake   5min@100ºC
       28.3 Oxygen plasma Descum
       28.4 RIE etching
            Equipment   STS
            C_4F_8 85.0sccm
            SF_6 160 sccm
            Pressure   15mTorr
            RF Power   Etch 250W-platen Generator
                                        Passivation 600W-Coil Generator
                                        Etch 800W
            Time   15mins
            Rotate wafers 180° at half time

 29 Final Release
       29.1 Immerse into Acetone and IPA
       29.2 Rinse
        29.3 Bake
        29.4 Probing test

TABLE A.1.THE LIST OF MASKS FOR PHOTOLITHOGRAPHY

NO	NAME	CLEAR/DARK	DESCRIPTION
1	POLY0	Clear	
2	ANCHOR	Dark	
2A	HIGHPOWER	Clear	(Optional)
3	POLY1	Clear	
4	HIGHPOWER	Clear	The same mask as 2A
5	SEAL	Dark	
6	PARYLENE	Clear	
7	METAL	Clear	For liftoff
8	PADOPEN	Dark	
9	SHAPE	Dark	
10	TRENCH	Dark	

APPENDIX B

THE PCB BONDING PROCEDURE

1) **Die patching**

Using the epoxy and hardener to attach the device to the PCB, cure it at the oven at 90°C for 15 to 20mins

2) **Wire bonding**

3) **Encapsulation**

    3-1   using 353 NDT+Epoxy hardener (ratio 10:1) to build up a barrier around the bonding pad area in order to prevent the fluidic-like epoxy flowing around;

    3-2   Curing it at the oven at 90°C for 10min until the barrier material turns into red color;

    3-3   Deposit the 353ND+Epoxy hardener (10:1 ratio) to fill up the bonding pad area;

    3-4   Curing it at the oven at 90°C for 30min;

4) **Tin soldering**

Mount the Connector on the Board and then solder the pins.

5) **Primary testing**

Electrically test the resistance between the ground the electrode, check if there is any electrical short problem.

REFERENCES

[1] Sokolvo, S. Y. "On the problem of the propagation of ultrasonic oscillations in various bodies." Elek. Nachr. Tech. 6:454-460, 1929.

[2] Dussik, K. T. "On the possibility of using ultrasound waves as a diagnostic aid." Neurol. Psychiat. 174:153-168. 1942.

[3] J. C. Somer, "Electronic Sector Scanning for Ultrasonic Diagnosis", Ultrasonics, vol. 6, issue 3, July 1968. pp 153~159

[4] Olaf T. Von Ramm, Ferderick, Thurstone, "Cardiac Imaging Using a Phased Array Ultrasound System" Circulation Vol 53, No.2, Feb. 1976 pp. 258~262.

[5] Omer Oralkan, " Acoustical Imaging Using Capacitive Micromachined Ultrasonic Transducer Arrays: Devices, Circuits, and Systems", Ph.D dissertation, Stanford University, March 2004.

[6] http://atcaonline.com/phone/Reis.html

[7] A.Ballato, "Piezoelectricity: old effect, new thrusts," IEEE Trans. Ultrason., Ferroelect., Freq. Cont., Vol. UFFC-42, pp.916~926, Sep. 1995.

[8] S.Fujishima, "The history of ceramic filters," IEEE Trans. Ultrason., Ferro-elect., Freq. Cont., vol. UFFC-47, pp 1~7, Jan 2000.

[9] M.I.Haller and B.T.Khuri-Yakub, "A surface micromachined electrostatic ultrasonic air transducer," in Proc. IEEE Ultrason. Symp., 1994, pp. 1241-1244.

[10] F.V.Hunt, "Electroacoustic: The analysis of transduction, and its historical background". New York, NY: Acoustical Society of America, 1982.

[11] D.W.Schindel and D.A.Hutchins, "The design and characterization of micromachined air-coupled capacitance transducers," IEEE Trans. Ultrason., Ferroelect., Freq. Cont., vol.UFFC-42, pp 42-50, Jan 1995.

[12] P.C.Eccardt, K.Niederer, T.Scheiter, and C.Hierhold, "Surface micromachined ultrasound transducers in CMOS technology," in Proc. IEEE Ultrason. Symp., 1997, pp 959~962.

[13] X. C. Jin, I.Ladabaum, and B. I. Khuri-Yakub, "The microfabrication of capacitive ultrasonic transducers," J. Microelectromech. Syst., vol. 7, no.3, pp 295~302, Sept. 1998.

[14] X. C. Jin, I. Ladahaum, F. L.Degertekin, S. Calmes and B. T. Khuri-Yakub, "Fabrication and characterization of surface micromachined capacitive ultrasonic immersion transducers," IEEE/ASME J. Microelectromech. Syst., vol.8, pp. 100-114, Mar. 1999.

[15] B. T. Khuri-Yakub, C. -H Cheng, F. L. Degertekin., S. Ergun, S. Hansen, X. C. Jin, and O. Oralkan "Silicon micromachined ultrasonic Transducers, "Jpn. J.Appl. Phys., vol. 39, pp 2883~2887, May 2000.

[16] Omer Oralkan, A.Sanli Ergun, etc., "Capacitive Micromachined Ultrasonic Transducers: Next Generation Arrays for Acoustic Imaging?", IEEE. Trans. Ultrason, Ferroelect., Freq. Contr. Vol. 49, No.11, Nov. 2002.

[17] Keith Daniel, "Focusing Piezoelectric Ultrasonic Medical Diagnostic System", Oct.2.1979, US Patent 4,276,491.

[18] Yoichi Haga, Masayoshi Esashi, "Biomedical Microsystems for minimally invasive diagnosis and treatment", Proceedings of the IEEE, Vol. 92, No.1 Jan 2004.

[19] Douglas M. Cavaye, Rodney A. White. Intravascular Ultrasound Imaging, Raven Press.1993.

[20]Omer Oralkan, Sean T. Hansen, Baris Bayram, Goksen G Yarahoglu, A. Sanli Ergun, and Butrus T. Khuri-Yakub, "CMUT Ring Arrays for Forwad-Looking Intravascular Imaging," Proceedings of the 2004 IEEE Ultrasonics Symposium, pp.403-406.

[21] Joshua G. Knight and F. Levent Degertekin, "Capacitive Micromachined Ultrasonic Transducers for Forward Looking Intravascular Imaging Arrays," Proceedings of the 2002 IEEE Ultrasonics Symposium, pp. 1079-1082.

[22] Y. Wang, D. N. Stephens, and M. O'Donnell, "A Forward-Viewing Ring-Annular Array for Intravascular Imaging," Proceedings of the 2001 IEEE Ultrasonics Symposium, pp. 1573-1576.

[23] Y. Wang, D. N. Stephens, and M. O'Donnell, "Initial Results from a Forward-Viewing Ring-Annular Ultrasound Array for Intravascular Imaging," Proceedings of the 2003 IEEE Ultrasonics Symposium, pp. 212-215.

[24] J. A. Shercliff, "The Theory of Electromagnetic Flow Measurement," Cambridge: University Press, 1962.

[25] M. D. Stern, "In vivo evaluation of microcirculation by coherent light scattering," Nature, vol.254, London 1975, pp 56-58.

[26] A. Sacks, G. Ksander, etc. "Difficulties in laser Doppler measurement of skin blood flow under applied external pressure". Journal of Rehabilitation Research and Development vol.25 No.3 pp. 19-24.

[27] Jonathan P. Majo. "A study of Blood-flow measurement by Doppler Effect utilizing a non-stationary signal processing technique" Masters dissertation, Clarkson University, 2005.

[28] Charles W.Francis, "Ultrasound-Enhanced Thrombolysis" Echocardiology, Volume 18.3,April 2001.

[29] K. Y. Saleh, N. B. Smith, "Two-dimensional ultrasound phased array design for tissue ablation for treatment of benign prostatic hyperplasia" Int. J. Hyperthermia, vol 20, No.1 Feb 2004 PP 7-31.

[30] Mark E.Schafer, Jame Gessert , Wayne Moore, "Development of a High Intensity Focused Ultrasound (HIFU) Hydrophone System" 2005 IEEE Ultrasonic Symposium.

[31] Ethan J. Halpern, "High-Intensity Focused Ultrasound Ablation: Will Image-guided Therapy Replace Conventional Surgery" Radiology *2005;235:345-346*

[32] J. E. Schneider, S. D. Bamforth, S. M. Grieve, K. Clarke, S. Bhatacharya, and S. Neubauer, "High resolution, high-throughput magnetic paragraph sign resonance imaging of mouse embryonic paragraph sign anatomy using a fast gradient-echo sequence." Magma 16, 443-51 (2003).

[33] P. Mansfield, and P. G. Morris, NMR Imaging in Biomedicine, New York: Academic Press (1982).

[34] X. Wang, Y. Pang, G. Ku, X. Xie, G. Stoica, and L.-H. Wang, "Non-invasive laser-induced photoacoustic tomography for structural and functional imaging of the brain in vivo," *Nature Biotechnology* 21 (7), 803-806 (2003).

[35] M. Xu and L. V. Wang, "Photoacoustic imaging in biomedicine," Review of Scientific Instruments 77, 041101, pp. 1–22, 2006.

[36] Igal Ladabaum, Xuecheng Jin etc., "Surface Micromachined Capacitive Ultrasonic Transducers", IEEE.Trans. Ultraon, Ferroelect., Freq. Contr. vol. 45, No.3, May 1998

[37] O.Ahrens, A.Buhrdorf, D.Hohlfeld, L.Tebje, and J.Binder, "Fabrication of gap-optimized CMUT," IEEE Trans. Ultrason., Ferroelect. Freq. Contr., vol. 49, no.9, pp 1321-1329, 2002

[38] Annette Lohfink, Peter-christian Eccardt, "Linear and nonlinear equivalent Circuit modeling of CMUT" IEEE Trans. Ultrason, Ferroelect. Freq. Contr., vol. 52, No.12, pp 2163~2172, Dec 2005

[39] W J Wang, R M Lin, Q B Zou and X X Li, "Modeling and characterization of a silicon condenser microphone", J. Micromech. Microeng. 14 (2004) 403-409.

[40] A. Bozkurt, I. Ladabaum, A. Atalar, and B. T. Khuri-Yakub, "Theory and analysis of electrode size optimization for capacitive microfabricated ultrasonic transducers," IEEE trans. Ultrason., Ferroelect., Freq. Contr., vol. 46, pp 1364-1374, 1999

[41] J. Cheng, J. Zhe, X. Wu, K. R. Farmer, V. Modi, and L. Frechette, "Analytical and FEM Simulation Pull-in Study on Deformable Electrostatic Micro Actuators," in International Conference on Modeling and Simulation of Microsystems, Puerto Rico, USA, 2002, p. 4.

[42] I. Dufour and E. Sarraute, "Analytical Modeling of Beam Behavior Under different Actuations: Profile and Stress Expressions," Journal of Modeling and Simulation of Microsystems, vol. 1, no. 1, pp. 57–64, 1999.

[43] A. S. Ergun, G. G. Yaralioglu, B. T. Khuri-Yakub "Capacitive Micromachined Ultrasonic Transducers: Theory and Technology. Journal of Aerospace Engineering, ASCE, Apr 2004 pp76~84.

[44] Ark-Chew Wong, "VHF Microelectromechanical Mixer-Filters" PhD dissertation, University of Michigan, 2001.

[45] G. G. Yaralioglu, A. S. Ergun, B.Bayram, E. Hæggstrom, and B. T. Khuri-Yakub, "Calculation and measurement of electromechanical coupling coefficient of capacitive micromachined ultrasonic transducers," IEEE Trans. Ultrason., Ferroelect., Freq. Contr., vol 50, pp 449-456, 2003.

[46] Muhammed N. Senlik, Selim Olcum, Abdullah Atalar, "Improved performance of CMUT with nonuniform membranes." IEEE ultrasonics symposium., 2005, pp597~600.

[47] T. B. Avallone III and E. A. Avallone, "Mark's Standard Handbook for Mechanical Engineers," Tenth Edition, McGraw-Hill, New York, NY 1996.

[48] L.Kinsler, A.Frey, A.Coppens, J.Sanders. "Fundamental of Acoustics" Fourth Edition, John Wiley & Sons, 2000

[49] Yuan Xie , "Micromechanical Extensional Wine-Glass Mode Ring Resonators For Wireless Communications", Ph.D dissertation, 2006, University of Michigan.

[50] Alessandro Caronti, Riccardo Carotenuto, and Massimo Pappalardo, "Electromechanical coupling factor of capacitive micromachined ultrasonic transducers". J. Acoust. Soc. Am. 113(1) Jan 2003 pp 279~288.

[51] F. V. Hunt, Electroacoustics; The Analysis of Transduction, and its historical background, Cambridge, MA: Harvard University, 1954.

[52] Y. Zhang, K. D. Wise,; An ultra-sensitive capacitive pressure sensor with a bossed dielectric diaphragm: Technical Digest, Solid-State Sensor and Actuator Workshop; 1994.

[53] T. Umeda, Y.Mochizuki, etc "Charge-trapping defects in Cat-CVD silicon nitride films", Thin Solid films 395 (2001) 266-269.

[54] L. Do Thanh and Balk " Properties of Thin Oxide-Nitride-Oxide Stacked Films" Journal of Electronic Materials, Vol.17, No.2 1988.

[55] William G. Meyer, Richard B. Fair "Dynamic Behavior of the Buildup of Fixed Charge and Interface States During Hot-Carrier Injection in Encapsulated MOSFET's" IEEE Transactions on Electron Devices Vol. ED-30, No.2 February 1983.

[56] S. M. Sze, *Physics of Semiconductor Devices*, 2nd ed. New York: JohnWiley and Sons, 1981.

[57] W. Olthuis and P. Bergveld, "On the Charge Storage and Decay Mechanism in Silicon Dioxide Electrets," *IEEE Transactions on Electrical Insulation*, vol. 27, no. 4, pp. 691– 697, 1992.

[58] L. Huamao, X. Zhongfu, and S. Shaoqun, "The Study of the Intrinsic Charges in SiO2 Electrets," in *Proc. Intern. Symp. on Electrets of ISE8*, Paris, 1994, pp. 107–112.

[59] Mario Kupnik, "Ultrasonic Transit-Time Gas Flowmeter For Automotive Applications", Ph.D dissertation, 2004, University of Leoben.

[60] Shea, H. R.; Gasparyan, A.; Chan, H. B.; Arney, S.; Frahm, R.E.; Lopez, D.; Jin, S.; McConnel, R.P. "Effects of electrical leakage currents on MEMS reliability and Performance". IEEE Trans on Device and Materials Reliability 2004, 4(2)198-207.

[61] Goksen G. Yaralioglu, Mohammaed H. Badi, A. Sanli Ergun, and B. T. Khuri-Yakub, "Improved Equivalent Circuit and Finite Element Method Modeling of Capacitive Micromachined Ultrasonic Transducers". IEEE Ultrasonic Symposium, 2003 pp 469~472.

[62] Shiwei Zhou, Paul Reynolds, John A Hossack, "Improving the Performance of Capacitive Micromachined Ultrasound Transducers using Modified Membrane and Support Structures." IEEE Ultrasonic Symposium,2005.

[63] Yongli Huang, A. Sanli Ergun, Edward Haggstrom, Mohammed H. Badi, and B. T. Khuri-Yakub, "Fabricating Capacitive Micromachined Ultrasonic Transducers with Wafer Bonding Technology". Journal of Microelectromechanical Systems, Vol.12, No.2, April 2003

[64] http://www.mbadi.com/mbadi_papers/waferbond.pdf

[65] K. Kirk Shung, Michael B. Smith, Benjamin Tsui, "Principles of medical imaging", Copyright 1992 by Academic press, Inc.

[66] Jan Ove Erstad "Design of sparse and non-equally spaced arrays for medical ultrasound" University of Oslo Department of informatics, November 14th 1994.

[67] Jian-Yu Lu, "A study of two-dimensional array transducer for limited diffraction beams" IEEE Transaction on ultrasonic, Ferroelectric, and Frequency control, vol. 41, no. 5, September 1994.

[68] M. Moshfeghi, "Sidelobe suppression in annular array and axicon imaging systems". J. Acoust. Soc. Am. 83:2202-2209; 1988.

[69] Sverre Holm, "Medical Ultrasound Transducers and Beamforming" Proc. 15th Int. Congress on Acoustics, Trondheim, Norway, 26-30 June 1995.

[70] Bjørn A.J. Angelsen, Hans Torp, Sverre Holm, Kjell Kristofersen, T.A. Whittingham. "Which transducer array is best?". European Journal of Ultrasound 2 (1995) 151-164.

[71] Durnin, J,; Miceli, J. J., Jr.; Eberly, J. H. Diffraction-free beams. Phys. Rev. Lett. 58:1499-1501; 1987.

[72] Fatemi, M.; Arad, M. A. Ultrasonic nondiffracting beam image formation and restoration. IEEE 1991 Ultrason. Symp. Proc. 91CH3079-1. 2:1305-1308;1991.

[73] Kino, G. S. Acoustic waves: Devices, imaging, and analog signal processing. Englewood Cliffs, NJ: Prentice-Hall, Inc.; 1987.

[74] Jian-Yu Lu, Hehong Zou and James F. Greenleaf, Biomedical Ultrasound Beam Forming, Ultrasound in Med. & Biol., Vol. 20 No.5 pp. 403-428, 1994.

[75]http://www.stanford.edu/class/me342/Projects/2005/ME342%20Mouse%20Abstract%208_10_05.pdf

[76] Yongrae Roh, and Butrus T.Khuri-Yakub, "Finite Element Analysis of Underwater Capacitor Micromachined Ultrasonic Transducers," IEEE Trans. Ultrason, Ferroelect., Freq.Contr., Vol. 49, No.3, March 2002.

[77] B. Bayram, O. Oralkan, A. S. Ergun, E. Ha□ggstrom, G. G. Yaralioglu, and B. T.Khuri-Yakub, "Capacitive Micromachined Ultrasonic Transducer Design for High Power Transmission," Ultrasonics, Ferroelectrics and Frequency Control, IEEE Transactions on, vol.52, no.2, pp. 326~339, Feb. 2005.

[78] Yongrae Roh, and Butrus T. Khuri-Yakub, "Finite Element Analysis of Underwater Capacitor Micromachined Ultrasonic Transducers," IEEE Trans. Ultrason, Ferroelect., Freq. Contr., Vol. 49, No.3, March 2002.

[79] Alessandro Caronti, Riccardo Carotenuto, "A finite Element Study of Cross Coupling in 1-D Capacitive Micromachined Ultrasonic Transducer Array," Ultrasonic Symposium, 2002, Proceedings. Vol. 2, 8-11 Oct 2002, pp 1059~1062.

[80] http://www.acoustics.co.uk/products/hp1

[81] L A Rocha1, E Cretu2 and R Fwolffenbuttel, "Measuring and interpreting the mechanical–thermal noise spectrum in a MEMS." J. Micromech. Microeng. 15 (2005) S30–S38.

[82] Russell S. Wittea*, S. Huanga, S. Ashkenazia, K. Kima and M. O'Donnell, "Contrast-enhanced photoacoustic imaging of live lobster nerve cord." Proc. of SPIE Vol. 6437, 64370J, (2007)

[83]. B. T. Cox, S. R. Arridge, K. P. Kostli and P. C. Beard, "Two-dimensional quantitative photoacoustic image reconstruction of absorption distributions in scattering media by use of a simple iterative method," Appl Opt 45(8), 1866-1875 (2006).

[84]. G. Paltauf and P. E. Dyer, "Photomechanical processes and effects in ablation," *Chem Rev* 103(2), 487-518 (2003).

[85]. A. N. S. Institute, *American National Standard for the Safe Use of Lasers*, American National Standards Institute, New York (2000).

[86] http://www.ondacorp.com/index1.html

[87] M. Wang, J. Chen, X. Cheng, "The Initial Doppler Flow Measurement Using an Implantable CMUT Array" IEEE Ultrasonic Symposium, 2007, New York

[88] M.Karaman and B. T. Khuri-Yakub, "Low-cost front-end processing for large array systems," in Proc. 17th Int. Congr. Acoust. (ICA'01), 2001

[89] Joshua Knight, Jeff Mclean, and F.Levent Degertekin. "Low Temperature Fabrication of Immersion Capacitive Micromachined Ultrasonic Transducers on Silicon and Dielectric Substrates". IEEE Transactions on Ultrasonics, Ferroelectrics, and Frequencies Control. Vol 51, No.10, Oct. 2004.

[90] M.Chen, and M.Lu, "Design and characterization of an air-coupled capacitive ultrasonic sensor fabricated in a CMOS process", J.Micromec, Microeng, 18 2008.

[91] B.P.Gogoi, S.Jo, R.August, A.McNeil, M.Fuhrmann, J.Torres, T.F.Miller, A.Reodique, M.Shaw, etc "A 0.8um CMOS Integrated Surface Micromachined Capacitance Pressure Sensor With EEPROM Trimming and digital output for a tire pressure monitoring system.

[92] S. Linder, H. Baltes, F. Gnaedinger, and E. Doering, "Fabrication technology for wafer through-hole interconnections and three-dimensional stacks of chips and wafers," in Proc. MEMS, 1994, pp.349~354

[93] C. Cheng, E. Chow, X. Jin, S. Ergun, B. T. Khuri-Yakub, "An Efficient Electrical Addressing Method Using Through-wafer Vias For two-dimensional Ultrasonic Arrays"., IEEE Ultrasonic Symposium, 2000, pp.1179~1182

[94] S.Choa, "Experimental Studies of Through-wafer Copper interconnect in wafer Level MEMS Packaging", Key Engineering Materials Vols. 324~325 (2006) pp. 231-234

[95] D. Lemmerhirt, K. D. Wise, "Air-isolated through-wafer interconnects for microsystem applications", Transducers, Solid-state Sensors, Actuators and Microsystems, 12th International Conference on, Volume 2, Issue, 8-12 June 2003 pp. 1067~1070 vol.2.

[96] H. T. Soh, C. P. Yue, A. McCarthy, et al., "Ultralow resistance, through-wafer via (TWV) technology and its application in three dimensional structures on silicon", Japanese Journal of Applied Physics, Part I 38(4B) 2393-6 (1999)

[97] T. R. Anthony, "Forming electrical interconnections through semiconductor wafers", Journal of Applied Physics, 52(8) 5340-9 (1981).

[98] E. M. Chow, **A.** Partridge, C. F. Quate, T. W. Kenny, "Through-Wafer Electrical Interconnects Compatible with Stanford Semiconductor Processing", Solid-state Sensor and Actuator Workshop, Hilton Head Island, South Carolina, June 4-8, 2000, pp. 343-6 (2000)

[99] R.Vetter, J.Williams, J.Hetke, E. A. Nunamaker, D.Kipke, " Chronic Neural Recording Using Silicon-Substrate Microelectrode Arrays Implanted in Cerebral Cortex", IEEE Transactions on Biomedical Engineering, Vol. 51, No.6, June 2004.

[100] M.Senlik, A.Atalar, H.Koymen,etc "Radiation impedance and equivalent circuit for immersed CMUT Array Element", IEEE Ultrasonic Symposium, 2006

[101] Arif Sanli Ergun, Yongli Huang, Xuefeng Zhuang, Omer Oralkan, Gokesen G.Yaralioglu, B.T.Khuri-Yakub, "Capacitive Micromachined Ultrasonic Transducers: Fabrication Technology" IEEE Trans. Ultrason. Ferroelect, Freq. Cont. vol 52, No.12 Dec 2005.

[102] O. Oralkan, S. Hansen, B. Bayram, etc, "High-Frequency CMUT Arrays for High-Resolution Medical Imaging", IEEE Ultrasonic Symposium 2004.

[103] Sean T. Hansen*, A. Sanlı Ergun, and Butrus T. Khuri-Yakub. "Wideband micromachined acoustic sensors with radio frequency detection" Proceedings of SPIE Vol. 5090 (2003)

[104] Sean T. Hansen,a) A. Sanli Ergun, William Liou, Bertram A. Auld, and Butrus T. Khuri-Yakub, "Wideband micromachined capacitive microphones with radio frequency detection". J. Acoust. Soc. Am. 116 (2), August 2004.

[105] R. Held, V. Zderic, T. Nguyen, etc " Annular Phased-Array High-Intensity Focused Ultrasound Device for Image-Guided Therapy of Utenrine Firoids" IEEE Transactions on Ultrasonics, Ferroelectrics, and Frequency control, Vol.53, No.2 Feb 2006.

[106] Clark Nguyen, "Micromechanical Signal Processors" PhD dissertation, University of California, Berkeley, 1994

[107] O.Oralkan, S. Hansen, B.Bayram, G.G.Yarahoglu, A.Ergun, B.T.Khuri-Yakub, "High-frequency CMUT arrays for High-resolution Medical Imaging" 2004 IEEE Ultrasonic Symposium.